E.O. Paton Electric Welding Institute of the National Academy of Sciences of Ukraine

International Scientific-Technical and Production Journal

The Paton WELDING JOURNAL

August **2017**
No. 8

Published since 2000

English translation of the monthly «Avtomaticheskaya Svarka» (Automatic Welding) journal published in Russian since 1948

Founders
E.O. Paton Electric Welding Institute, NASU
International Association «Welding»

Publisher
International Association «Welding»

Translators
A.A. Fomin, O.S. Kurochko, I.N. Kutianova
Editor
N.G. Khomenko
Electron galley
D.I. Sereda, T.Yu. Snegiryova

Address
E.O. Paton Electric Welding Institute,
International Association «Welding»
11 Kazimir Malevich Str. (former Bozhenko Str.),
03680, Kiev, Ukraine
Tel.: (38044) 200 60 16, 200 82 77
Fax: (38044) 200 82 77, 200 81 45
E-mail: journal@paton.kiev.ua
www.patonpublishinghouse.com

State Registration Certificate
KV 4790 of 09.01.2001
ISSN 0957-798X
doi.org/10.15407/tpwj2017.08.01

Subscriptions
$348, 12 issues per year,
air postage and packaging included.
Back issues available.

CONTENTS

SCIENTIFIC AND TECHNICAL

INDUSTRIAL

NEWS

INFORMATION

doi.org/10.15407/tpwj2017.08.01

EFFECTIVE VALUES OF ELECTRODYNAMIC CHARACTERISTICS OF THE PROCESS OF NONCONSUMABLE ELECTRODE WELDING WITH PULSE MODULATION OF ARC CURRENT

V.F. DEMCHENKO, U. BOI, I.V. KRIVTSUN and **I.V. SHUBA**
E.O. Paton Electric Welding Institute, NASU
11 Kazimir Malevich Str., 03680, Kiev, Ukraine. E-mail: office@paton.kiev.ua

The paper is devoted to analysis of the influence of pulse modulation of welding current on effective values of electrodynamic characteristics of the process of nonconsumable electrode welding. The first part of the paper provides analysis of the possibilities for increasing the effective value of arc current through selection of optimum time and current parameters of pulse modulation. A quite general case of current modulation by pulses of trapezoidal shape is considered (rectangular and triangular pulses are treated as particular cases). In the second part distribution of effective values of electromagnetic and dynamic characteristics of modulated current in the weld pool is studied, proceeding from a nonstationary model of arc discharge and model of electromagnetic processes in the metal being welded. Force impact of modulated current on weld pool metal at current modulation by triangular pulses with pauses at 10 kHz frequency is considered as a characteristic example. Influence of dynamic effects in the pulsed arc on distribution of effective values of electromagnetic characteristics, namely centripetal component of Lorenz force and magnetic pressure, is analyzed. A conclusion is made that with optimum shape of current pulses dynamic effects arising in nonstationary arc are capable of essentially enhancing its force impact on weld pool metal in nonconsumable electrode welding with high-frequency current modulation, compared to welding by constant current coinciding in magnitude with effective value of modulated current. 19 Ref., 13 Figures.

Keywords: *nonconsumable electrode welding, pulse current modulation, electrodynamic characteristics, effective value, weld pool metal, mathematical models*

Pulse modulation of arc current in nonconsumable electrode (TIG) welding is one of the effective methods to control the characteristics of thermal and dynamic impact of the arc on the metal being welded. Variation of the parameters of welding current modulation, such as frequency, relative pulse duration, pulse amplitude and shape, allows changing the depth and shape of metal penetration, and thermal cycle of welding in a broad range, and, therefore, influencing the structure and properties of weld metal and near-weld zone, lowering residual stresses and deformations of welded item. Determination of optimum values of parameters of welding current pulse modulation requires having valid data on relative influence of each of them on the nature of running of thermal, electromagnetic, gas- and hydrodynamic processes in arc plasma and metal being welded.

A large number of works are devoted to experimental study and mathematical simulation of processes running in arc plasma, on the surface and in the volume of metal being welded in TIG welding with pulse modulation of arc current [1–12]. Modes with low-frequency (modulation frequency $F < 10$ Hz) [1, 2, 6, 7, 9, 10], medium frequency ($F \leq 5$ kHz) [2, 4, 5] and high-frequency ($F > 10$ kHz) [2, 3, 8, 11, 12] modulation of welding current, are considered. In the majority of the above-listed publications, however, (except for works [2, 4]) practically no attention is given to studying the influence of current pulse shape on the nature of running of nonstationary processes of heat-, mass- and charge transfer in the considered system, as well as on the effective values of the above process characteristics. Moreover, only low-frequency modulation of arc current is considered in publications devoted to detailed numerical modeling of the process of TIG welding by modulated current [6, 7, 9, 10]. Therefore, the objective of this work is theoretical study and numerical analysis of the influence of the shape of welding current pulses in a broad range of modulation frequencies on effective values of electromagnetic characteristics, determining the thermal, and, particularly, dynamic (force) impact of the arc with refractory cathode on the metal being welded.

Basic postulates. Let $I(t)$ be the periodically changing in time t arc current, assumed to be unidirectional; $\tau = 1/F$ is the current modulation period; $I_A = \langle I \rangle$, $I_E = \sqrt{\langle I^2 \rangle}$ is its average and effective values, respectively. Here and furtheron $\langle \phi \rangle$ means integral mean value of function $\phi(t)$ in the range of $[0, \tau]$:

$$\langle \phi \rangle = \frac{1}{\tau} \int_0^{\phi} \phi(t)\,dt.$$

Effective value of alternating current is usually understood to be such a value of constant current, which creates a thermal effect, coinciding with thermal effect of alternating current. At constant ohmic resistance R of the conducting medium thermal power W, generated by constant current I, is expressed in terms of the square of current, according to Joule–Lenz law: $W = I^2R$. Then, in keeping with the above interpretation of effective value of alternating current, the following equality holds: $W = W_E$, where $W_E = I_E^2 R$ is the effective thermal power of alternating current.

In the case of nonconsumable electrode welding with pulse current modulation, this interpretation of the effective value of current is valid only at consideration of the processes of current transfer and heat input in the metal being welded, specific electric resistance of which is weakly dependent on the value of flowing current. At the same time, because of the high electric conductivity of metals, thermal effect of current flowing in the metal being welded, turns out to be insignificant. Therefore, effective value of current as the determining characteristic of thermal processes in the item being welded, is not significant. In contrast to that, Joule heating of arc plasma has a decisive influence on its thermal state. In keeping with volt-ampere characteristic of the arc, however, arc voltage U (arc gap resistance R) essentially depends on flowing current [3, 13]. Therefore, thermal power W_E of the arc at pulse modulation of current should be determined by averaging the product of arc current and voltage

$$W_E = \langle IU \rangle = \frac{1}{\tau} \int_0^{\tau} I(t)U(t)\,dt$$

[3], i.e. in the form, which is not expressed directly through the square of effective current value.

Welding current impact on arc plasma and metal being welded is not exhausted by generation of thermal energy. Another important characteristic of such an impact is electromagnetic force, arising as a result of interaction of arc current with intrinsic magnetic field. The impact of this force is manifested in two ways. On the one hand, the resultant gas-dynamic head of arc plasma flow deforms the free surface of the weld pool, resulting in shifting of the heat source in-depth of the metal being welded, thus promoting increase of penetration depth. On the other hand, electromagnetic force, acting on molten metal in the weld pool, intensifies convective energy transfer from the most heated central part of pool surface to its bottom part that also promotes increase of penetration depth [14].

Let us now consider the thermal and dynamic impact of modulated current on the metal being welded. For this purpose, we will perform assessment of the time of relaxation of thermal and gas-dynamic states of the metal melt at its disturbance due to external impact, which we will associate with pulsed change of welding current in the context of the discussed problem. Let $\mathrm{Fo}^{(T)} = a\bar{t} / \bar{l}^2$ and $\mathrm{Fo}^{(V)} = \nu\bar{t} / \bar{l}^2$ be the thermal and hydrodynamic Fourier criteria. Here: a is the thermal diffusivity of the metal being welded; ν is the coefficient of kinematic viscosity of the melt; $\bar{l}$ is the characteristic geometrical size of the weld pool, $\bar{t}$ is the characteristic time. As is customary, we will assume that during times $\bar{t}^{(T)}$, $\bar{t}^{(V)}$, as which values of criteria $\mathrm{Fo}^{(T)}$ and $\mathrm{Fo}^{(V)}$ reach a unity, relaxation of disturbance of thermal and hydrodynamic state of the metal due to the impact of disturbing external factor, takes place. Selecting the characteristic size of the weld pool $\bar{l}$ = 0.5 cm and assuming that for stainless steel, for instance, $a = 0.07$ cm^2/s, $\nu = 0.07$ cm^2/s [6], we obtain: $\bar{t}^{(T)}, \bar{t}^{(V)} \approx 3.6$ s. These, very approximate calculations, allow assessing the duration of transient processes of heat- and mass-transfer in the weld pool as a value of the order of several seconds. We can confidently say that at modulation frequencies $F \geq 100$ Hz (modulation period $\tau < 10^{-2}$ s) thermal and hydrodynamic processes in the weld pool are sensitive not to current, time-varying characteristics of electromagnetic field, but to their values, averaged over the period of current modulation.

Work [14] also shows that at spot DC TIG welding, volume density of electromagnetic force in the weld pool, excited by electric current flowing through it, is proportional to $I^2(r, z)$, where $\{r, z\}$ is the cylindrical system of coordinates, axis OZ of which is directed normal to the surface of metal being welded; $I(r,z) = 2\pi \int_0^r j_z(r',z) r'\,dr'$ is the current, flowing within a circle of radius r, selected in an arbitrary axial section z of the pool; $j_z(r, z)$ is the axial component of current density. According to the above-performed evaluation of characteristic times $\bar{t}^{(T)}, \bar{t}^{(V)}$, in welding with modulated current of frequency $F > 100$ Hz, force impact of arc current on weld pool metal is expressed through value $\langle I^2(r, z) \rangle$, i.e. it depends on effective value of the square of current, flowing through a circle of the selected radius. Note that unlike determination of effective current value by its thermal effect, this characteristic is in no way connected with ohmic resistance of the metal. Therefore, the notion of effective value of current in TIG welding by modulated current can be given another, more general meaning, based not on thermal but on force impact of current on the metal being welded.

It is obvious that the greater the square of effective value of welding current I_E^2, the larger its distributed characteristic $\langle I^2(r, z)\rangle$, and the greater the effective force impact of arc current on the metal being welded, respectively. At assigned average value of modulated current I_A its maximum effective value I_E can be achieved by properly selecting the shape and time parameters of the pulses. This problem is considered in the first section of this paper for the general case of welding current modulation by pulses of a trapezoidal shape, particular cases of which are triangular and rectangular pulses. The second section presents the results of numerical analysis of effective (averaged by modulation period) electrodynamic characteristics distributed in the volume of the metal being welded, in TIG welding with pulse modulation of current. At analysis of these results, attention is focused on force impact of arc current on weld pool metal, as well as its influence on the intensity of hydrodynamic flows, excited in it.

1. Effective value of modulated current. Let us consider modulated current $I(t)$ in the form of unidirectional pulses of trapezoidal shape with pauses between them (Figure 1, *a*). Average value of such current can be presented in the form of $I_A = (1 - \alpha)I_1 + \alpha I_2$, where $\alpha = \frac{\tau_3 + \tau_2 - \tau_1}{2\tau}$ $(0 \le \alpha \le 1)$; τ_1, $\tau_3 - \tau_2$ are the durations of leading and trailing fronts; $\tau_2 - \tau_1$ is the duration of pulse «plateau», where current is kept constant, equal to I_2; $\tau - \tau_3$ is the duration of the pause (see Figure 1, *a*). Thus, average value of modulated current is expressed in terms of values of current in the pause I_1 and maximum current in the pulse I_2, as well as through dimensionless time parameter α. Let us introduce two more dimensionless parameters: $\xi = \tau_3 / 2\tau$ $(0 < \xi \le \frac{1}{2})$ and $\gamma = (\tau_2 - \tau_1)/\tau_3$ $(0 \le \gamma \le 1)$. The first of them characterizes relative pulse duration (mode stiffness) and is connected with relative pulse duration $s = \tau/\tau_3$ by ratio $\xi = 1/2s$, and the second is the relative duration of pulse «plateau» and characterizes its shape (at $\gamma = 0$ trapezoidal pulse becomes a triangular one, and at $\gamma = 1$ it becomes rectangular). As a result, dimensionless parameter α can be expressed through ξ and γ as follows: $\alpha = \xi(1 + \gamma)$.

For any periodically changing current $I(t)$ the following representation holds:

$$I(t) = I_A = A\eta(t) \tag{1}$$

where $A = I_2 - I_1$ is the amplitude of current variation; $\eta(t)$ is a certain normed function, containing information about the shape and time characteristics of current pulses. According to the definition of average current, function $\eta(t)$ should meet the following condition

$$\int_0^\tau \eta(t)dt = 0. \tag{2}$$

In particular, for a trapezoidal pulse, given in Figure 1, *a*, function $\eta(t)$ has the following form (see Figure 1, *b*):

$$\eta(t) = \begin{cases} \frac{t}{\tau_1} - \alpha, \ 0 < t < \tau_1; \\ 1 - \alpha, \ \tau_1 < t < \tau_2; \\ -\frac{t - \tau_2}{\tau_3 - \tau_2} + 1 - \alpha, \ \tau_2 < \tau < \tau_3; \\ -\alpha, \ \tau_3 < t < \tau. \end{cases} \tag{3}$$

Using representation (1) and condition (2), the following expression for the square of effective current value can be derived:

$$I_E^2 = I_A^2 + A^2 f(\xi, \gamma), \tag{4}$$

where $f(\xi, \gamma) = \langle\eta^2\rangle$.

Omitting cumbersome calculations, we will give the final expression for function $f(\xi, \gamma)$:

$$f(\xi, \gamma) = \xi\left[\frac{2}{3}(1 + 2\gamma) - \xi(1 + \gamma)^2\right],$$

behaviour of which is shown in Figure 2. From the explicit form of this function it follows that effective value of pulsed current depends on relative duration and shape of pulses and does not depend on their repetition rate. We will also note that $f(\xi, \gamma) \ge 0$, i.e. square of effective value of current is higher than average current square.

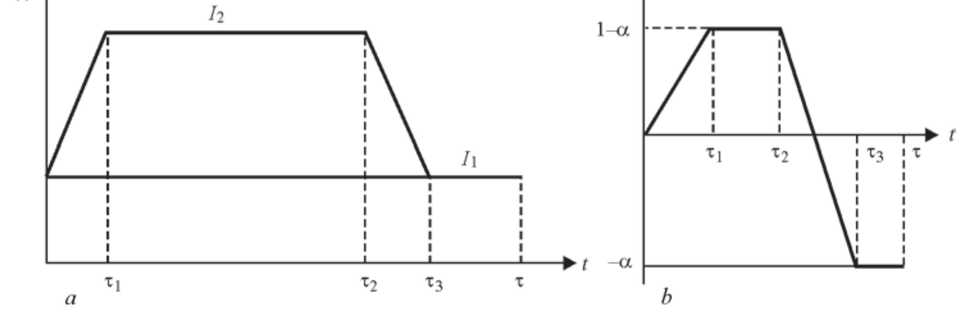

Figure 1. Schematic representation of arc current pulse: *a* — trapezoidal pulse with a pause; *b* — respective normed pulse (function $\eta(t)$)

As follows from expression (4), at specified value of I_A there are two possibilities to increase the effective value of modulated current: the first is through increasing amplitude A; the second — by selection of such values of time parameters of the pulse, at which function $f(\xi, \gamma)$ has the highest value. In the first case, increasing the magnitude of current I_2, in principle, allows reaching as high a value of current I_E as is desired, by reducing pulse duration appropriately, so as to ensure satisfying condition I_A = const. Considering the quadratic dependence of I_E^2 on current amplitude, this method is highly effective. Its application, however, is limited by the capabilities of arc power source (in equipment models known to the authors $I_2 \leq 500$ A [8]). Therefore, it is of interest to consider the second method of increasing I_E.

Furtheron we will assume that values I_1, I_2 (or A), as well as average current value I_A are given and will select parameters ξ, γ so that function $f(\xi, \gamma)$ included into expression (4), had the highest values. Note that at given values I_1, A, I_A, parameter $\alpha = \xi(1+ \gamma)$ is uniquely determined: $\alpha = (I_A - I_1)/A$. Therefore, at analysis of numerical values of function $f(\xi, \gamma)$ not the entire range of ξ, γ variation should be considered, but just those of their values, which satisfy equation $\xi(1 + \gamma) = \alpha$. Expressing γ from this equation through ξ, α, and substituting it into the expression for $f(\xi, \gamma)$, we obtain $f(\xi, \alpha) = \frac{4}{3}\alpha - \alpha^2 - \frac{2}{3}\xi$. This function decreases monotonically with ξ increase and has the largest value at minimum value $\xi_{\min}$. In case of triangular pulses ($\gamma = 0$) we find $\xi = \alpha$ from expression $\xi = \alpha/(1 + \gamma)$, and in the case of rectangular pulses ($\gamma = 1$) we have $\xi = \alpha/2$. Thus, minimum value $\xi_{\min} = \alpha/2$, providing at given α the largest value of function $f(\xi_{\min}, \alpha) = \alpha - \alpha^2$, is reached in the case $\gamma = 1$. Function $\alpha - \alpha^2$ has a maximum at $\alpha = 0.5$, that yields $\xi = 0.25$, i.e. this set of dimensionless parameters corresponds to rectangular pulses in the form of a meander.

Thus, at given I_1, A, I_A, of all the possible variations of the considered forms of the pulse, the largest effective value of current $I_E = \sqrt{I_1^2 + I_1 A + 0.5A^2}$ is reached at application of rectangular pulses in the form of a meander, average current value being $I_A = I_1 + 0.5A$.

As in practice it is impossible to reach an ideal rectangular shape of pulses, it is of interest to study behaviour of function $f(\xi, \gamma)$ for the general case of trapezoidal current pulse. Let us denote the total duration of the pulse leading and trailing fronts as $\tau_f = \tau_1 + \tau_3 - \tau_2$ (see Figure 1, *a*), determined by parameters of the power source and electric circuit, containing the welding arc. In the considered case minimum value of ξ is defined as follows: $\xi_{\min} = \alpha / (2 - \bar{\tau}_f)$, where $\bar{\tau}_f = \tau_f / \tau_3$, which yields

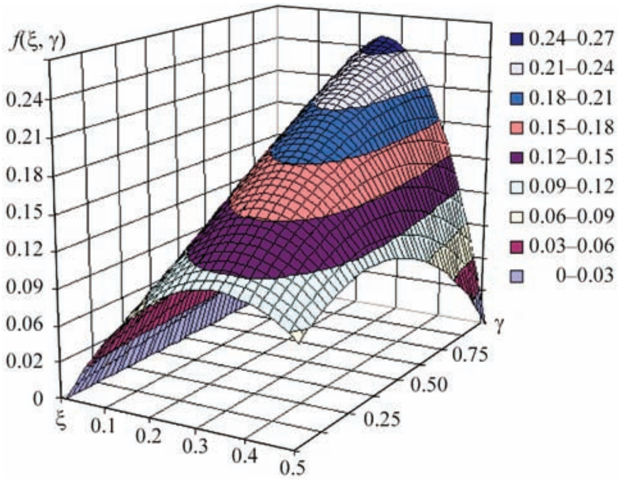

Figure 2. Appearance of function $f(\xi, \gamma)$

$$f(\xi_{\min}, \alpha) = \frac{2}{3}\left(2 - \frac{1}{2 - \bar{\tau}_f}\right)\alpha - \alpha^2.$$

This function has a maximum equal to

$$f(\bar{\tau}_f) = \frac{1}{9}\left(2 - \frac{1}{2 - \bar{\tau}_f}\right)^2,$$

at

$$\alpha = \frac{1}{3}\left(2 - \frac{1}{2 - \bar{\tau}_f}\right).$$

As follows from Figure 3, value of function $f(\bar{\tau}_f)$ is rather weakly dependent on total front duration. So, for instance, if τ_f is equal to 50 % of pulse duration, value $f(\bar{\tau}_f)$ decreases just by 20 %, compared to the best value achieved at current modulation by rectangular pulses in the form of a meander $(\bar{\ } \quad 0)$.

2. Distribution of effective values of characteristics of electromagnetic field of arc current in the metal being welded. As was noted above, in TIG welding with current modulation at more than 100 Hz frequency the impact of electromagnetic force on arc plasma and weld pool metal is determined not by current value of electromagnetic force, but by its value, averaged in time over the period of current modulation, i.e., effective value of the force. Expression for vor-

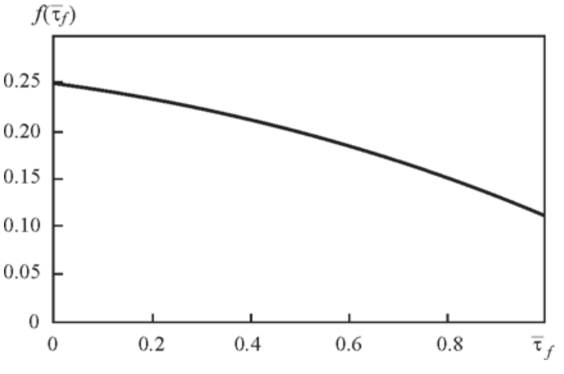

Figure 3. Influence of relative duration of pulse fronts on $f(\bar{\tau}_f)$

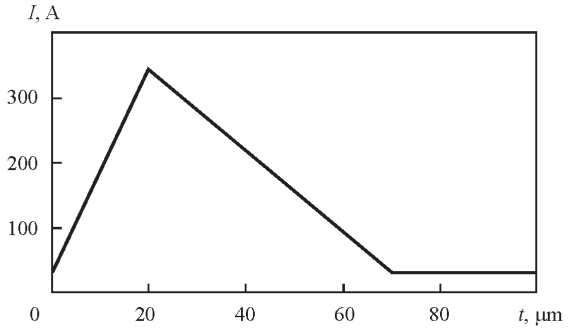

Figure 4. Triangular current pulse with pause

tex component of this force in the cylindrical system of coordinates is written in strict compliance with the one given in [14] for constant current arc with the only difference that $I^2(r, z)$ is replaced by $\langle I^2(r, z)\rangle$, namely

$$\vec{F}_{\text{rot}}(r,\ z) = -\mu_0\mu\frac{\langle I^2(r,z)\rangle}{4\pi^2 r^3}\vec{e}_r, \qquad (5)$$

here, μ is the metal permeability; μ_0 is the universal magnetic constant; $\vec{e}_r$ is the unit radius-vector.

Proceeding from magnetostatics equations [15], we can show that under the impact of force $\vec{F}_{\text{rot}}(r,\ z)$ a magnetic pressure field arises in the weld pool, average (over current modulation period) magnitude of which $\langle P_{\text{mag}}(r, z)\rangle$ is determined by the following formula

$$\langle P_{\text{mag}}(r,\ z)\rangle = \frac{\mu_0\mu}{4\pi^2}\int_r^\infty \left|\vec{F}_{\text{rot}}(r',\ z)\right| dr'. \qquad (6)$$

In the approximation of magnetostatics, radial component of magnetic pressure field $\langle P_{\text{mag}}(r,\ z)\rangle$ is balanced by force $\vec{F}_{rot}(r,\ z)$, and its axial component is balanced in the full system of equations of hydrodynamics by forces of nonmagnetic origin, primarily, those of inertia and viscosity [14].

We will use expressions (5), (6) for evaluation of effective values of electromagnetic force and magnetic pressure in the metal being welded in spot TIG welding by modulated current. Performance of detailed calculations requires information about the distribution of current characteristic $I(r, z, t)$ in the metal volume within one period of current modulation. Two mathematical models were developed for this purpose: first is model of the arc, burning in a nonstationary mode; second is the model of electromagnetic processes in the metal being welded in welding by modulated current. Axisymmetric (2D) model of constant current arc [16] was modified [17], allowing for nonstationary nature of thermal and gas-dynamic situation in arc plasma, which is due to a change of electric current in time (in keeping with the assigned shape of the pulse and frequency modulation). Such a model allows modeling the dynamics of burning of a nonstationary arc discharge and obtaining calculated data on time-varying distributed and integral characteristics of the arc column and anode region of the arc, including distribution of electric current density on the surface of metal being welded. Computer realization of the proposed model envisages feeding a packet of pulses in the quantity, sufficient for establishing arc plasma state, recurring from pulse to pulse.

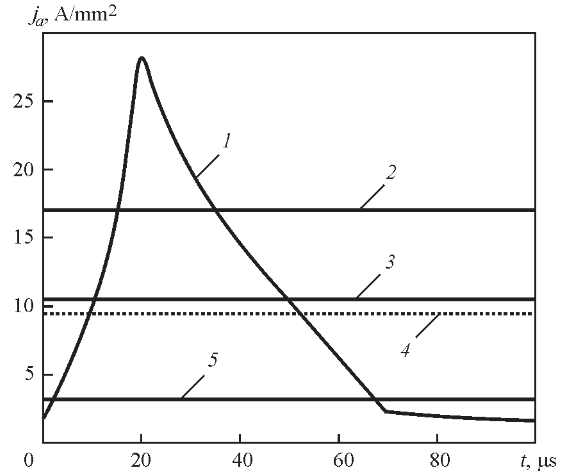

Figure 5. Change in time of axial current density in the arc anode binding region

During computational experiments, burning of argon arc 3 mm long with tungsten cathode was studied, anode was assumed to be non-evaporating, pulse current modulation was performed in the form of feeding triangular-shaped pulses with pauses between them (Figure 4) at the following values of current and time parameters of the pulse: I_1 = 30 A, I_2 = 345 A (A = 315 A); $\tau_1 = \tau_2$ = 20 μs, τ_3 = 70 μs, τ = 100 μs (ξ = 0.35; γ = 0), that corresponds to I_{A} = 140 A, $I_{\text{E}} \approx$ 175 A; F = 10 kHz. Time parameters of this triangular current pulse are practically optimal in the sense that they provide maximum effective value of current at its given average value (see Section 1).

In discussion of the results of calculation of characteristics of modulated current arc, we will give preference to analysis of processes running in arc anode region, disregarding a number of interesting features of nonstationary thermal, gas-dynamic and electromagnetic processes in its column. Let $j_{\text{a}}(r,\ t)$ be the distribution of axial component of current density at the anode, calculated using arc model [17]. Let us first consider the change in time of axial value of current density $j_{\text{a}}(0,\ t)$ per one modulation period. In Figure 5 the change of the above characteristic in time (curve *1*) is given in comparison with values of axial density of current for stationary arcs at currents $I = I_2$, I_{A}, I_1 (curves *2*, *3*, *5*, respectively). The same figure gives axial value of current density averaged over the modulation period (dotted curve *4*). Figure 6 at gives the distributions of current density at the anode in different moments of time for the leading (Figure 6, *a*) and trailing (Figure 6, *b*) fronts of the pulse. Dashed lines

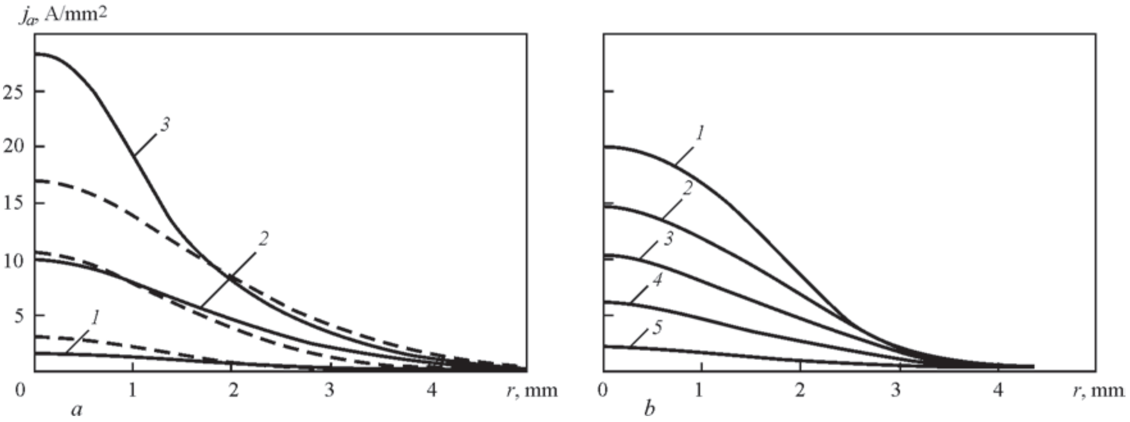

Figure 6. Distribution of current density at the anode at different moments of time: *a* — leading front (*1* — $t = 0$, $I = 30$ A; *2* — $t = 10$ μs; $I = 187$ A; *3* — $t = 20$ μs, $I = 345$ A); *b* — trailing front (*1* — $t = 30$ μs, $I = 282$ A; *2* — $t = 40$ μs; $I = 219$ A; *3* — $t = 50$ μs, $I = 156$ A; *4* — $t = 60$ μs, $I = 93$ A; *5* — $t = 70$ μs, $I = 30$ A)

in Figure 6, *a* show the respective distributions for constant current arc at $I = 30$, 140 and 345 A.

Before going over to analysis of nonstationary nature of variation of electric current density at the anode, shown in Figures 5, 6 we will give a general description of mode of arcing with high-frequency current modulation. According to the accepted terminology, at current modulation electric processes run in the quasi-stationary mode, if their characteristics change periodically with current modulation frequency, and this change is realized in the mode of successive change of stationary states, corresponding to constant current, which coincides in its magnitude with instantaneous value of modulated current. In the case considered here, the first of these conditions is fulfilled already after feeding the first 5–6 pulses. The second condition, however, is not satisfied at modulation frequencies of 10 kHz. This is clearly demonstrated by the data shown in Figures 5, 6. Effect of pronounced nonstationary nature of variation of electric current density at the anode is manifested in that the maximum value of $j_a(0, t)$ (see Figure 5, curve *1*) is approximately 1.5 times higher than axial density of current at the anode for stationary arc at current $I = I_2 = 345$ A. The same effect is manifested also in distribution of electric current at the anode (see Figure 6, curve *3* and respective dashed curve). Therefore, we can conclude that in the considered case the arc burns in a nonstationary mode, accompanied by a significant increase of current density at the anode.

The simplest explanation for this effect may be that the rapidly changing current at the pulse leading front (see Figure 4) is passed through the current channel of arc column, the size of which does not have enough time to follow the change of $I(t)$, because of inertia of gas-dynamic processes in arc plasma, and preserves the dimensions, close to those which it had at the start of modulation period (at small value of current). As shown by analysis of other dynamically changing characteristics of arc discharge, such a mechanism of increasing electric current density at the anode is not the only one, i.e. there also exist other causes behind the extreme nature of $j_a(0, t)$ variation, and these causes are associated not with arc column, but with near-anode plasma region.

We will consider changes of radial distribution of near-anode plasma temperature $T_a(r, t)$ (Figure 7, *a*) in time within the first 40 μs from the moment of the pulse start, of which 20 μs falls on its leading front. At current $I = 30$ A ($t = 0$) axial value of near-anode plasma temperature is equal to 7736 K (see Figure 7, *a*, curve *1*). At current increase up to 345 A ($t = 20$ μs) the temperature rises up to 8960 K and continues rising over the next 10 μs (temperature distributions at these moments of time are represented in Figure 7, *a* by curves *2*, *3*). Notably, $T_a(r, t)$ increase is limited by a circle, the radius of which does not exceed 3 mm;

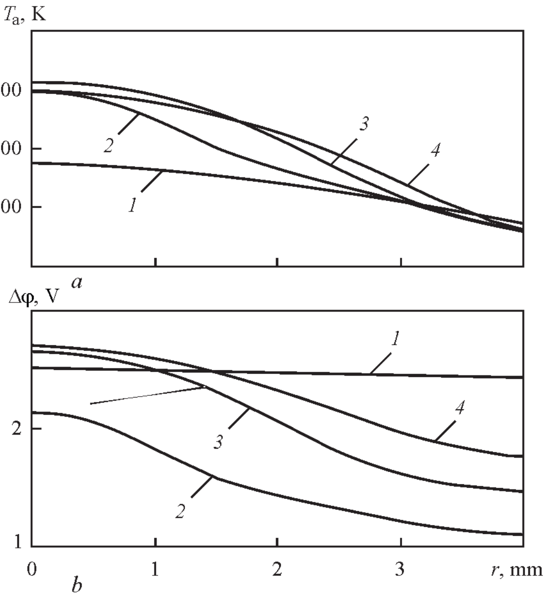

Figure 7. Distribution of temperature (*a*) and potential (*b*) of near-anode plasma along its boundary with arc column: *1* — $t = 0$, $I = 30$ A; *2* — $t = 20$ μs, $I = 345$ A; *3* — $t = 30$ μs, $I = 282$ A; *4* — $t = 40$ μs, $I = 219$ A

at greater values of r near-anode plasma temperature does not change compared to the temperature it has reached during the pause (as a result of inertia of thermal and gas-dynamic processes in arc column).

Local temperature rise (in time and space) leads to a change of radial distribution of potential drop across the anode $U_a(r, t) = -\Delta\varphi(r, t)$, which depends on distribution of electric current density at the anode and near-anode plasma temperature [16]. This dependence is illustrated by presented in Figure 7, *b*, results of calculation of the dynamics of distribution of value $\Delta\varphi$, which actually is the near-anode plasma potential on the boundary with arc column, under the condition that anode surface potential is taken to be constant and equal to zero.

At low current $I = 30$ A ($t = 0$) the boundary of near-anode plasma and arc column is practically isopotential ($\Delta\varphi \approx 2.5$ V — Figure 7, *b*, curve *1*) so that current density vector in it is directed along a normal to anode surface. With increase of axial value of temperature of near-anode plasma by more than 1000 K (see Figure 7, *a*, curves *2–4*), this boundary becomes significantly non-isopotential, and in such a way that potential value decreases along the anode surface, reaching a gradient of about 1 V at 3 mm distance from the center of anode binding region. Non-uniform distribution of anode potential drop in near-anode plasma results in appearance of radial component of current density vector, directed from the center to the periphery of anode region, which enables radial unloading of current flowing out of the anode. The effect of local increase of current density at the anode is achieved exactly due to current flowing more readily out of the anode into arc plasma. The effect of arc current contraction at the anode due to additional local heating of arc plasma was found for the first time in study [8] under the conditions of hybrid (TIG + CO_2-laser) welding.

At the conclusion of this analysis, we will mention one more possible cause for current density increase at high-frequency modulation of current (see Figures 5, 6). In the region of low temperatures of argon plasma (of the order of 7–12 kK), its specific electric conductivity rises noticeably with temperature increase, while at temperatures above 20 kK plasma electric conductivity is weakly dependent on temperature. Thus, increase of arc plasma temperature at current rise only slightly changes the electrophysical properties of arc column, and at the same time creates a region of increased electric conductivity in paraxial regions of near-anode plasma. Such a feature can also promote increase of current density in the central part of the region of anode binding of the arc.

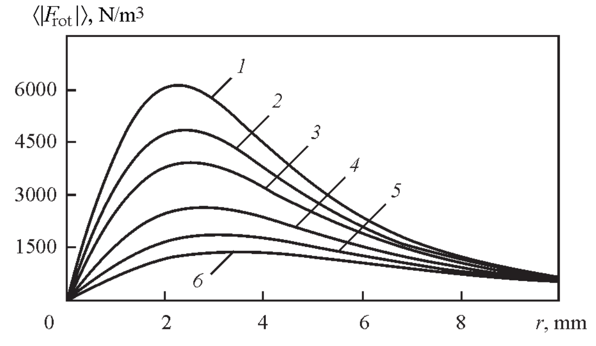

Figure 8. Distribution of effective value of vortex component of electromagnetic force in different axial sections of the plate being welded: *1* — $z = 0$; *2* — 0.25; *3* — 0.5; *4* — 1.0; *5* — 1.5; *6* — 2.0 mm

Now let us go back to the problem of force impact of modulated current on the metal being welded. Calculation of current distribution in 10 mm plate being welded was performed using axisymmetric (2D) model of electric processes described in [14]. For each moment of time t_k during one period of current modulation ($t_k \in \in [0, \tau]$, $k = 1$–100) distribution of axial current density $j_a(r, t_k)$ was assigned on the anode surface ($z = 0$), which was determined on the basis of a computer model of nonstationary arc for a current pulse, shown in Figure 4. On the plate lower surface ($z = 10$ mm) scalar potential of electric field was taken to be constant (equal to zero); on the axis of symmetry and at sufficiently great distance from the axis ($R = 50$ mm) the radial component of current density vector was taken to be zero. Vector field of current densities $j(r, z, t_k)$ was calculated at each moment of time t_k, which was used to find $I^2(r, z, t_k)$ distribution. Average value of the respective characteristic $\langle I^2(r, z)\rangle$ was calculated by the method of numerical integration by quadrature formula of a rectangles. Effective value of vortex component of electromagnetic force was found from formula (5), and magnetic pressure created by this force — by formula (6). Results of calculation of the above characteristics are given in Figures 8, 9.

As volume density of vortex component of electromagnetic force $\vec{F}_{rot}(r, z)$ is in quadratic dependence on magnetic field intensity $H_\theta(r, z)$ (see [14]), the nature of radial distribution of $\left\langle\left|\vec{F}_{rot}(r, z)\right|\right\rangle$ (see Figure 8) is similar to $H_\theta(r, z)$ distribution, including the position of radius, in which maximum of vortex component of the force is reached. Maximum value of $\left\langle\left|\vec{F}_{rot}(r, z)\right|\right\rangle$ decreases rapidly with greater distance from the anode surface in-depth of the weld pool, becoming more than 4 times smaller at $z = 2$ mm. Magnetic pressure field turns out to be even more concentrated near the surface of metal being welded (see Figure 9). Its largest gradient is reached in a melt layer of 1 mm thickness, located directly under the pool surface.

It is of interest to compare magnetic pressure and its axial gradient in welding by modulated current with respective characteristics for constant current $I =$ const. In Figures 10, 11 the results of the respective

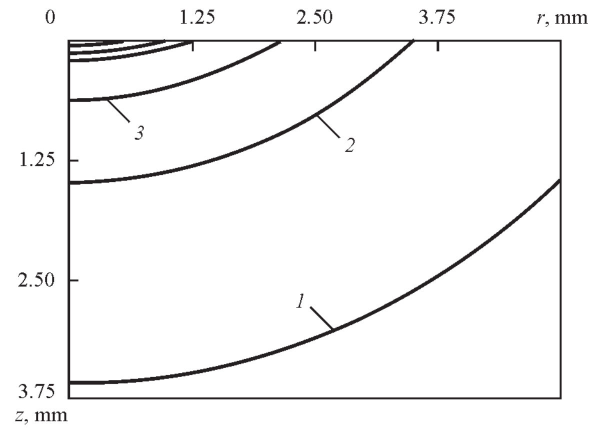

Figure 9. Isobars of averaged magnetic pressure in the weld pool: *1* — $\langle P_{\text{mag}}(r, z)\rangle = 5$; *2* — 15; *3* — 30 Pa (curves in the upper part of the Figure correspond to 45, 50 and 55 Pa)

calculations at $I = I_{\text{A}} = 140$ A and $I = I_{\text{E}} = 175$ A are given in comparison with characteristics for the case of modulated current. As expected, magnetic pressure at modulated current welding is significantly higher than magnetic pressure of constant current, coinciding in value with average value of modulated current. However, $\langle P_{\text{mag}}\rangle$ exceeding P_{mag} at $I = I_E = 175$ A requires some clarification. The cause for this excess are dynamic processes in the arc, flowing in high-frequency modulated current welding, in particular extreme behaviour of current density on the pulse leading front (see Figures 5, 6).

Note that in the considered case maximum value of magnetic pressure is equal to less than 0.1 % of atmospheric pressure. However, because of its high concentration near the weld pool surface, the radial, and particularly, axial components of magnetic pressure gradient turn out to be quite significant (see Figures 9, 11).

Let us illustrate the last statement. For this purpose we will use the equation of movement of viscous incompressible fluid in the cylindrical system of coordinates (r, z), which is the projection of the balance of volume forces on axis z. We will assume melt movement to be stationary, and pressure in the liquid phase to be averaged magnetic pressure $\langle P_{\text{mag}}\rangle$. Let us denote vector of liquid metal movement speed as $\vec{V}(r, z)$; and ρ as its density. As a result, we obtain:

$$\rho\left(V_r\frac{\partial V_z}{\partial r} + V_z\frac{\partial V_z}{\partial z}\right) = -\frac{\partial\left\langle P_{\text{mag}}\right\rangle}{\partial z} + \nu\Delta V_z. \tag{7}$$

We will take into account that at $r = 0$, in view of the conditions of axial symmetry of the considered flow, radial component of speed vector is equal to zero; then, neglecting the forces of viscous friction, from (7) we obtain

$$\frac{\rho}{2}\frac{\partial\bar{V}_z^2}{\partial z} = -\frac{\partial\left\langle\tilde{P}_{\text{mag}}\right\rangle}{\partial z},$$

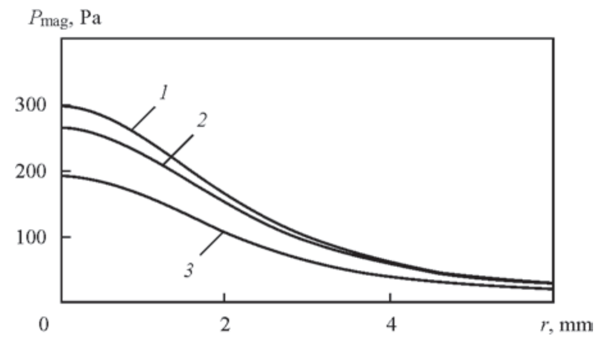

Figure 10. Distribution of magnetic pressure on weld pool surface: $\langle P_{\text{mag}}\rangle$ for an arc of modulated current (curve *1*); P_{mag} for stationary arcs at $I = I_{\text{E}} = 175$ A (curve *2*) and $I = I_{\text{A}} = 140$ A (curve *3*)

which yields Bernoulli equation for an ideal liquid:

$$\frac{\rho}{2}\left[V_z^2(0, z) - V_z^2(0, 0)\right] = \left\langle P_{\text{mag}}(0, 0)\right\rangle - \left\langle P_{\text{mag}}(0, z)\right\rangle.$$

As axial component of speed of metal movement on pool surface ($z = 0$) can be considered equal to zero, Bernoulli equation yields a simple formula for approximate estimation of axial speed of melt flowing on the pool axis of symmetry ($r = 0$):

$$V_z(0, z) = \sqrt{\frac{2\left(\left\langle P_{\text{mag}}(0, 0)\right\rangle - \left\langle P_{\text{mag}}(0, z)\right\rangle\right)}{\rho}}. \tag{8}$$

Results of calculation by this formula for steel, given in Figure 12, are indicative of the fact that quite intensive downward (directed towards pool bottom) melt flow arises in the weld pool under the impact of magnetic pressure gradient, which is capable of transporting overheated metal from the hottest subsurface region in-depth of the melt, and thus increasing penetration depth, this effect being the most pronounced at pulse modulation of welding current.

Discussion of results. Effective value of modulated current does not directly determine the number of charges, transferred per a unit of time through the conductor cross-section, but is an indirect parameter, which characterizes thermal and force impact of current on the conducting medium in comparison with the impact of constant current of the respective magnitude.

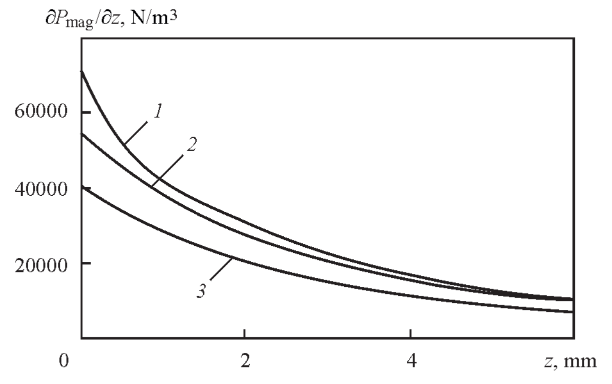

Figure 11. Distribution of axial value of axial component of magnetic pressure gradient: *1* — $I = I(t)$ (modulated current): *2* — $I = I_{\text{A}} = 140$ A; *3* — $I = I_{\text{E}} = 175$ A

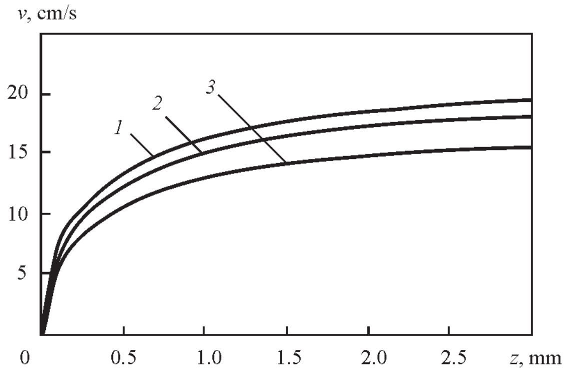

Figure 12. Axial change of axial component of the vector of weld pool metal movement speed (ρ = 7040 kg/m^3, designations on the curves are the same as in Figure 11)

However, these two kinds of impact are exactly the most significant ones for the technological results of arc welding, primarily, in terms of their influence on the depth and shape of metal penetration. Therefore, theoretical analysis of processes running in arc plasma, and in the metal being welded, appears to be very important for revealing the hidden capabilities of TIG welding with high-frequency pulse current modulation.

Conducted in section 1 analysis of the dependence of effective value of modulated current on modulation mode parameters is indicative of the fact that this characteristic is independent of modulation frequency, and is determined only by the shape and relative duration of current pulses. This almost obvious result is also valid for other pulse shapes, different from the trapezoidal one considered here. At selected value of average current, the highest effective value of current can be ensured through appropriate selection of time parameters of pulse modulation, and, therefore, greater force and thermal impact of modulated current both on arc plasma, and on weld pool metal. It should be noted that effective value of modulated current, as its integral characteristic, does not uniquely define thermal power of the arc discharge, as arc voltage also depends on current, changing during current pulse passage. In [19] it is shown that dynamic volt-ampere characteristic of nonstationary arc forms a hysteresis loop (see also [13]), enclosing (Figure 13) the volt-ampere characteristic of constant current arc. The shorter the duration of pulse leading front, the greater the loop of hysteresis loop, and, therefore, the greater the difference between the power of nonstationary arc and that of constant current arc, coinciding in magnitude with effective value of modulated current. Therefore, in high-frequency arc welding effective value of arc power should be determined by averaging the product of instantaneous values of current and voltage. At digital measurement of current and voltage with computer recording of signals, determination of average electric power of modulated current is not difficult. Theoretical analysis of this characteristic, however, requires use of arc discharge model with description of both arc column, and its near-electrode regions. Investigations in this direction are still to be performed, including experimental ones.

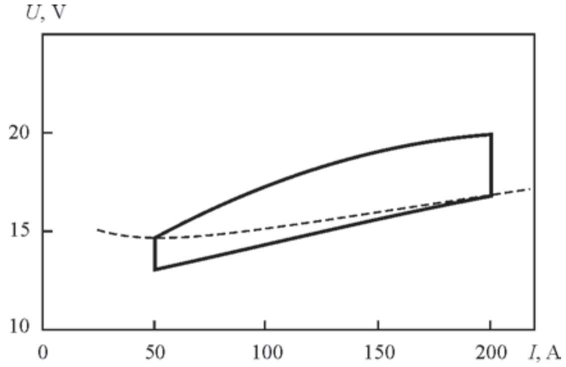

Figure 13. Dynamic volt-ampere characteristic of stationary argon arc 3 mm long with 20 μs duration of the pulse leading front

The conclusion that effective current value is independent of modulation frequency does not at all mean that value *F* has no influence on thermal and hydrodynamic processes, running in the metal being welded. In the second section it is established that force interaction of modulated current with intrinsic magnetic field is determined not by square of effective current value, but by its analog distributed in the metal volume, which is value $\langle I^2(r, z)\rangle$ — square of effective value of current flowing in a circle of radius *r*. This characteristic is highly dependent on modulation frequency *F*, as at high-frequency modulation of current by pulses with a steep leading front $\langle I^2(r, z)\rangle$ distribution is influenced by the above-described dynamic processes in the arc column and anode region, manifested in extreme distribution of current density at the anode (see Figures 5, 6). This, eventually, determines the difference between the force impact on the metal being welded of the arc with pulse current modulation and arc at constant current, coinciding by magnitude with effective value of modulated current (see Figures 11, 12).

It should be noted that given in this work results of calculations of the characteristics of electromagnetic processes in the metal being welded, were obtained in the assumption that the sample being welded is firmly pressed against the copper backing (electric potential of the sample lower surface is taken to be constant). Other variants of sample grounding were also considered during performance of computational experiments. Here, the pattern of current distribution in the metal being welded was cardinally different, depending on the position of local grounding relative to arc axis. Despite that, quantitative characteristics of force impact of modulated current on the metal being welded, given in the second section, remain valid for different connection diagrams. This result is due to high concentration of the field of magnetic pressure in the subsurface layer of weld pool metal approximately 1 mm thick (see Figure 9). In this layer distribution of current density and configuration of current lines are determined only by distribution of electric current density on the pool surface and are weakly dependent on the pattern of current spreading in the entire sample being welded.

In work [14] it is shown that technological means, providing a reduction of the size of the arc anode binding region (increase of electric current density on weld pool surface) in TIG welding, promote an increase of axial component of magnetic pressure in paraxial regions of the pool, and lead to intensification of downward flow of the melt, respectively, thus facilitating increase of penetration depth of the metal being welded. Analysis of effective values of electromagnetic characteristics of nonstationary arc in TIG welding performed in this study, gives grounds to assert that application of high-frequency pulse modulation of welding current is one of such technological means.

Finally, we will note one more important feature of the impact of vortex component of the Lorentz force on formation of magnetic pressure field in the weld pool. The action of centripetal force $\vec{F}_{\rm rot}(r, z)$, as well as the distribution of magnetic field intensity $H_\theta(r, z)$, extends to unlimited space. Having reached the maximum value (see Figure 8), both these characteristics of electromagnetic field tend to zero as $1/r$. On the other hand, magnetic pressure in the weld pool forms under the impact of just that part of force $\vec{F}_{\rm rot}(r, z)$, , which is applied to molten metal; now the rest of the force is balanced by elastic reaction of the solid phase. Therefore, the smaller the pool cross-section, the smaller the fraction of welding current flowing through it, and the lower its force impact, respectively. This, on the whole, correct conclusion, is not obvious in the case, when reduction of pool cross-section is due to electric current contraction on anode surface under the impact of additional technological factors, such as application of activating fluxes, special shielding gas mixtures, or focused laser radiation (hybrid TIG + CO$_2$-laser welding), as at constriction of the current channel on anode surface the fraction of current flowing through the weld pool becomes greater. Clarifying the physical features of force impact of arc current under the conditions of this alternative is the subject of further research. It is also of interest to study the possibility of increasing the force impact of arc current on weld pool metal due to dynamic effects, arising in electric current density distribution on anode surface at passing of very steep leading front of the pulse. Therefore, another object of further studies are dynamic processes in the arc discharge and metal being welded at current modulation by rectangular pulses, which, as is shown in the first section, have an advantage over triangular pulses in terms of effective current value.

1. Leitner, R.E., McElhinney, G.H., Pruitt, E.L. (1973) An investigation of pulsed GTA welding variables. *Welding J., Res. Suppl*., **9**, 405–410.
2. Omar, A.A., Lundin, C.D. (1979) Pulsed plasma-pulsed GTA arcs: A study of the process variables. *Ibid*., **4**, 97–105.
3. Cook, G.T., H.E.E.H. EASSA (1985) The effect of high-frequency pulsing of a welding arc. *IEEE Transact. Ind. Appl*., 1A-21, **5**, 1294–1299.
4. Kolasa, A., Matsunawa, A., Arata, Y. (1986) Dynamic characteristics of variable frequency pulsed TIG arc. *Transact. of JWRI*, 15(**2**), 173–177.
5. Saedi, H.R.,Unkel, W. (1988) Arc and weld pool behavior for pulsed current GTAW. *Welding J., Res. Suppl*., **11**, 247–255.
6. Kim, W.H., Na, S.J. (1998) Heat and fluid flow in pulsed current GTA weld pool. *Int. J. Heat and Mass Transfer,* 41(**21**), 3213–3227.
7. Wu, C.S., Zheng, W., Wu, L. (1999) Modelling the transient behaviour of pulsed current tungsten-inert-gas weld pools. *Modelling Simul. Mater. Sci. Eng*., 7(**1**), 15–23.
8. Onuki, J., Anazawa, Y., Nihei, M. et al. (2002) Development of a new high-frequency, high-peak current power source for high constricted arc formation. *Jpn. J. Appl. Phys*., **41**, 5821–5826.
9. Traidia, A., Roger, F., Guyot, E. (2010) Optimal parameters for pulsed gas tungsten arc welding in partially and fully penetrated weld pools. *Int. J. Therm. Sci*., **49**, 1197–1208.
10. Traidia, A., Roger, F. (2011) Numerical and experimental study of arc and weld pool behaviour for pulsed current GTA welding. *Int. J. Heat and Mass Transfer*, **54**, 2163–2179.
11. Qi, B.J., Yang, M.X., Cong, B.Q. et al. (2013) The effect of arc behavior on weld geometry by high-frequency pulse GTAW process with 0Cr18Ni9Ti stainless steel. *Int. J. Adv. Manuf. Technol*., **66**, 1545–1553.
12. Yang, M., Yang, Z., Cong, B. et al. (2014) A study on the surface depression of the molten pool with pulsed welding. *Welding J., Res. Suppl*., 93(**8**), 312–319.
13. Sydorets, V.N., Krivtsun, I.V., Demchenko, V.F. et al. (2016) Calculation and experimental research of static and dynamic volt-ampere characteristics of argon arc with refractory cathode. *The Paton Welding J*., **2**, 2–8.
14. Demchenko, V.F., Krivtsun, I.V., Krikent, I.V. et al. (2017) Force interaction of arc current with self-magnetic field. *Ibid*., **3**, 15–24.
15. Landau, L.D., Lifshits, E.M. (1982) Electrodynamics of continuums. Vol. 8. *Teoreticheskaya Fizika*, Moscow: Nauka.
16. Krivtsun, I.V., Demchenko, V.F., Krikent, I.V. (2010) Model of the processes of heat, mass and charge transfer in the anode region and column of the welding arc with refractory cathode. *The Paton Welding J*., **6**, 2–9.
17. Krivtsun, I.V., Krikent, I.V., Demchenko, V.F. (2013) Modelling of dynamic characteristics of a pulsed arc with refractory cathode. *Ibid*., **7**, 13–23.
18. Krivtsun, I.V., Krikent, I.V., Demchenko, V.F. (2015) Interaction of CO$_2$-laser radiation beam with electric arc plasma in hybrid (laser + TIG) welding. *Ibid*., **3/4**, 6–15.
19. Sokolov, O.I., Gladkov, E.A. (1977) Dynamic characteristics of free and constricted alternating current welding arcs with non-consumable electrode. *Svarochn. Proizvodstvo*, **4**, 3–5.

Received 03.07.2017

doi.org/10.15407/tpwj2017.08.02

BRAZING FILLER METAL WITHOUT BORON AND SILICON FOR BRAZING OF HEAT-RESISTANT NICKEL ALLOY

S.V. MAKSYMOVA, V.V. VORONOV and **P.V. KOVALCHUK**
E.O. Paton Electric Welding Institute, NASU
11 Kazimir Malevich Str., 03680, Kiev, Ukraine. E-mail: office@paton.kiev.ua

The use of nickel brazing filler metals, containing boron and silicon as depressants, provides a good wetting of material brazed, allows a significant reduction in brazing temperature, but leads to formation of brittle phases and low-melting eutectics in the brazed welds. This work shows the possibility of forming brazed joints of cast heat-resistant nickel alloy ZhS6U applying brazing in vacuum with use of multicomponent nickel brazing filler metals which do not contain boron and silicon as depressants. Applying the method of high-temperature differential thermal analysis in atmosphere of high-purity helium, the temperatures of liquidus and solidus of brazing filler metals were determined. The results of metallographic and micro-X-ray spectral examinations on studying the features of structure formation of brazed welds are presented. The long-term strength of the brazed joints was evaluated. It is shown that nickel brazing filler metals, containing a large concentration of zirconium, are characterized by a lower melting point, however, in the brazed welds the precipitations of the phase $Ni(Me)_xZr$ are formed. It was determined that decrease in the concentration of zirconium in the nickel brazing filler metal allows avoiding the formation of intermetallic phase enriched in zirconium and obtaining a solid nickel-based solution as the predominant phase in the weld. The results of tests of flat brazed (butt) specimens on long-term strength, carried out at the elevated temperature of 975 °C and the stress of 140 MPa, showed that the joints preserve integrity and do not fracture after 41–60 h of testing. It is shown that zirconium can act as an alternative depressant (instead of mutual adding of boron and zirconium). 13 Ref., 3 Tables, 8 Figures.

Keywords: *vacuum brazing, heat-resistant nickel cast alloy, liquidus temperature, solidus, microstructure, multicomponent brazing filler metal, brazed joint, long-term strength*

Among the numerous heat-resistant materials applied in industry, the greatest attention is drawn to the alloys used for manufacture of parts of the hot tract of gas turbine engines, in particular, turbine blades. At the present time, in the overwhelming majority of cases, these are the high-alloy nickel alloys, in which solid-solution, carbide and intermetallic hardening are realized [1, 2]. During service, the parts of the hot tract of turbines, in the first turn guide and working blades, are subjected to corrosion, erosion and thermal fatigue fracture under the conditions of cyclically changing temperatures, centrifugal loads and the effect of combustion products of the gas turbine fuel. To extend the service life of these expensive parts, the repair technologies are used, for example, brazing [3–7]. In many cases, the brazing is the only possible way of joining.

The dispersion-hardened heat-resistant nickel alloys contain a large amount of alloying elements, respectively, and brazing filler metals, as a rule, also represent the complexly-alloyed systems on nickel base. They contain the components which provide the necessary high-temperature strength, heat resistance, resistance to high-temperature corrosion and oxidation and other characteristics of brazed joints. To decrease the melting point, the brazing filler metals are alloyed with the depressants.

Analysis of systems of existing high-temperature nickel brazing filler metals (Ni–Cr–Si, Ni–Cr–B, Ni–Cr–Si–B, Ni–Mn–Si, Ni–Mn–Cr–Si, Ni–Cr–Pd–Si, etc.) shows that they contain boron, silicon, manganese, palladium, zirconium and gafnium as depressants [5, 8, 9]. Thus, in the system Ni–Cr–Si, the reduction of liquidus temperature is achieved due to silicon, and in the system Ni–Cr–B, the liquidus is significantly influenced by boron. Applying the mentioned brazing filler metals, in the brazed welds the brittle intermetallic compounds and easily-melted eutectic phases, enriched in boron and silicon are formed in addition to the solid solution, which makes it difficult to obtain the high values of heat resistance [8–11]. It is possible to reduce the number of these phases applying a long-term heat treatment, which complicates the technological process of producing permanent joints.

The aim of this work is to create a composition of brazing filler metal for brazing heat-resistant nickel alloys with an acceptable interval of melting, which allows reducing or avoiding the formation of intermetallic phases, easily-melting eutectics and obtaining a chemical composition of the brazed weld close to the base material.

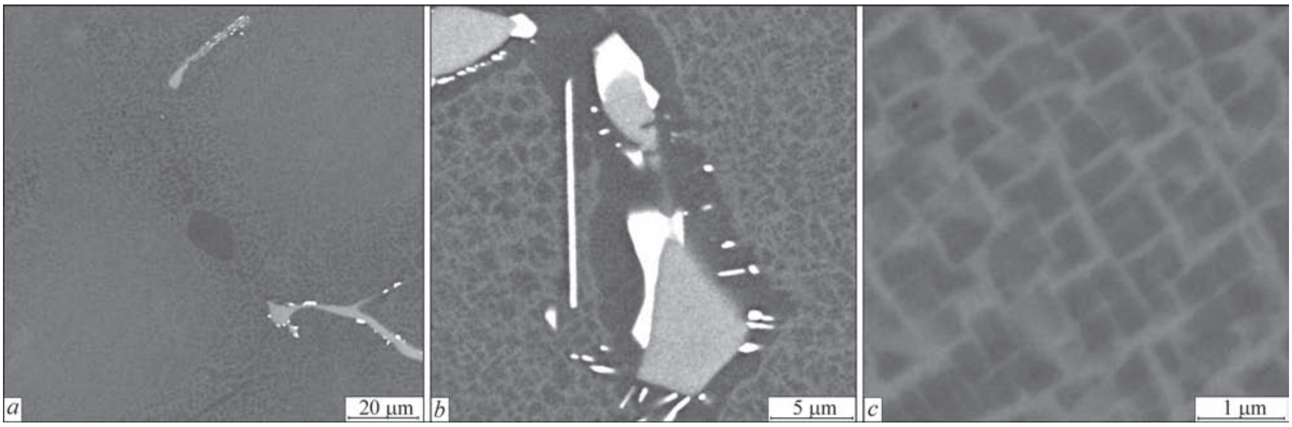

Figure 1. Microstructure of alloy ZhS6U: *a* — general view; *b* — carbide phases; *c* — (γ´ + γ)-structure

By analyzing a number of state diagrams of nickel with elements of IV–V groups of the periodic system, it can be noted that in this case it is impossible to distinguish a definite double base system for developing a brazing filler metal either due to the absence of a high-nickel eutectic with an acceptable melting temperature (the systems Ni–Ti, Ni–Nb), or in view of the extremely low solubility of the depressant element in nickel (the system Ni–Zr, Ni–Hf) [12].

The put task can be solved by applying complex multicomponent alloying, combining such elements as aluminum, zirconium and hafnium as depressants. To achieve a high fraction of solid solution in the brazed weld, it is necessary to minimize the content of elements having a low solubility in nickel.

As a base metal the cast plates of the high-alloyed heat-resistant nickel cast alloy ZhS6U (Ni–(8.0–9.5) Cr–(9.0–10.5)Co–(9.5–11.0)W–(5.1–6.0)Al–(2.0–2.9)Ti–(1.2–2.4)Mo–(0.8–1.2)Nb–1Fe–(0.13–0.02 C) were used. The total amount of elements (Al + Ti), which determine the high heat resistance of the alloy, is 7.1–8.9 wt.%. This alloy is referred to hard-to-weld one due to initiating of hot cracks in the heat-affected zone (HAZ) and weld during crystallization or subsequent heat treatment [9, 13]. The ZhS6U alloy is characterized by a coarse-grained heterophase structure, consisting of γ-solid solution, hardening γ´-phase, which is precipitated in the grain volume, carbide and boride phases (Figure 1, *a*, *b*). The amount of particles of γ´-phase in alloy matrix in the initial state (before service) is about 60 vol.% and is characterized by a cubic morphology (Figure 1, *c*). For investigations, the multicomponent brazing filler metals based on nickel, containing chromium, cobalt, tungsten and other elements, were melted by arc method on a cold substrate in argon. By applying the method of high-temperature differential thermal analysis (DTA) the temperatures of liquidus and solidus, as well as intermediate phase transformations of experimental alloys during heating were determined by using the thermal analyzer VDTA-8M3 in the atmosphere of high-purity helium at the heating rate of 40 °C/min.

Using the produced brazing filler metals, the brazing of specimens (at the liquidus temperature of each brazing filler metal) of the alloy ZhS6U was carried out in vacuum furnace SGV 2.4-2/15-I3 (rarefaction of working space was $1.33–10^{-3}$ Pa). The heating rate was about 12 °C/min, the holding time at the brazing temperature was 5 min.

The produced brazed specimens were cut perpendicularly to the brazed weld and according to standard procedure the microsections were manufactured. The microstructure of brazed joints and chemical composition of separate phases were investigated using the scanning electron microscope TescanMira 3 LMU, equipped with the energy dispersive spectrometer Oxford Instruments X-max 80 mm^2 (software package of INCA). The distribution of elements and shooting of microstructures were carried out in the back-scattered electrons (BSE), which allow examining the microsections without chemical etching. The micro-X-ray spectral method provides a high locality of examinations (up to 1 µm).

To carry out tests for long-term strength, the butt flat plates were brazed, which were subjected to heat treatment by the mode T = 1220 °C, τ = 4 h in order to homogenize the structure of brazed welds. Further, the special specimens of 80 mm length were cut from the brazed plates for testing on long-term strength at the elevated temperature. The width of test zone in the brazing area was 5 mm at the specimen thickness of

Table 1. Basic systems and intervals of melting brazing filler metals

Alloy number	Basic alloying system	Temperature, °C	
		T_S	T_L
1	Ni–Co–Cr–Ti–Nb–Al–(Me)–2Zr	1101	1231
2	Ni–Co–Cr–Ti–Nb–Al–(Me)–1Zr	1141	1259

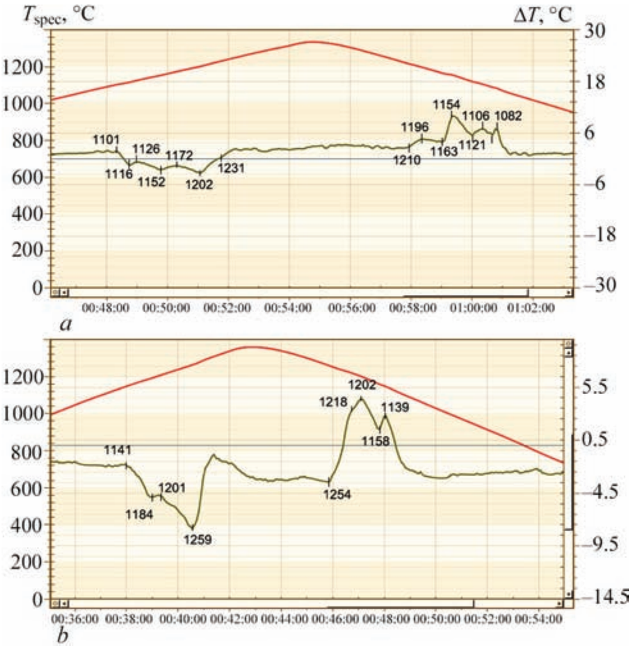

Figure 2. Curves of differential thermal analysis of brazing filler metals; No.1 (*a*) and No.2 (*b*)

4.5 mm. The tests were carried out at the temperature of 975 °C and the constant stress of 140 MPa.

As a result of carried out investigations, two promising brazing filler metals were selected based on the system Ni–Co–Cr–Me (Al, Ti, Nb, Zr) with different zirconium content (Table 1).

The results of high-temperature differential thermal analysis showed that alloy No.1, having an increased concentration of zirconium, is characterized by a wide interval (130 ° C) and a minimum melting temperature (Figure 2, *a*). The thermal effects obtained on the thermal curve indicate the presence of four phases in the initial alloy. The decrease in the concentration of zirconium (in alloy No.2) leads to decrease in a number of phases in the brazing filler metal and to increase in the temperature of solidus and liquidus (Figure 2, *b*). The temperature interval is narrowed to 118 °C.

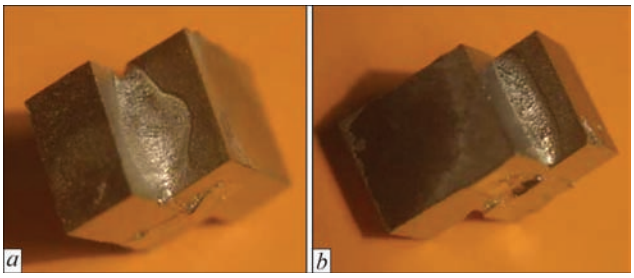

Figure 3. Appearance of overlapped joint, brazed applying brazing filler metal No.1: *a* — straight fillet; *b* — reverse fillet

The visual inspection of brazed joints of the heat-resistant alloy ZhS6U showed that when applying the brazing filler metal No.1 containing 2 % of zirconium, a good spreading and wetting of base metal is observed (Figures 3, *a*, *b*). The formation of complete fillet areas is provided, the defects on the specimens are absent, which confirms the results of further metallographic examinations (Figure 4).

The local micro-X-ray spectral analysis determined that brazed weld is characterized by a multiphase structure. The weld matrix is represented by grains of a solid solution based on nickel with a variable concentration of constituent elements, which is explained by liquation processes during crystallization. Along the grain boundaries of solid solution the separate single particles of a light phase based on tungsten (carbides), a nickel-based phase enriched in zirconium (21.78 %), a boundary eutectic γ′-phase on the basis of nickel with an increased concentration of aluminum and a nickel-based phase enriched in molybdenum, niobium and tungsten (Figure 5, *a*, *b*, Table 2) are observed.

In accordance with the state diagram of the binary system Ni–Zr, it can be assumed that the phase, enriched in zirconium, refers to intermetallic compound Ni_5Zr [12]. Due to the fact that the nickel brazing filler metal is multicomponent, it is most probable, that a complex intermetalic compound $Ni(Me)_xZr$ is formed in the brazed weld. It should be noted, that the volume fraction of this phase is insignificant.

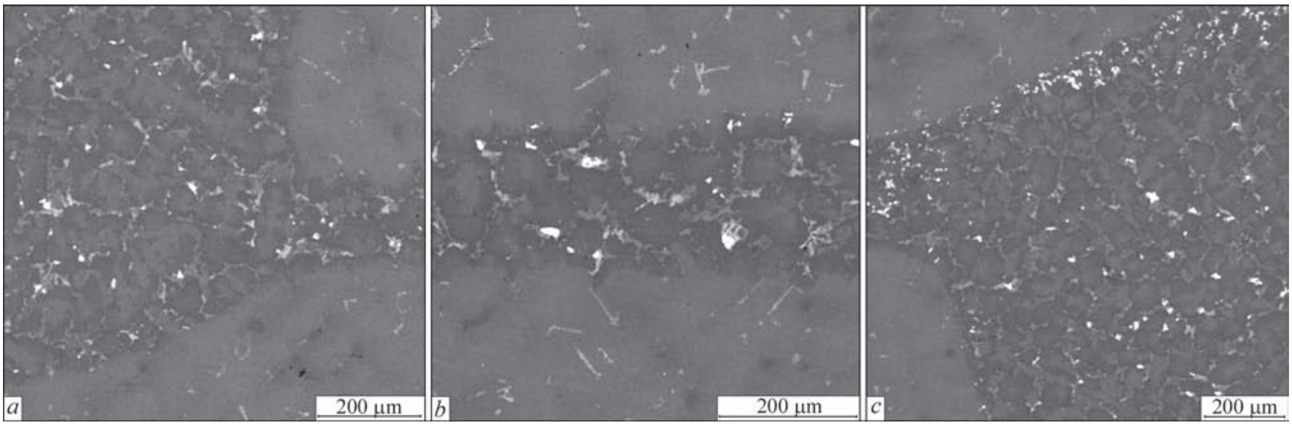

Figure 4. Microstructure of straight fillet (*a*); central weld zone (*b*) and reverse fillet (*c*)

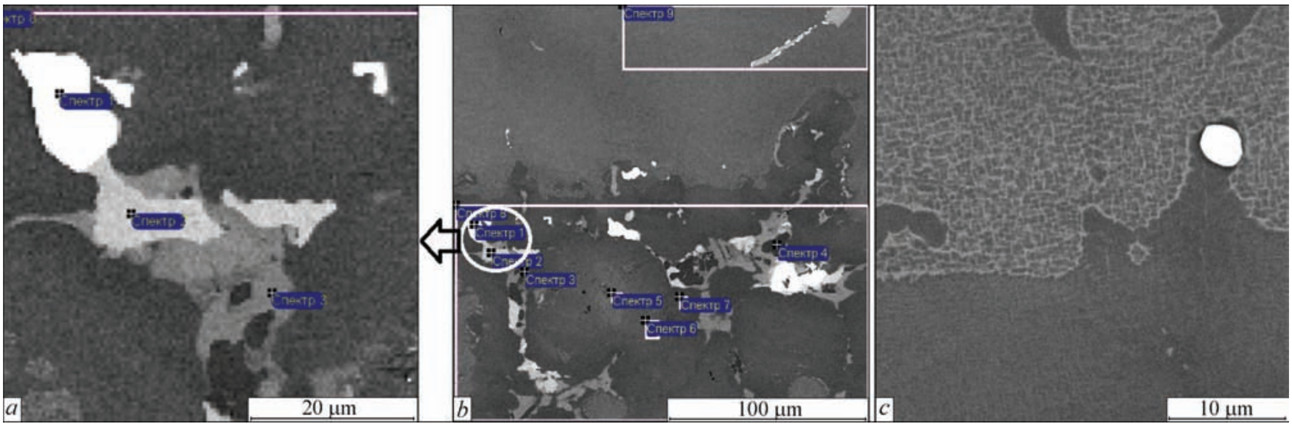

Figure 5. Microstructure of investigat of phases (*a*, *b*) and grain of (γ + γ´)-structure in weld of joint of alloy ZhS6U, brazing filler metal No.1

The dark precipitations of a nickel-based phase with an increased aluminum concentration (12.44 %) correspond to the boundary phase Ni_3 (Al, Ti, Zr, Nb), in which the aluminum atoms are replaced by γ´-forming elements. The investigations of a fine structure of the brazed weld (at a high resolution) showed the presence of γ´-hardening phase in a solid solution based on nickel, which is characterized by a cuboidal morphology and provides a heat resistance to the brazed weld (Figure 5, *c*).

In the fillet area the same structural components were revealed as in the brazed weld. The difference is that the phase enriched in tungsten is precipitated mainly along the brazing filler metal — base metal interface (Figure 4, *a*, *c*).

The reduced concentration of zirconium to 1 % in brazing filler metal No.2 allows avoiding the formation of a zirconium intermetallic compound in the brazed weld and in the fillet area. The formation of a dense, defect-free brazed weld with a thickness of about 100 μm and complete fillet areas is observed (Figure 6, *a*, *b*, *c*).

The structure of a brazed weld is similar to the structure of a fillet area (Figure 6, *b*, *c*). The matrix of a brazed weld is represented by a solid solution based on nickel with a variable concentration of constituent elements by the grain (Table 3).

The areas of (γ + γ´)-structure in weld metal are also observed (Figure 6, *d*). The formation of dispersed carbide phases based on tungsten is typical for both systems of the applied brazing filler metals. The elevated

Table 2. Concentration of elements in brazed joint using brazing filler metal No.1, wt.%

Number of spectrum	Al	Ti	Cr	Co	Ni	Zr	Nb	Mo	W
1	0.25	0.19	2.52	0.36	3.23	0.00	0.00	8.32	85.14
2	0.70	1.52	19.24	12.90	17.02	0.00	10.84	10.52	27.26
3	2.03	1.50	3.95	10.12	48.37	21.78	10.14	0.00	2.11
4	12.44	7.63	8.18	10.88	53.81	1.43	4.05	0.46	1.13
5	5.45	4.58	7.60	10.49	58.43	0.00	1.38	1.56	10.52
6	6.12	6.09	4.39	9.01	64.65	0.00	1.52	1.32	6.91
7	6.64	7.31	3.76	9.42	65.68	0.00	2.62	0.48	4.08
8	4.96	6.45	7.42	9.55	55.56	0.71	3.72	1.39	10.25
9	5.08	3.09	8.51	9.44	56.11	0.00	1.77	1.94	14.06

Table 3. Content of chemical elements in brazed weld of joint of alloy ZhS6U, produced using brazing filler metal No.2

Number of spectrum	Al	Ti	Cr	Fe	Co	Ni	Nb	Mo	W
1	0.19	0.19	3.41	0.00	0.64	3.08	0.00	13.57	78.92
2	0.98	1.31	17.88	0.20	12.95	18.02	14.36	11.68	22.62
3	14.04	5.18	8.82	0.00	9.96	56.62	3.07	0.61	1.70
4	7.16	4.89	3.73	0.00	8.23	67.23	2.57	1.38	4.81
5	7.21	4.99	7.97	0.34	9.57	56.72	5.74	1.80	5.65
6	5.33	3.75	11.04	0.00	10.50	54.70	3.75	2.90	8.03
7	5.49	3.42	8.92	0.19	9.51	58.45	2.46	1.51	10.06
8	5.43	2.27	9.57	0.16	10.41	58.93	0.00	1.30	11.93

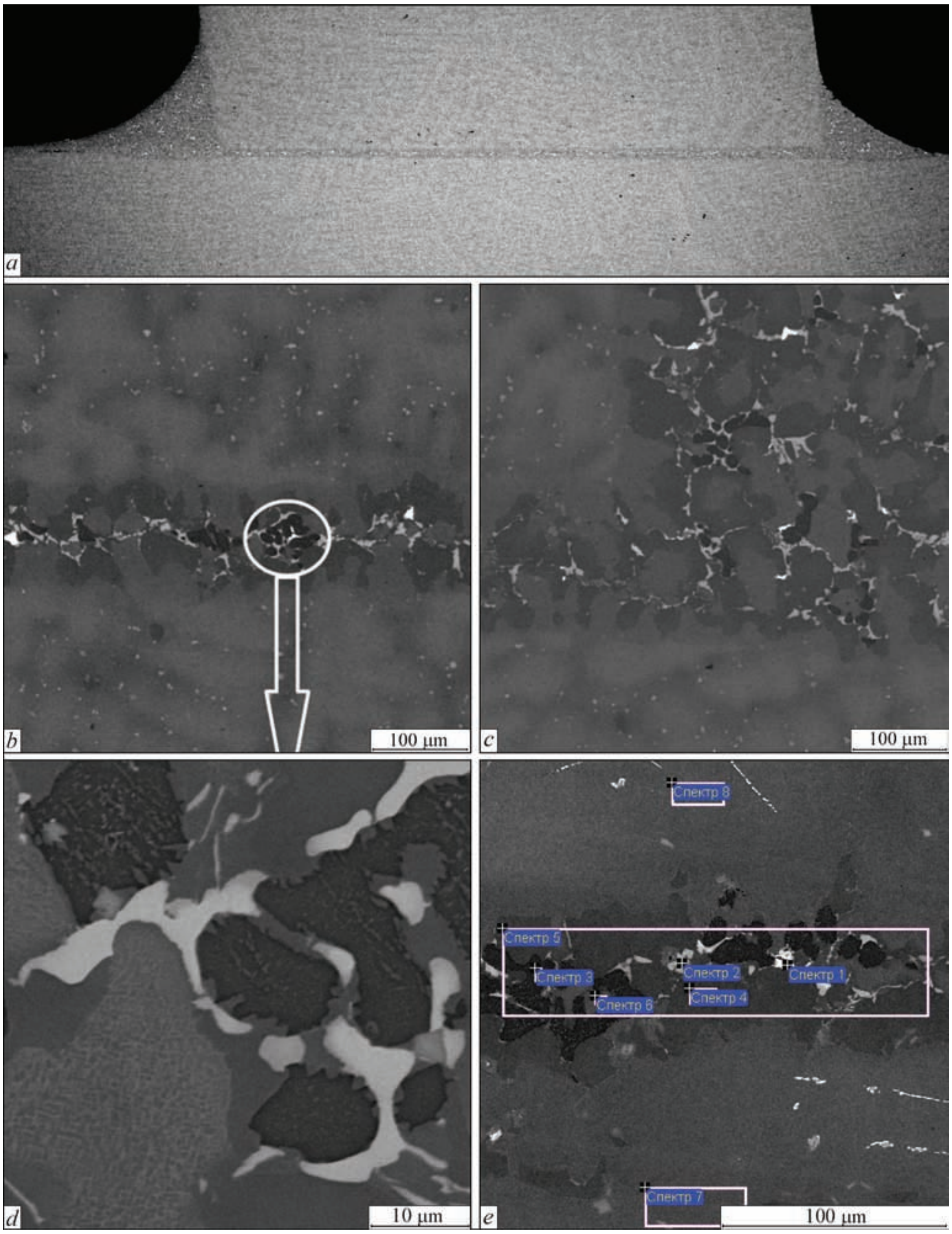

Figure 6. Microstructure of brazed T-joint produced using brazing filler metal No.2: *a* — general view; *b* — brazed weld; *c* — fillet area; *d* — phase in the interdendritic region; *e* — investigated phases in the brazed weld

temperature of brazing by the given filler metal promotes a partial dissolution of these phases in a solid solution, which leads to decrease in their number.

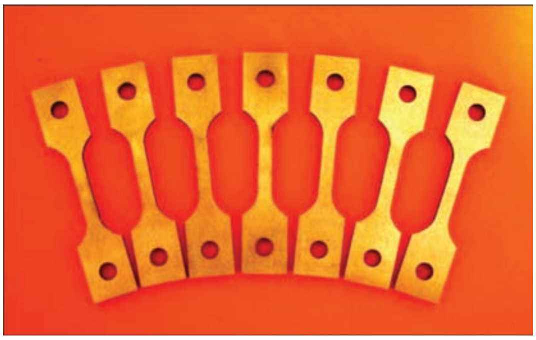

Figure 7. Appearance of flat butt specimens for tests on long-term strength

In the interdendritic regions of the brazed weld, a dark phase is observed, representing the boundary phase Ni_3 (Al, Ti, Zr, Nb), as in the previous case (Figure 6, *e*, spectrum 3, Table 3). In addition, a complex phase is formed on the base of system Ni–Nb, enriched in chromium, cobalt, molybdenum, tungsten (Figure 6, *e*, Table 3).

The obtained results of micro-X-ray spectral examinations showed that by applying the brazing filler metal No.2 the brazed welds contain a minimum amount of carbide phases, which positively affects the results of mechanical tests.

The butt brazed specimens (Figure 7), produced by applying brazing filler metal No.1, were characterized by minimal values of long-term strength and were fractured after 18–19 h at the test temperature T = 975 °C and the stress of 140 MPa (Figure 8). The specimens produced by applying brazing filler metal No.2 showed the better results: they preserved structural integrity and did not fracture after 41–60 h of tests (Figure 8). Based on the results of structural investigations and mechanical tests, a correlation between the microstructure of welds and the level of long-term strength of brazed joints is observed.

Conclusions

The carried out micro-X-ray spectral examinations of brazed joints of ZhS6U alloy produced applying a brazing in vacuum using multicomponent nickel brazing filler metals, not containing boron and silicon, showed the formation of quality, defect-free welds with predominance of a significant volume fraction of a solid nickel-based solution in the brazed weld.

It was found that the decrease in concentration of zirconium in nickel brazing filler metal (up to 1 %) provides a significant increase in the long-term strength of brazed joints at elevated temperature. Thus, at the test temperature of 975 °C and stress of 140 MPa, the specimens preserved structural integrity and did not fracture after 41, 48 and 60 h of testing.

Thus, the application of brazing filler metal with a minimum amount of zirconium provided 2–3 times increase in the duration of tests without fracture of brazed joints.

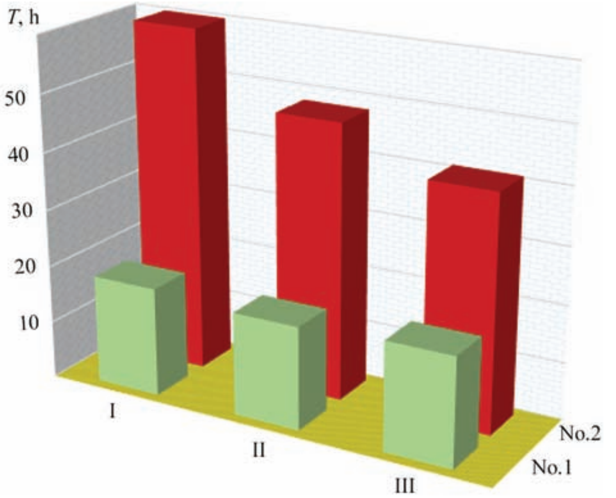

Figure 8. Results of tests on long-term strength of brazed joints produced using brazing filler metals No.1 and No.2 (I–III — test specimens)

1. Paton, B.E., Stroganov, G.B., Kishkin, S.T. et al (1967) *Heat-resistance of cast nickel alloys and their protection from oxidation*. Kiev: Naukova Dumka.
2. (2006) S.T. Kishkin effect. Ed. by E.N. Kablov. In: *Cast heat-resistant alloys: Transact*. Moscow: Nauka.
3. Khorunov, V.F., Maksymova, S.V., Ivanchenko, V.G (2004) Development of filler metals for brazing heat-resistant nickel- and titanium-base alloys. *The Paton Welding J*., **9**, 26–31.
4. Ermolaev, G.V., Kvasnitsky, V.V., Kvasnitsky V.F. et al. (2015) *Brazing of materials*. Mykolaiv: NUS.
5. Maksymova, S.V. (2007) Amorphous filler metals for brazing of stainless steels and titanium and structure of brazed joints. *Adgeziya Rasplavov i Pajka Materialov*, **40**, 70–81.
6. Khorunov, V.F., Maksymova, S.V. (2013) *Advanced in brazing. Science, technology and applications*. UK: Cambridge: Woodhead Publ. Ltd.
7. Khorunov, V., Maksymova, S., Samokhin, S. et al. (2001) Brazing filler metal containing Zr and Hf as depressants. In: *Proc. of 3rd Int. Conf. on High Temperature Capillarity HTC-2000* (Kurashiki, Japan 2000). Osaka.
8. Rabinkin, A. (2013) *Advances in brazing science, technology and applications*. UK: Cambridge: Woodhead Publ. Ltd.
9. Malashenko, I.S., Kurenkova, V.V., Belyavin, A.F. et al. (2006) Short-term strength and microstructure of brazed joints of alloy VJL12U produced using boron-containing brazing filler metal with addition of silicon. *Advances in Electrometallurgy*, **4**, 23–38.
10. Arafina, M.A., Medraja, M., Turnerb, D. (2007) Transient liquid phase bonding of Inconel 718 and Inconel 625 with BNi-2: Modeling and experimental investigations. *Mater. Sci. & Engin. A*, 447(**1/2**), 125–133.
11. Chaturvedi, M.C., Ojo, O.A., Richards, N.L. (2004) Diffusion brazing of cast Inconel 738 superalloy. *Advances in Technol.: Materials & Materials Proc*., 2(**6**), 206–213.
12. Massalski, T.B. (1990) *Binary alloy phase diagrams. American Society for Metals*. Metals Park: ASM International: CD).
13. Kurochko, R.S. (1982) Welding and brazing of heat-resistant materials of GTE hot section. *Aviats. Promyshlennost*, **8**. *http*://viam.ru/public/files/1982/1982-198570.pdf

Received 20.04.2017

doi.org/10.15407/tpwj2017.08.03

INCREASE OF BRITTLE FRACTURE RESISTANCE OF METAL OF HEAT-AFFECTED ZONE IN RAILWAY WHEEL SURFACING

O.A. HAIVORONSKYI, V.D. POZNYAKOV, L.I. MARKASHOVA,
A.S. SHISHKEVICH, V.A. YASHCHUK and A.V. KLAPATYUK
E.O. Paton Electric Welding Institute, NASU
11 Kazimir Malevich Str., 03680, Kiev, Ukraine. E-mail: office@paton.kiev.ua

Presented results are continuation of the complex investigations and refer to effect of low-temperature tempering, which is carried out in process of delayed cooling of products after welding, on mechanical properties and crack resistance of the joints of high-strength steel with 0.55–0.65 % carbon content. It is determined that tempering at 100 °C during four hours promotes rise of ductility property indices of quenched metal of heat-affected zone by 70 %, that of impact toughness 3 times, crack resistance 4.5 times, welded joint life duration 2 times. It is related with 1.5 times decrease of dislocation density in a volume of bainite and martensite laths as well as relaxation of stresses of II type. 14 Ref., 2 Tables, 7 Figures.

Keywords: *high-strength carbon steel, arc welding, heat-affected zone, low-temperature tempering, mechanical properties, brittle fracture, life*

One of the main problems in welding of high-strength steels is embrittlement of heat-affected zone (HAZ) metal due to formation in it of the quenching structures with low capacity to microplasma deformation. It is well known fact [1, 2] that ductile properties of quenched HAZ metal predetermine the possibility of cold cracks formation in the joints during welding as well as further workability of welded joints under effect of operation loads. Different technological methods are used in order to increase metal resistance to brittle fracture. The most efficient among them are thermal methods of welded joint treatment. Thus, the joints are preheated before welding, that allows regulating cooling rate and structure-phase composition of quenched HAZ metal. As a rule, this technological operation permits welding high-strength steel joints without cold cracks formation in them [3, 4]. However, preheating does not always efficiently influence HAZ metal resistance to brittle fracture under effect of external loading. In order to solve this problem the products after welding are subjected to tempering at temperatures from 250 to 600 °C. Thermal mode of tempering (heating rate, temperature and duration of holding, cooling rate) depends on content and level of steel strength, geometry of the products. Tempering allows stabilizing structure of welded joint metal as well as significantly decreases level of stresses in the structure [5, 6]. The disadvantages of the method are large energy expenses and necessity in special equipment use.

Issue of increase of brittle fracture resistance of quenched HAZ metal is the most pressing in welding of high-strength steel joints with 0.55–0.65 % carbon content. Work [7] shows that the value of critical coefficient of stress intensity K_{1c} has 4–8 times reduction for HAZ in comparison with metal in initial state. Also, it was determined that 2–3 times increase of brittle fracture resistance of quenched HAZ metal requires welding conditions providing formation of structure with prevailing portion of lower bainite. At that, content of hydrogen in HAZ metal should not exceed 0.2 ml/100 g. However, brittle fracture resistance of HAZ metal of high-strength carbon steel joints is significantly lower than that in base metal even at such welding conditions.

Today high-strength carbon steels are widely used in manufacture of railway wheels and bands for main transport, urban passenger transport and enterprises' transport. Carbon content in steels varies from 0.55 to 0.70 % and main alloying elements are silicon (up to 0.60 %) and manganese (up to 1.20 %) [8]. The wheels are worn in process of long-term operation and their restoration is carried out using surfacing methods. Surfacing technology assumes application of preheating and delayed cooling of wheel after surfacing. Thus, in restoration of the wheels, made of wheel steel of grade 2 (0.55–0.65 % C), a temperature of preheating makes 150 °C and after surfacing the wheels are cooled in heat chambers to 20–30 °C temperature during 4–5 h [9–10]. Necessity of application of delayed cooling as technological operation for deposited wheels was experimentally determined back in the 1990th. It allowed eliminating formation of cracks in deposited wheels at their restoration. At the same time it was also shown that increase of preheating temperature to 250 °C, but without delayed cooling of wheel after surfacing, does not provide significant effect in rise of crack resistance of restored wheels.

Aim of the present work is to determine effect of cooling conditions on structure, mechanical properties, brittle fracture resistance of HAZ metal and life of welded joints of high-strength steels with 0.55–0.65 % carbon content.

Materials and investigation method. Wheel steel of grade 2 (wt.% 0.58 C; 0.44 Si; 0.77 Mn; 0.10 Ni; 0.05 Cr; 0.012 S; 0.011 P) and carbon steel of 65G grade (0.65 C; 0.19 Si; 0.91 Mn; 0.18 Ni; 0.16 Cr; 0.017 S; 0.010 P) were used as materials for investigation.

The investigations were carried out on model and welded specimens. Work [7] in details describes the methods of preparation and testing of the specimens. Cooling rate of the model specimens in simulation of thermal-deformation welding cycle in 600–500 °C temperature interval ($w_{6/5}$) made 6 °C/s. Bainite structure (100 %) is formed at this cooling rate in HAZ metal of grade 2 wheel steel and bainite-martensite structure in steel 65G at relationship of portion of structural constituents 66/34. At that, part of the specimens were subjected to continuous cooling to room temperature, and another ones after reaching specific temperature were put in a furnace, hold at this temperature during set time and then they were cooled in air to 20 °C under natural conditions. Tempering (holding) mode of the specimens in the furnace was selected based on temperature of wheel tread after surfacing, which made approximately 260 °C, and time of wheel cooling in the heat chamber. Effect of tempering temperature of 200, 150, 100 and 50 °C at specimens' holding in the furnace during 1–4 h was investigated. Further they were used for making the specimens for static tension (GOST 1497), impact (GOST 9454), three-point bend (GOST 25.506) and metallographic investigations. 3 specimens for each mode of heat treatment were produced for mechanical tests, the results were averaged.

Structure of heat treated metal, distribution, dislocation density and specimen fractures were examined using optical microscopy, scanning and electron microscopy methods (SEM-515 of Philips Company, JEM-200CX of JEOL Company). Further, local deformation (ε_{loc}) and structural stresses of II type (τ_{loc}) were determined using experimentally found parameters of substructure depending on metal cooling conditions.

Fatigue fracture resistance of welded joints, cooling of which took place under different conditions, was evaluated at cyclic bending loading with symmetric cycle according to generally accepted methods [12]. The tests were carried out with the specimens of butt joints of 400×85 mm size, 10 mm (65G) and 20 mm (KS2) thickness, which were welded by mechanized submerged arc welding in 3 and 6 passes, respectively. Welding of the specimens was performed using Sv-08KhM wire of 2 mm diameter on the following mode, namely welding current 240–280 A, arc voltage 28–30 V and welding rate 24 m/h.

Specific welding heat input at such modes made 10 kJ/cm. Preheating of the joints up to 150 °C was carried out before welding in order to eliminate the possibility of cold crack formation. After cooling the welded specimens were tested on UMP-1 unit at symmetric loading cycle with 14 Hz frequency. Cycle stresses (σ_a) were measured in 60–120 MPa range. A criterion of evaluation was the maximum stresses (fatigue limit σ_{-1}) , at which welded joint has no fatigue cracks after 2 mln cycles of loading.

Results of investigation and their discussion. Influence of temperature and time of tempering on change of mechanical properties of HAZ metal was evaluated using model specimens of steel 65G. Figure 1 shows generalized results of carried tests. A zero point on diagram abscissa scale is a value of mechanical properties of HAZ metal, cooling of which was carried out continuously on welding thermal cycle.

It is determined that tempering in 50–200 °C temperature range during four hours does not have significant effect on change of strength properties of quenched HAZ metal (Figure 1, *a*). Short-term strength of metal lies in 1120–1090 MPa range and conventional yield strength of metal made 745–760 MPa. But, as can be seen from presented data, the temperature value of low tempering has more significant influence on ductility properties and impact toughness of HAZ metal, and this is nonequivalent (Figure 1, *b*, *c*). Relative elongation rises 1.3 times (from 6.7 to 9 %) and contraction increases 1.7 times (from 15 to 25.6 %) at tempering temperature 100 °C. At 150–200 °C tempering these indices gradually decrease to initial level. The same tendency is observed with impact toughness indices of HAZ metal, at that their rise is more significant. There is 3.1 times (from 7 to 22 J/cm^2) increase of *KCU* value at 20 °C testing temperature, 2.7 times (from 6 to 16 J/cm^2) at –20 °C and 2.5 times (from 5 to 12.3 J/cm^2) at –40 °C.

Taking into account received data, the further evaluation was performed as for influence of time of holding at 100°C temperature on change of ductility and toughness of HAZ metal of steel 65G. Figure 2 shows generalized results of these investigations. It is determined that significant increase of indices of ductile properties and impact toughness has already been observed at two hours tempering. Increase of time of

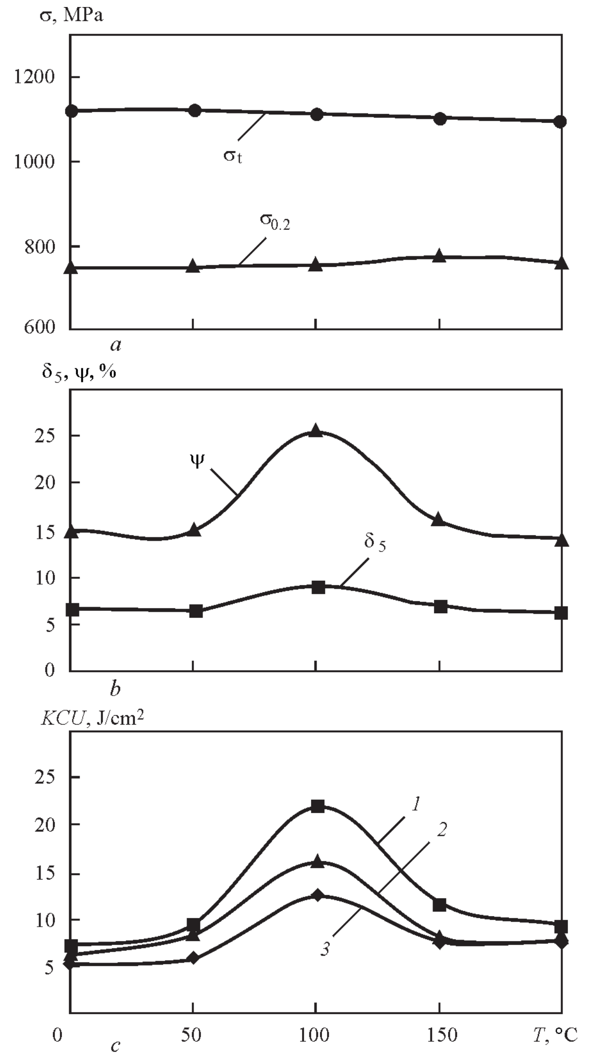

Figure 1. Effect of tempering temperature of 4 h duration on indices of strength (*a*), ductility (*b*) and impact toughness (*c*) of HAZ metal of steel 65G at testing temperature: *1* — 20; *2* — –20; *3* — –40 °C

metal holding at 100 °C to four hours promotes rise of its ductility by 16–22 %, indices of impact toughness at testing temperature 20 °C virtually do not change and at negative temperatures they increase by 21 and 40 %, respectively.

Obviously that enhancement of HAZ metal ductility as a result of delay of its cooling at 100 °C for 2–4 h can be related only with changes on substructural level since phase transformations to this moment in the majority of cases have already finished (temperature of start of martensite transformation 240 °C) [7]. Reduction of its ductility at higher tempering temperature (150–200 °C), apparently, takes place as a result of development of processes of carbon redistribution and precipitation of carbides in form of fine plates at bainite and martensite laths boundaries [5].

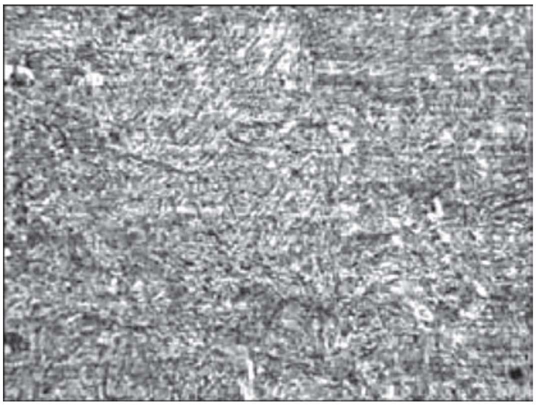

Figure 3. Microstructure of HAZ metal of steel 65G (×500)

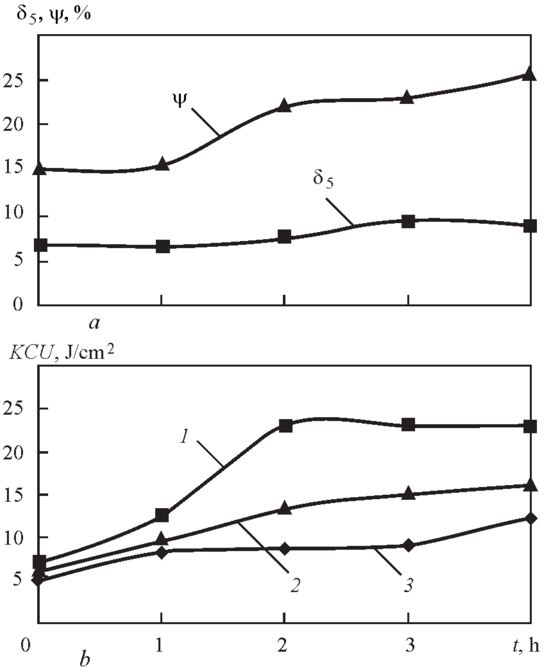

Figure 2. Effect of holding time at 100 °C tempering on indices of ductility (*a*) and impact toughness (*b*) of HAZ metal of steel 65G at testing temperature: *1* — 20; *2* — –20; *3* — –40 °C

Optical metallography methods did not detect substantial difference in the structure of quenched metal of the specimens, which were cooled under different conditions (Figure 3). For all cooling variants the structure is presented mainly by lower bainite (B_L) with *HV*0.1-3620–3860 MPa microhardness and martensite (M) (4120–4410 MPa). Volume fraction of upper bainite (B_U) with 3030–3210 MPa microhardness does not exceed 10 %. Separate areas of pearlite (2570–2710) and residual austenite (2700 MPa) of total volume not more than 2 % were also found.

Special electron-microscopy examinations of fine structure of the specimens were carried out for confirmation of changes in substructural level in HAZ metal, which take place at low-temperature tempering. The specimens that were continuously cooled on welding thermal cycle and specimens with four hours holding at 100 °C were selected for this. Table 1 shows generalized results of the investigations.

It is determined that tempering of HAZ metal during its cooling provoked changes in the substructural level, and they lied in the following. Dislocation density ρ in the elements of structure decreased approximately 1.5

Table 1. Parameters of fine structure, calculation values of local deformation and second type stresses (HAZ, steel 65G)

Cooling conditions	Structure elements	Lath width h, μm	Dislocation density ρ, cm^{-2}	Local deformation ε_{loc}, %	Second type stresses τ_{loc}, MPa
Continuous cooling on WTC	B_U	0.2–0.5	$4–5\cdot10^{10}$	2.8–9.0	739–924
	B_L	0.4–0.7	$6–7\cdot10^{10}$	8.4–17.5	1109–1294
	M	0.8–1.2	$7–8\cdot10^{10}$	17.5–33.6	1294–1474
On WTC from 100 °C, tempering 4 h, further in air	B_U	0.2–0.5	$3–3.5\cdot10^{10}$	2.1–6.3	554–646
	B_L	0.4–0.7	$4–4.5\cdot10^{10}$	5.6–11.25	739–830
	M	0.8–1.2	$5–6\cdot10^{10}$	14.0–25.0	924–1109

times (Table 1). At that width of the laths h of structural constituents does not change. Besides, together with simple quenching martensite (Figure 4, *b*) there were local areas of tempering martensite (Figure 4, *d*) in the metal. A calculation method, using substructure parameters, determined local deformations and stresses of II type. It is determined that local deformations and stresses in the volume of upper bainite laths showed 1.4 times reduction, that for lower bainite made 1.5 times and 1.3–1.4 times for martensite. Obviously, that these changes in the substructural level are the main factor of increase of indices of ductile and impact toughness properties of HAZ metal. These positive changes should, as a consequence, promote increase of its brittle fracture resistance.

Work [7] notes that the critical coefficient of stress intensity K_{1c} for HAZ metal of steels 65G and KS2 at cooling rate $w_{6/5}$ = 6 °C/s and hydrogen content $[H]_{dif}$ = = 0.5 ml/100 g makes 11 and 17.5 MPa √m, respectively, that is 6.5 and 3 times lower than the indices for steels in their initial state. These indices of metal brittle fracture resistance were received in testing of the specimens in course of not more than 0.5 h after their hydrogenation. K_{1c} indices increased 1.9 and 1.5 times (Figure 5), respectively, in testing of the similar specimens after aging (recovery) during 72 h at room temperature. Obviously, it is related with diffusion processes and partial removal of hydrogen from quenched metal.

K_{1c} index during two hours tempering at 100 °C for KS2 steel HAZ increased 1.8 times (from 17.5 to 32 MPa√m). More significant 4 times rise of brittle fracture resistance (from 11 to 45 MPa√m) under these conditions of cooling is noted for steel 65G HAZ metal. In our opinion, these changes can be explained by effect of two factors. First of all, it is complete removal of diffusion hydrogen from metal, that can be experimentally proved using «pencil tests» with model specimens after their fracture. Secondly, as it was determined earlier, due to relaxation of stresses of II type in the quenched metal structure. Mutual effect

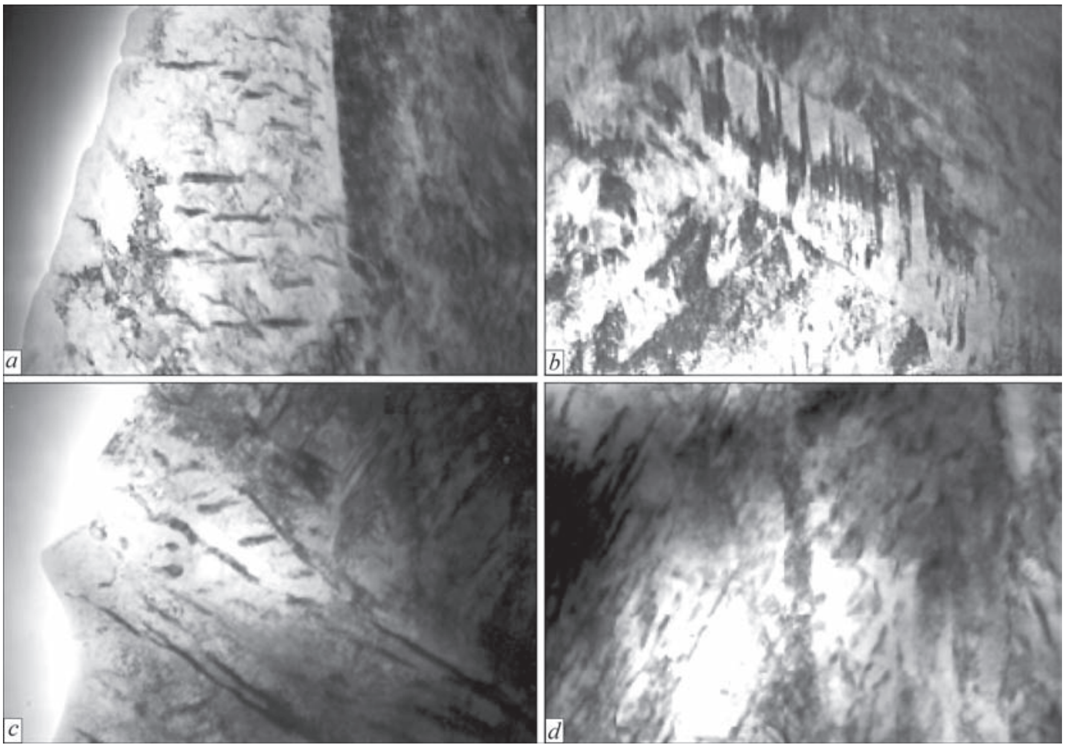

Figure 4. Elements of fine structure of HAZ metal of steel 65G at continuous cooling on welding thermal cycle (*a*, *b*) and with tempering at 100 °C during four hours (*c*, *d*) (×30000): *a*, *b* — B_L; *c*, *d* — M

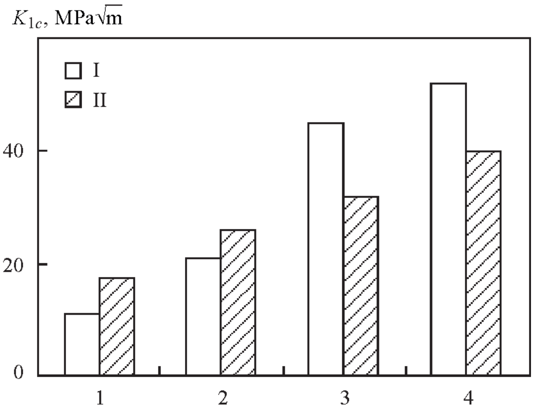

Figure 5. Brittle fracture resistance of HAZ metal of steels 65G (I) and KS2 (II) ($[H]_{dif}$ = 0.5 ml/100 g) depending on cooling conditions (1–4 — numbers of experiments in accordance to Table 2)

of these two processes were more obvious in testing of HAZ metal with bainite-martensite structure. Increase of holding time in the furnace at 100 °C up to four hours promotes approximately 10 % (Figure 5) additional rise of crack resistance in HAZ metal of studied steels.

Structure of fractures was examined on HAZ metal of steel KS2. Table 2 shows generalized results of fracture examination in a zone of main crack propagation, and Figure 6 represents typical fracture types. It is determined that nature of the fracture will dramatically change at holding of HAZ metal at 100 °C during 2–4 h. There is no brittle intercrystalline fracture (BCF) on the fracture surface, portion of brittle intraglanular fracture (BGF) increases up to 80–90 %, length of secondary cracks (L_{sec}) significantly reduces (from 120 to 30 μm), and portion of tough constituent in the fracture rises up to 10–20 %.

Carried investigations showed that application of low-temperature tempering (at 100 °C) during 2–4 h in process of cooling of railway wheels after their surfacing allows dramatic up to 4.5 times increase of resistance of quenched HAZ metal to brittle fracture, approximating it to high-strength steel indices in initial state. Taking into account that the wheel tread in process of continuous surfacing is heated to 260 °C, these technological operations can be fulfilled without additional energy expenses at delayed cooling of railway wheels in the heat chambers. In order to keep metal temperature at 100 °C level during long time it is necessary to use heat-insulating materials in a heat chamber structure, being additionally applied to the wheels, or use heating to 50 °C in the general heat chambers, where wheel pairs are set after surfacing. It is experimentally determined that time of metal holding in the temperature range 130–90 °C rises up to four hours under such conditions of wheel cooling after surfacing.

Enhancement of resistance of HAZ metal of high-strength carbon steels to brittle fracture has positive effect on change of welded joint fatigue resistance (Figure 7). Fatigue limit of the joints increases 1.5–2.0 times applying tempering at 100 °C in course of four hours in process of cooling. Moreover, a tendency of change of welded joint fatigue limit differs depending on type

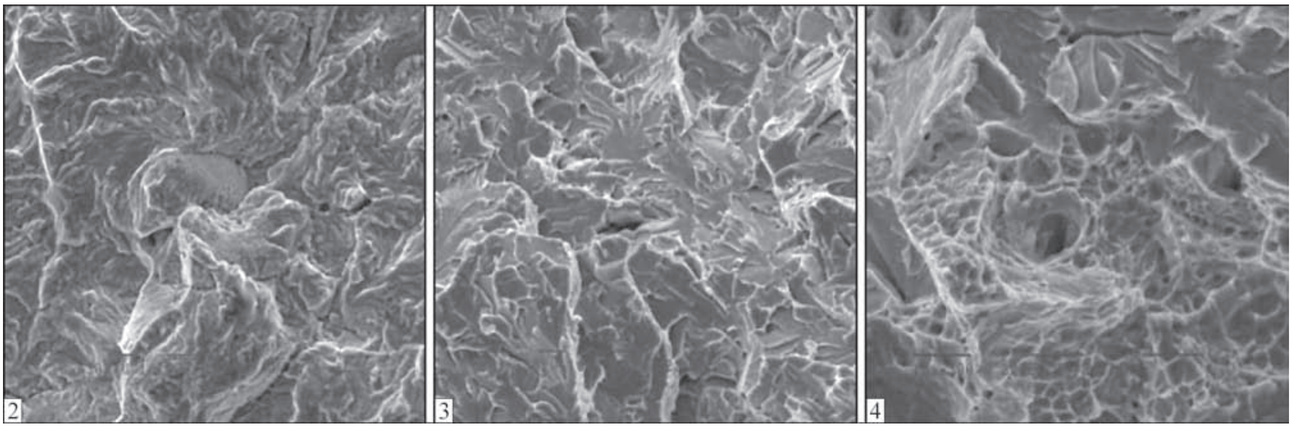

Figure 6. Fracture surface of HAZ metal of steel KS2 in zone of main crack propagation depending on cooling conditions (2, 3 — ×1010; 4 — ×2020); 2–4 — numbers of tests (see Table 2)

Table 2. Fracture nature in zone of main crack propagation (HAZ, steel KS2)

Number of experiment	Cooling conditions	K_{1c}, MPa√m	Fracture characteristics		
			BGF, %/ L_{sec}, μm	BCF, %/ L_{sec}, μm	Tough, %
1	Continuous cooling on WTC	17.5	70/120	30/120	–
2	Continuous cooling on WTC, holding 72 h	26	95/30	–	5
3	On WTC to 100 °C, tempering 2 h, further in air	32	90/30	–	10
4	On WTC to 100 °C, tempering 4 h, further in air	40	80/30	–	20

of investigated steel. Apparently, it is related with different structural state of quenched HAZ metal. Thus, cooling rate in HAZ of the joints with indicated welding conditions made $w_{6/5}$ = 13–15 °C/s. Bainite-martensite structure (relationship of structural constituents approximately 70/30) is formed in HAZ metal of steel KS2 at this cooling rate, and that in steel 65G is mainly martensite (volume fraction of bainite not more than 3 %) [7]. Therefore, fatigue limit of the joints of steel KS2 during two hours holding at 100 °C in comparison with four hours makes already 92 % of maximum value, 110 and 120 MPa, respectively, and only 67 % (80 MPa) for steel 65G. This indicates that two hours holding at 100 °C in formation of mainly martensite metal structure is not enough for relaxation of II type stresses. Realization of microplastic changes in such metal requires more time. It should also be noted that the same results [13] were obtained at H.V. Karpenko Phyciso-Mechanical Institute of the NAS of Ukraine (Lviv) during independent investigations on evaluation of changes at propagation of fatigue cracks in HAZ metal depending on cooling conditions.

In the conclusion it should be noted that carried investigations allowed improving surfacing technology in order to increase reliability of repaired wheels in railway transport operation. A novelty of the technology is proved by the patent of Ukraine [14]. It in addition to new requirements on cooling conditions of railway wheels after surfacing includes the requirements to value of preheating temperature depending on carbon content in wheel steel and level of welding consumables alloying.

Conclusions

1. It is determined that application of low-temperature tempering at 100 °C during two-four hours in process of cooling of welded joints of high-strength steels with 0.55–0.65 % carbon content promotes rise of indices of ductility properties of quenched HAZ metal up to 1.7 times and that of impact toughness up to 3 times at keeping its high strength level. Enhancement of HAZ metal ductility takes place due to positive changes in the substructural level. At that there is 1.5 times reduction of dislocation density in the lath volume of bainite and martensite as well as level of II type stresses in the structure of quenched HAZ metal.

2. Application of low-temperature tempering at 100 °C in surfacing of railway wheels in process of their cooling allows significant (up to 4.5 times) rise of resistance of quenched HAZ metal to brittle fracture, approximating its to as-delivered high-strength steel indices. Fatigue fracture resistance of welded joints rises up to two times at that.

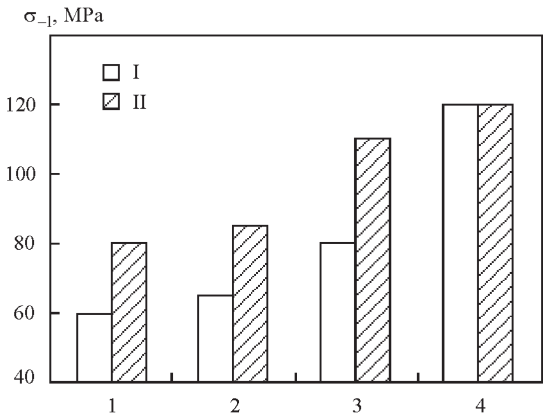

Figure 7. Effect of cooling conditions on fatigue strength of welded joints of steel 65G (1) and KS2 (II); 1–4 — numbers of experiments in accordance with Table 2

1. (1972) *New methods for assessment of resistance of metals to brittle fracture*. Ed. by Yu.N. Robotnova. Moscow: Mir.
2. Makarov, E.L. (1981) *Cold cracks in welding of alloy steels*. Moscow: Mashinostroenie.
3. Kasatkin, O.G., Mikhoduj, L.I., Kasatkin, S.B. et al. (1995) Resistance to delayed and brittle fracture of HAZ metal of 14Kh2GMR type high-strength steels. *Avtomatich. Svarka*, **2**, 7–10.
4. Skulsky, V.Yu. (2009) Peculiarities of kinetics of delayed fracture of welded joints of hardening steels. *The Paton Welding J*., **7**, 12–17.
5. Efimenko, M.G., Radzivilova, N.O. (2003) *Physical metallurgy and heat treatment of welded joints*. Kharkiv: NTU KhPI.
6. Anokhov, A.E., Korolkov, P.M. (2006) *Welding and heat treatment in power engineering*. Kyiv: Ekotekhnologiya.
7. Gajvoronsky, A.A., Poznyakov, V.D., Markashova, L.I. et al. (2016) Brittle fracture resistance of HAZ metal in arc-welded joints of high-strength steels with carbon content of 0.55–0.65 %. *The Paton Welding J*., **9**, 2–8.
8. Babachenko, A.I., Litvinenko, P.L., Knysh, A.V. et al. (2011) Improvement of chemical composition of steel for railway wheels providing of their resistance invrease to defect formation on roll surface. In: *Fundamental and applied problems of ferrous metallurgy: Transact., Dnepropetrovsk*, 226–233.
9. Matveev, V.V. (2007) *Restoration of railway wheels using surfacing*. Kiev: PWI.
10. Gajvoronsky, O.A. (2016) Conditions of quality assurance of railway wheels restored by surfacing. Science and progress of transport. *Visnyk DNUZT im. V. Lazaryana*, 5(**65**), 136–151.
11. Markashova, L.I., Poznyakov, V.D., Berdnikova, E.N. et al. (2014) Effect of structural factors on mechanical properties and crack resistance of welded joints of metals, alloys and composite materials. *The Paton Welding J*., **6/7**, 22–28.
12. (1990) *Strength of welded joints under alternating loadings*. Ed. by V.I. Trufyakov, Kiev: Naukova Dumka.
13. Haivoronskyi, O.A., Poznyakov, V.D., Markashova, L.I. et al. (2016) Structure and mechanical properties of the heat-affected zone of restored railway wheels. *Mater. Sci*., 51(**4**), 563–569.
14. Gajvoronsky, O.A., Poznyakov, V.D., Klapatyuk, A.V. (2014) *Method of restoration of high-carbon steel products*. Pat. 107301, Ukraine. Int. Cl. B23P 6/00.

Received 12.04.2017

doi.org/10.15407/tpwj2017.08.04

INVESTIGATION OF PROCESS OF FORMATION OF STRUCTURE AND PROPERTIES IN MAGNETRON NANOLAYER FeAl-COATINGS

Yu.S. BORISOV[1], **M.V. KUZNETSOV**[1], **B.T. TKACHENKO**[1], **A.V. VOLOS**[1], **V.G. ZADOYA**[1],
L.M. KAPITANCHUK[1], **A.I. GUDYMENKO**[2] and **V.F. GORBAN**[3]
[1]E.O. Paton Electric Welding Institute, NASU
11 Kazimir Malevich Str., 03680, Kiev, Ukraine. E-mail: office@paton.kiev.ua
[2]V.E. Lashkaryov Institute of Semiconductor Physics, NASU
45 Nauki Ave., 03028, Kiev, Ukraine. E-mail: mickle@semicond.kiev.ua
[3]I.M. Frantsevich Institute of Problems of Materials Science, NASU
3 Akad. Krzhizhanovsky, 03142, Kiev, Ukraine. E-mail: post@ipms.kiev.ua

The work is dedicated to investigation of process of formation of Fe-Al coating with regulated composition on substrates of 08Kh18N10T steel at mutual magnetron sputtering of composite Al + Fe target with heated above the Curie point (768 °C) insert of St.3 and aluminum target. Application of a system of cyclic substrate movement in the active zones of magnetron operation allowed forming a nanolayer structure of coatings with Al — 1.3–1.9 and Fe — 1.6 nm nanolayer thickness. The coatings were investigated using Auger spectrometry, X-ray diffraction and microindentation. It is determined that 3 μm FeAl-coatings containing 39.6 and 54.6 at.% of Al are an ordered B2 — FeAl phase consisting of 0.135–0.173 and 0.293–0.335 μm size grains, formed from nanocrystallites of 7 and 22 nm, respectively. 17 Ref., 4 Tables, 6 Figures.

Keywords: *magnetron sputtering, nanolayer structure, FeAl-coatings, regulated layer*

One of the tasks of surface engineering at modern stage of equipment development is a development of new coatings and technologies for their deposition ensuring protection of the parts and assemblies of equipment under conditions of elevating operating temperatures and mechanical loads, effect of aggressive media. In this connection, FeAl intermetallics, being characterized with high heat-resistance at 600–1000 °C, corrosion resistance in aggressive sulfur-containing media and wear, represent themselves a perspective material for development of new protective coatings. The technologies of coating deposition based on iron aluminides using plasma, electric arc, high-velocity plasma arc, detonation spraying [1, 2], allow forming FeAl-coatings of 100–300 μm thickness. Another field for producing FeAl-coatings is the vacuum methods, namely cathode sputtering [3], ion spraying [4], electron-beam evaporation [5], pulse laser deposition [6–8] and magnetron sputtering [9–12]. The magnetron sputtering method has gained the widest distribution.

Magnetron sputtering is widely used due to its capability to provide formation of coatings with thicknesses from nanometers to microns by means of condensation from neutral or ionized atoms at relatively low temperature with dense nanocrystalline structure [9]. Deposition of such coatings can be made using different technological schemes. There is an experience of application of magnetron sputtering system with the targets from FeAl alloy, produced by melting and casting in vacuum of pure Fe and Al metals [10]. The cheaper variant is receiving of FeAl coatings of various compositions by sputtering of compound target consisting of aluminum base and changeable iron disks of different diameters [11]. It should be noted that low iron deposition velocity was obtained at that. It is related with the fact that a magnetic flow, formed with magnetron magnetic system, is shunted by magnetic insert. This provokes distortion of distribution of transverse component of magnetic induction and its maximum displacement out of the insert limits. A variant of simultaneous sputtering of two targets from aluminum and iron is characterized by higher possibility for producing FeAl-coating of any composition. The multi-layer Al (4nm)/Fe(3.7 nm) magnetic films of 140 nm thickness were deposited on rotating silicon substrates with iron deposition velocity 9 nm/min [12]. The X-ray diffraction investigations showed that these films have bad crystallinity and do not contain reliable characteristics of ordered B2 phase.

Present work is dedicated to investigation of process of FeAl-coating formation with regulated composition at simultaneous magnetron sputtering of two targets.

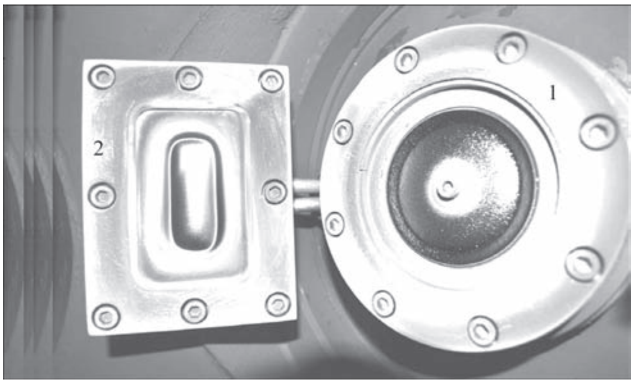

Figure 1. Positioning of magnetrons in vacuum chamber of VU-1BS unit: 1 — magnetron 1 with compound target Al + Fe (d = 88 mm); 2 — magnetron 2 with aluminum target of 80×50 mm size

Figure 2. Compound target Al + Fe with insert (d = 64 mm, δ = = 3 mm) of steel St.3

Procedures of experiment and investigations. FeAl-coatings were deposited using modernized vacuum unit VU-1BS, which was equipped with direct current magnetron sputtering module consisting of two magnetrons (Figure 1). A compound Al + Fe target consisting of water-cooled aluminum part (d = = 88 mm, δ = 10 mm) and heat-insulated from it insert (d = 65 mm, δ = 3 mm) of low-carbon steel St.3 was installed on the magnetron 1. A magnetron discharge was excited at P_1 = 850 W, with cold insert at the periphery of aluminum part of the target, as well as maximum value of transverse constituent of magnetic induction $B_{\text{tr.max}}$ of magnetron 1 magnetic field. It provides fast heating of the insert via its end to the temperature above the Curie point (768 °C for iron) that provokes simultaneous displacement of $B_{\text{tr.max}}$ and discharge on insert surface. As a result the insert became a source of constant deposition velocity of iron atoms (Figure 2). Magnetron 2 with aluminum target of 80×50 mm size was used for receiving regulated aluminum constituent of FeAl-coating at power variation in P_2 = 0.35–1.4 kW range.

An auxiliary magnetic system of the same structure as a magnetron magnetic system was installed in front of magnetron 1 at 100 mm distance from it. Its magnetic field formed a consistent configuration with a field of magnetron 1 magnetic system (central and external poles of the auxiliary magnetic system have intensity of magnetization opposite in relation to poles of the magnetron magnetic system). This provided increase of current density of ion cleaning of substrate and enhancement of effect of plasma ions of magnetron discharge on a surface of growing coating that promoted rise of coating adhesion.

Glass substrates (65×30×4 mm) were used for initial experiments on investigation of the process of formation of FeAl-coating layers at different power of magnetrons. Choice of the glass substrates was stipulated by the necessity to perform accurate measurements of coating thickness with the help of profilograph — profilometer of AI Model 252 type. Specimens of steel 08Kh18N10T of 65×30×0.5 mm size were used as base substrates.

The substrate was moved in sequence in relation to the magnetrons crossing the zones of Al and Fe atom flows, being formed on sputtered targets *1* and *2* with 0.3 m/s velocity. The distance between the targets and substrate made 55 and 70 mm, respectively (Figure 3). Deposition of FeAl-coating took place in cyclic mode with formation of single layers at substrate passing through the zones of Al and Fe atom flows. Thickness of the single layers depends on speed of rotation of holder with fastened substrate and deposition velocity of coating components (Fe and Al).

Thickness of the single layers makes 1.6 nm for Fe and 1.3–1.9 nm for Al under conditions of 0.3 m/s speed of substrate linear movement and deposition velocities v_{Fe} = 24nm/min and v_{Al} = 20–29 nm/min.

The next procedure was developed for calculation of content of aluminum in FeAl-coatings using the deposition velocities of iron and aluminum.

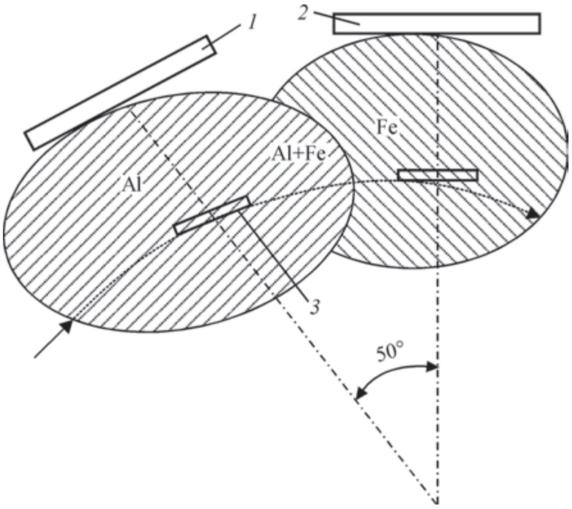

Figure 3. Scheme of deposition of magnetron FeAl-coating: *1* — aluminum target; *2* — St.3 heated insert of compound Al + Fe target; *3* — position of substrate relative to magnetrons in rotation with 15 rpm rate

Content of aluminum in FeAl-coatings can be presented by expression:

$$C_{\mathrm{Al}} = \frac{Q_{\mathrm{Al}}}{Q_{\mathrm{Al}} + Q_{\mathrm{Fe}}} \cdot 100\,\%,\ \text{wt.\%}, \qquad (1)$$

where Q_{Al} and Q_{Fe} are the weight of aluminum and iron composing the coating, which are simultaneously deposited using magnetrons *2* and *1*, respectively.

Values of Q_{Al} and Q_{Fe} are equal:

$$Q_{\mathrm{Al}} = \rho_{\mathrm{Al}} v_{\mathrm{Al}} ts;\ Q_{\mathrm{Fe}} = \rho_{\mathrm{Fe}} v_{\mathrm{Fe}} ts, \qquad (2)$$

where ρ_{Al} and ρ_{Fe} are the densities of deposited aluminum and iron, g/cm^3; v_{Al} and v_{Fe} are the deposition velocities of aluminum and iron, nm/min; t is the time of deposition, min; s is the area of specimen surface, cm^2.

Following the expressions (1) and (2)

$$C_{\mathrm{Al}} = \frac{\rho_{\mathrm{Al}} v_{\mathrm{Al}} ts}{\rho_{\mathrm{Al}} v_{\mathrm{Al}} ts + \rho_{\mathrm{Fe}} v_{\mathrm{Fe}} ts} \cdot 100\,\% = \frac{\rho_{\mathrm{Al}} v_{\mathrm{Al}}}{\rho_{\mathrm{Al}} v_{\mathrm{Aa}} + \rho_{\mathrm{Fe}} v_{\mathrm{Fe}}} \cdot 100\,\%,\ \text{wt.\%}. \qquad (3)$$

Transformation of expression (3) generates formula (4) for calculation of deposition velocity of aluminum v_{Al} on set values of aluminum content C_{Al} and deposition velocity of iron v_{Fe}.

$$v_{\mathrm{Al}} = \frac{C_{\mathrm{Al}} v_{\mathrm{Fe}} \rho_{\mathrm{Fe}}}{(100\,\% - C_{\mathrm{Al}})\rho_{\mathrm{Al}}},\ \text{nm / min}. \qquad (4)$$

The next experiments were carried out for determination of ρ_{Al} and ρ_{Fe} of received coatings. Coatings of iron and aluminum were deposited on glass substrates at magnetron power $P_1 = 830$ W and $P_2 = 1350$ W. The profilograph-profilometer was used for determination of thickness of these coatings and calculation of deposition velocities $v_{\mathrm{Fe}} = 24$ nm/min and $v_{\mathrm{Al}} = 38$ nm/min. At these values of P_1 and P_2 and corresponding velocities v_{Fe}, v_{Al} the coatings of iron and aluminum were deposited on substrate of steel 08Kh18N10T of 18 cm^2 area without its ion cleaning. The substrates were weighed on VLR-200 scales before and after coating deposition (weighing error ±0.00012 g) and weight increment of Fe and Al was determined: $\Delta_{\mathrm{Fe}} = 0.01145$ g, 0.01205 g ($\delta = 1000$ nm), $\Delta_{\mathrm{Al}} = 0.0118$ g, 0.0121 g ($\delta = 2440$ nm). Coating densities, i.e. $\rho_{\mathrm{Fe}} = 6.97$ g/cm^3 and $\rho_{\mathrm{Al}} = 2.7$ g/cm^3 were calculated on average values of received values $\Delta_{\mathrm{Fe}} = 0.01205$ and $\Delta_{\mathrm{Al}} = 0.01195$ g.

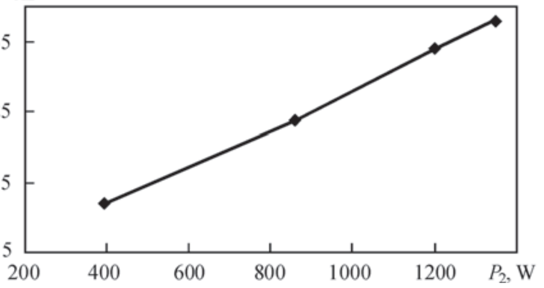

Figure 4. Dependence of aluminum deposition velocity on magnetron *2* power

Density of iron coatings has appeared to be less than standard volumetric density 7.86 per 0.89 g/cm^3 (11.3 %). This difference can depend on series of factors effecting vacuum coating formation. Thus, work [9] indicates that density of vacuum films is related with such characteristics as porosity, size of block structure, microstresses and can differ from volumetric density by up to 13 % value. Angle of incidence of sputtered atoms flow can vary in deposition of the coatings on moving substrate that can also influence the density of formed coating [14].

The following is received using $\rho_{\mathrm{Fe}} = 6.97$ g/cm^3, $\rho_{\mathrm{Al}} = 2.7$ g/cm^3 and constant value $v_{\mathrm{Fe}} = 24$ nm/min applied in all experiments.

$$v_{\mathrm{Al}} = \frac{61{,}92 C_{\mathrm{Al}}}{100\,\% - C_{\mathrm{Al}}},\ \text{nm / min}. \qquad (5)$$

The dependence v_{Al} (P_2) was received (Figure 4) for determination of magnetron *2* power on calculated v_{Al}.

The process of coating formation on surface of steel 08Kh18N10T substrates consisted of the following stages:

- before positioning in a vacuum chamber the substrate was cleaned in ultrasonic pool in acetone medium, and then in spirit;
- heating of substrate in vacuum chamber at $p = 5.0 \cdot 10^{-4}$ Pa, $T = 150$ °C, $t = 20$ min;
- ion cleaning of fixed substrate surface located between magnetron *1* and auxiliary magnetic system at pressure in the chamber $p_{\mathrm{Ar}} = 1.3$ Pa, $U = 1100$ V, current density $j = 3.5$ mA/cm^2, $t = 20$ min;
- excitation of magnetron discharge at a periphery of aluminum part of compound target of magnetron *1*, heating of steel insert to temperature above the Curie point with further movement of discharge over insert surface at $p_{\mathrm{Ar}} = 1.3$ Pa, $P = 0.9$ kW, $t = 5$–6 min;
- deposition of Fe sublayer on moving substrate at $p_{\mathrm{Ar}} = 0.3$ Pa, $P_1 = 830$ W, $U_{\mathrm{disp}} = -1100$ V, $T = 300$ ºC, $t = 10$ min, $\delta = 240$ nm;
- deposition of FeAl-coating on moving substrate at magnetron *2* switching-on at $p_{\mathrm{Ar}} = 0.3$ Pa, $U_{\mathrm{disp}} = 0$ V, $T = 150$–200 ºC, $\delta = 3$ μm.

Investigation of content and structure of coatings was carried out using Auger spectrometer JUMP 9500 F. X-ray phase analysis of the coatings was performed with the help of diffractometer Philips X'Pert – MRD based on Cu-K_α1 radiation (wave length $\lambda = 0.15405980$ nm). Diffraction spectra were recorded by scanning in step-by-step mode, scanning step made 0.025 °, time of setting in a point made 1 s. Qualitative phase composition was determined using ICDD, data base PDF-2 Release 2012.

Determination of mechanical characteristics of coatings and friction coefficient was performed employing micronanoindentor «Micron-Gamma» and friction machine «Micron-tribo» [15, 16]. Values of hardness and elasticity modulus in indentation were calculated automatically on ISO 14577-1:2002 standard [17].

Table 1. Parameters of deposition of FeAl-coating on moving substrates of steel 08Kh18N10T and measured values of aluminum content in coatings

Specimen	P_1, W	V_{Fe}, nm/min	P_2, W	v_{Al}, nm/min	C_{Al}^{calc},		C_{Al}^{meas},		Deviation value $C_{Al}^{meas} - C_{Al}^{calc}$	
					wt.%	at.%	wt.%	at.%	wt.%	at.%
Fe40Al	830	24	1040	29	32	49.6	36.74	54.6	4.74	5.0
Fe55Al	830	24	700	19.6	24	38.6	24.05	39.6	0.05	1.0

Results and their discussion. Investigations of process of FeAl-coating production was based on 47.0–52.7 at.% of Al concentration range, where B2–FeAl phase is formed, and coatings with 37–49 at.% of Al concentration, which have experimentally determined high heat-resistance at 600 – 1000 °C, including in aggressive gaseous media [10].

The values of aluminum concentration in the coating C_{Al}^{calc} = 36 and 24 wt.%, formula (5) and dependence $\nu_{Al}(P_2)$ were used for determination of aluminum deposition velocities and corresponding magnetron *2* powers, and production of coatings of 3 μm thickness on specimens *1* and *2*. During coating deposition the substrate successively passes through flows of aluminum and iron sputtered atoms (see Figure 3). Close location of the targets (distance between their centers 105 mm) and fast movement of the substrate promoted active mixing of deposited on its surface atoms of Al and Fe and generation at each turn FeAl nanolayers, which form FeAl-coating along its whole thickness (Table 1). It should be noted that Fe/Al-coating of alternating nanolayers of iron and aluminum can be obtained at lager distance between the magnetrons of indicated system design and installation of a screen between them. Table 1 shows that calculated concentration of aluminum differs from measured by 1–5 at.% of Al that can be explained by the following reasons:

- during selection of C_{Al} and ν_{Al} calculation procedure it was assumed that FeAl-coating consists only of iron and aluminum. However, JUMP 9500 F spectrometer registered in the vacuum coating specimens the constant additives (oxygen, carbon) reaching in sum up to 5 wt.%;
- another reason lies in quick change of erosion zone of aluminum target in process of coating formation. Carried investigations on sputtering of 4 mm thick target at P_2 = 1000 W showed that typical V-shaped erosion zone with *3* mm depth limit is formed in it at electric energy consumption 4.7 kW·h. It is determined that proportionality of $v_{Al}(P_2)$ dependence was preserved at electric energy consumption up to 2 kW·h. However, deepening of the erosion zone promotes gradual decrease of deposition velocity at constant discharge power. Thus, at zone depth 3 mm the measured deposition velocity of aluminum was less than calculated on curve $v_{Al}(P_2)$ (Figure 3) by 20.3 %. Decrease of aluminum deposition velocity is obviously related with formation of V-shaped surface of erosion zone that provokes increase of intensity of ionizing collisions in plasma of magnetron discharge, constriction of plasma area, growth of density of positive ions of Ar^+ as well as Al^+ ions of sputtered aluminum. As a result portion of ionized atoms of aluminum rises in the general flow of ions bombarding the target. They come back to the target, deposit on the surface of erosion zone and do not reach the substrate.

Figure 5 shows radiographs of coatings on specimens *1* and *2*.

The radiographs contain clear reflections (110) and (200) of FeAl phase, that indicate that the structure of coating on the specimens is the ordered B2–FeAl phase with body-centered crystalline lattice having the following parameters: Fe55Al — a_1 = 0.29097 nm, Fe40Al — a_2 = 0.29090 nm. The Scherrer formula was used for calculation of the dimension of coherent scattering region (CSR) for crystals forming the coating: Fe55Al — D_1 = 7 nm, Fe40Al — D_2 = 22 nm.

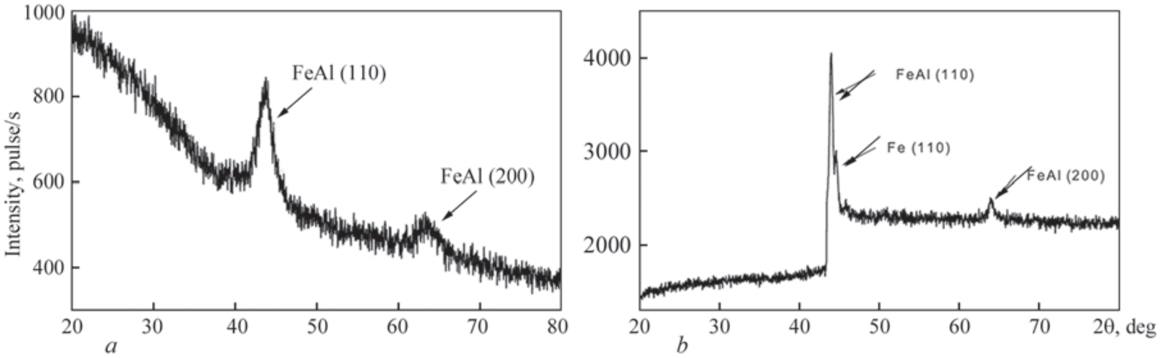

Figure 5. Radiographs of FeAl-coating with different Al content: *a* — FeAl-coating with 54.6 at.% of Al (specimen Fe55Al); *b* — Fe-Al-coating with 39.6 at.% of Al (specimen Fe40Al)

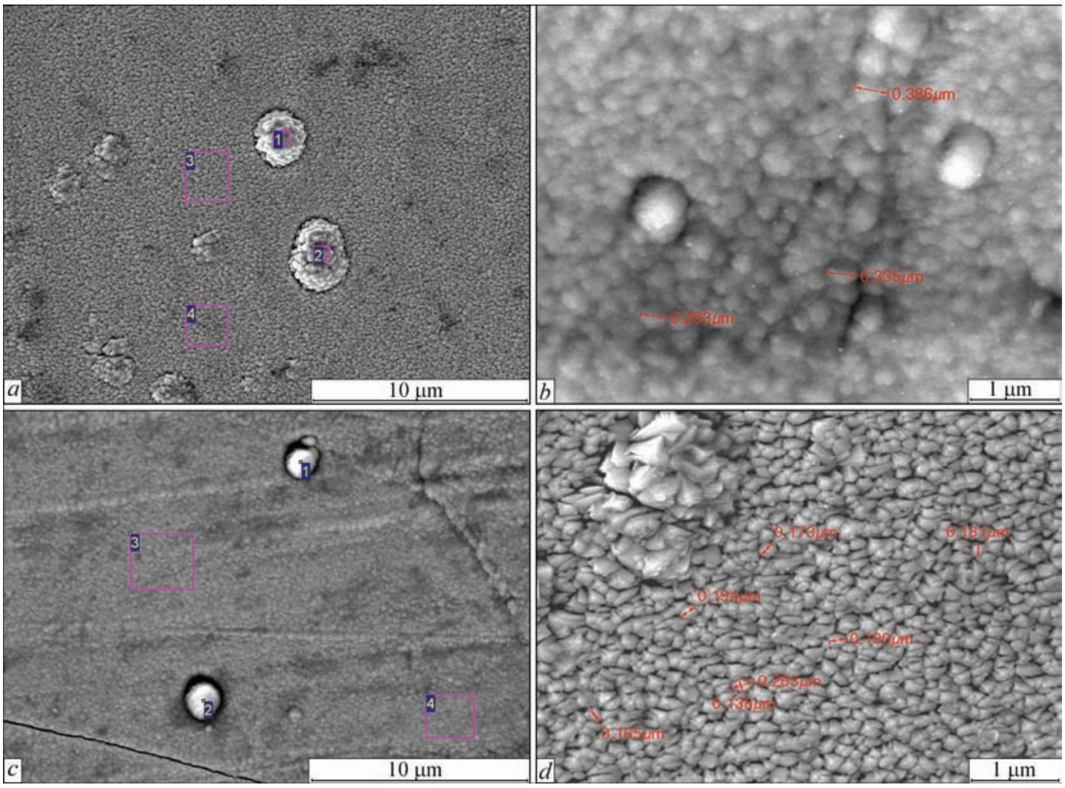

Figure 6. Microstructure of surface of magnetron FeAl-coatings of 3 mm thickness deposited on substrates of steel 08Kh18N10T with different Al content: *a*, *b* — Fe55Al; *c*, *d* — Fe40Al

Reflection Fe (110) is also registered on Fe40Al radiograph. It can be related with the fact that content of aluminum in this coating is less than the lower boundary of content range, in which B2–FeAl phase is formed in 47–52.7 at.% of Al.

Figure 6 and Tables 2 and 3 present the data and photos from scanning electron microscope (SEM) of the structure of coating surface on Fe55Al and Fe40Al specimens and compositions of these coatings at different areas of the specimens.

Analysis of received data shows formation of dense, pore-free crystalline structure of the coatings on the surfaces of both specimens of steel 08Kh18N10T. Grain sizes in these coatings depend on Al content and make 0.293–0.335 μm (Fe55Al) at 54.6 at.% of Al and 0.131–0.173 μm at 3.9 at.% of Al (Fe40Al).

Small content of chromium (C_{Cr} = 0.42–0.78 at.%) is found in the content of specimen coatings that can be related with insignificant sputtering of the frame made of steel 08Kh19N10T, with the help of which aluminum target is fixed to magnetron *2*.

Surfaces of FeAl-coating specimens include separate convex polycrystalline formations of 1.7 and 3.2 μm diameter, in which content of aluminum comparing with nearby area is more by 1.2–1.8 at.%.

It is apparently related with appearance of microarcs in the process of aluminum target sputtering that has stipulated generation of micron particles of aluminum, which were deposited on the surface of formed coating and was overgrown by this coating.

Mechanical characteristics of the coatings, determined by microindentation method, are presented in Table 4.

The results of measurement of mechanical properties of magnetron FeAl-coatings, made with the help of micronanoindentor «Micron-Gamma» showed that the value of their contact elasticity modulus rises with decrease of Al content and makes 204 GPa for Fe40Al coating in comparison with 188 GPa in Fe55Al coating. Values of hardness in both coatings differ insignificantly (14 and 13 GPa), but data of specified hardness, effecting coating wear resistance, are higher in Fe55Al coating (0.074 in contrast to 0.064 in Fe40Al coating).

Value of coefficient of dry friction in «coating–diamond indentor pair» with rounded radius

Table 2. Composition of FeAl-coating in different areas of Fe-55Al (at.%)

Spectrum	Al	Cr	Fe
1	54.72	0.42	44.87
2	55.37	0.78	43.85
3	54.01	0.78	45.21
4	54.14	0.77	45.08

Table 3. Composition of FeAl-coating in different areas of Fe-40Al (at.%)

Spectrum	Al	Cr	Fe
1	40.42	0.47	59.11
2	39.39	0.83	59.79
3	38.52	1.60	59.88
4	39.92	0.64	59.45

Table 4. Mechanical characteristics of FeAl-coating on substrates of steel 08Kh18N10T

Specimen	Hardness *H*, GPa	Contact elasticity modulus E^*, GPa	Specified hardness H/E^*, relative units	Friction coefficient *f* at loading on indentor, g		
				225	375	525
Fe55Al	14	188	0.074	0.11	0.12	0.12
Fe40Al	13	204	0.064	0.11	0.12	0.12

0.12 mmwith slip velocity 12 mm/s at 225–525 g loading made 0.11–0.12.

Conclusions

1. Microcrystalline FeAl-coatings of 3 μm thickness, formed from nanocrystallines with the size depending on coating composition and equal 7 nm in Fe54.6Al at.% coating and 22 nm in Fe39.6Al at.% coating, were received using the method of simultaneous direct current magnetron sputtering of compound target Al + Fe on moving substrates of steel 08Kh18N10T. The target consists of heated above the Curie point (768 °C) insert of steel St.3 (d_{insert} = = $0.75d_{\text{Al parts of target}}$) and aluminum target.

2. Developed system of magnetron sputtering of FeAl-coatings with the device for cyclic movement of substrate in zones of Al and Fe atom flows, being generated on used Al and Al + Fe targets, allows forming the nanolayer structure of FeAl-coating with thickness of single layers of 1.6 nm and iron 1.3–1.9 nm aluminum. This provides formation of FeAl phase without additional heat treatment by annealing at 600–1000 °C.

3. Calculation-experimental procedure was developed for regulation of aluminum content in FeAl-coating in 40–55 at.% of Al range by means of variation of power of magnetron discharge at aluminum target with constant power of sputtering of St.3 insert of compound target.

4. The results of examination of FeAl-coatings using Auger spectrometry and X-ray diffraction methods show that they are ordered B2–FeAl phase at content of 39.6 and 54.6 at. % of Al in them, grain size of which rises with increase of Al content in FeAl-coating, making 0.135-0.173 μm in the case of Fe40Al coating and 0.293–0.335 μm for Fe55Al coating.

5. Values of contact modulus of elasticity of FeAl-coatings, determined with microindentation method, depend on Al content and make 188 GPa in Fe55Al coating and 204 GPa in Fe40Al coating. Hardness values of received FeAl-coatings are 13–14 GPa, that of specified hardness make 0.064–0.074. Coefficient of dry friction of FeAl-coating in pair with diamond indentor made 0.1–0.12.

6. Application of developed method of magnetron deposition of FeAl-coating allows forming heat-resistant coatings with increased resistance to oxidation and scaling as well as multilayer soft magnetic FeAl-coatings with high intensity of magnetization in weak magnetic fields, which can be used in magnetic protection devices.

1. Cinca, N., Guilemany, J.M. (2012) Thermal spraying of transition metal aluminides: An overview. *Intermetallics*, **24**, 60–72.
2. Cinca, N., Guilemany, J.M. (2013) An overview of intermetallics research and application: Status of thermal spray coatings. *J. of Materials Research and Technology*, 2(**1**), 1–11.
3. Paldey, S., Deevi, S.C. (2003) Cathodic arc deposited FeAl coatings: Properties and oxidation characteristics. *Mater. Sci & Engin.*, **A355**, 208–215.
4. Arcon, I., Mozetic, M., Zalar, A. et al. (2003) EXAFS study of ion beam mixed Fe/Al multilayers. *Nuclear Instruments and Methods in Physics Research*, **B199**, 222–226.
5. Brajpuriya, R., Tripathi, S., Chaudhari, S.M. (2005) Thermally induced changes in magnetic, transport and electronic properties Fe/Al multilayers. *Solid State Communications*, **134**, 479–484.
6. Levin, A.A., Meyer, D.C., Paufler, P. (2000) Structural modifications of laser deposited Fe–Al multilayers due to thermal treatment. *J. of Alloys and Compounds*, 297, 59–67.
7. Levin, A.A., Meyer, D.C., Gorbunov, A. et al. (2001) Comparative study of interfaces of Fe–Al multilayers prepared by direct and crossed-beam pulsed laser deposition. *Thin Solid Films*, 47–56.
8. Levin, A.A., Meyer, D.C., Paufler, P. et al. (2001) Thermally stimulated solid state reactions in Fe-Al multilayers prepared by pulsed laser deposition. *J. of Alloys and Compounds*, **320**, 114–125.
9. Paldey, S., Deevi, S.C. (2003) Single layer and multilayer wear resistant coatings of (Ti, Al)N: A review. *Mater. Sci. & Engin.*, **A342**, 58–79.
10. Zhenya, L., Wei, G. (1998) Oxidation behaviour of FeAl intermetallic coatings produced by magnetron sputter deposition. *Scripta Materialia*, **39**, 1497–1502.
11. Sanchette, F., Billard, A. (2001) Main feature of magnetron sputtered aluminium-transition metal alloy coatings. *Surf. and Coat. Technol.*, **142–144**, 218–224.
12. Cherif, S.M., Boussigne, K., Boussigne, Y. (2007) Growth and magnetic study of sputtered Fe/Al multilayers. *Mater. Sci. & Engin.*, **138**, 16–21.
13. Marchenko, I.G., Marchenko, I.I., Neklyudov, I.M. (2004) Computer modeling of vacuum deposition of niobium films. *Visnyk Kharkivskogo Universytetu*, **628**, 93–98.
14. Tomal, V.S., Kasinsky, N.K., Ivanov, I.V. (2013) Repeatability of properties of optical vacuum coatings. *Materialy. Tekhnologii. Instrumenty*, **18**, 75–77.
15. Ignatovich, S.R., Zakiev, I.M. (2009) Universal micro-nanoindentometer Mikron-gamma. *Zavod. Laboratoriya*, 77(**1**), 61–67.
16. Gorban, V.F., Zakiev, I.M., Sarzhan, G.F. (2016) Comparative characteristics of friction of high entropic mononitride coatings. *Trenie i Iznos*, 37(**3**), 340–344.
17. Gorban, V.F., Mameka, N.A., Pechkovsky, E.P. et al. (2006) Indentification of structural state of materials by method of automatic indentation. In: *Kharkovskaya Nanotekhnologicheskaya Assambleya: Transact.*, **1**, 52–55.

Received 13.06.2017

doi.org/10.15407/tpwj2017.08.05

DEVELOPMENT OF TECHNOLOGY AND EQUIPMENT FOR REDUCTION OF RESIDUAL STRESSES AND STRAIGHTENING IN WELDED STRUCTURES APPLYING ELECTRODYNAMIC TREATMENT

L.M. LOBANOV and **N.A. PASHCHIN**
E.O. Paton Electric Welding Institute, NASU
11 Kazimir Malevich Str., 03680, Kiev, Ukraine. E-mail: office@paton.kiev.ua

A new technological process of postweld treatment of welded joints is presented, namely the electrodynamic treatment by pulses of high-density electric current. The carried out complex of experimental investigations on specimens of aluminium alloy AMg6 at different parameters of electric current pulses and inductance of power source showed that electrodynamic treatment influences the structure of treated metal and allows a significant reduction in residual stresses in welded joints, increasing their resistance to fatigue and brittle fracture, and also eliminating buckling deformations of thin-walled structural elements. The developed technologies and equipment provided the possibility of performing electrodynamic treatment of welded joints of ship-building structures and repair welds of intermediate casing of aircraft engine, which facilitated their increased operational reliability and service life. 8 Ref., 18 Figures.

Keywords: *electrodynamic treatment, aluminium alloy, welded joint, residual stresses, current pulse, mathematical modeling, current density, plastic deformation*

The high requirements specified to welded structures of advanced engineering cause the necessity in the development of technologies for their postweld treatment. Prospective are the processes based on the effect of electrodynamic forces on conductive materials during passing of electric current pulses (ECP), realized in a new technological process: electrodynamic treatment (EDT). Using the energy of ECP and the electrodynamic forces initiated by it, which affect the treated elements of metal structures at EDT, it is possible to influence the stressed state of metal materials. The effectiveness of EDT is determined by interaction of two components: the electric pulse one, realized during passing of ECP of density j over the workpiece treated and the dynamic one preset by the amplitude-frequency characteristic of waves of dynamic stresses. The increase in the service characteristics of welded joints as a result of EDT is predetermined by the complex influence of the following factors. Thus, in the treatment zone under the action of electrodynamic forces, the stress waves are formed in the weld metal, which, interacting with residual welding stresses, initiate a reduction in the latter. As a result of EDT, zones with refined grains are formed in the metal, the evolution of their structure being determined by plastic deformation under conditions of the realization of the electroplastic effect (EPE) based on the electron-dislocation interaction [1], initiated by passing of ECP at $j \geq 1$ kA/mm^2.

Taking into account the specifics of EDT of welded structures, which is distinguished by a large length of welded joints and their different spatial positions, the possibility of mobile positioning of equipment is provided to realize electrodynamic effects. The features of welded joints determine the requirements for equipment designed to perform EDT, which include:

- equipment for EDT should consist of separate components, such as ECP source (ECPS), an executive electrode device (ED) designed to realize the electrodynamic effects on the welded joint treated, as well as communication means between ECPS and ED;
- ergonomic characteristics of ED and the means of its communication with ECPS should provide convenience in realizing electrodynamic effects with a preset duration, amplitude and periodicity in manual mode and as a part of automated welding complexes.

Based on the analysis of pulse current generating devices, it was found that the most suitable for the formation of ECP in the composition of ECPS is the use of capacitor systems which have a number of advantages over other devices, such as the possibility of accumulating a controllable level of electric charge energy, creation of different shapes and duration of ECP, as well as simplicity in recovery of electrical parameters of the discharge mode. The most effective way to regulate the ECP discharge parameters is the control of voltage of the capacitive energy storage (CES) before passing a discharge pulse. Another regulating parameter of the device is the pulse duration. For this, it is necessary to provide the possibility of changing the electrical parameters of the discharge circuit of the capacitor. The control device, by means of which the pulse duration is regulated, is the inductance coil (IC) included into the ED. Moreover, the coil inductance can vary within a wide range. Coming from the requirements specified to ED, it is recommended to use IC in the form of a plane inductor. Thus, the control parameters of the ECPS are the charge voltage of CES, which can be varied over a wide range by means of a control system, and also the inductance of the discharge circuit L. At present, single- and double-circuit ECPS are designed, the appearance of which is shown in Figure 1.

A feature of the single-circuit ECPS (Figure 1, *a*) is the direct passing of ECP of the main circuit through the material treated, and that of the double-circuit is the separate passing of current through the circuits, providing the electric pulsed and dynamic components of the electrodynamic effect. The advantages of a single-circuit ECPS is the simplicity of its design, relatively small weight (up to 20 kg) and dimensions (450×450×250 mm), positioning mobility and simplicity in operation. Its drawbacks include lack of possibility in regulating the frequency characteristics of the electric pulsed and dynamic components of the electrodynamic effect. The advantage of the double-circuit ECPS (Figure 1, *b*) is the equipment regulation of frequency characteristics of the components of the electrodynamic effect, and the drawbacks are a relatively large weight (up to 120 kg) and dimensions (1500×450×450 mm).

For realization of EDT using a single-circuit ECPS, a specialized ED was developed, the design of which provides passing of ECP through a one-channel circuit.

Figure 1. Appearance of single-circuit (*a*) and double-circuit (*b*) sources of pulsed electric current for EDT

The schematic diagram and appearance of one-channel ED are shown in Figure 2. The ED provides electric contact between the discharge circuit and the metal treated through one channel, through which the ECP is passed into the latter. ED provides the realization of a dynamic and electric pulse effect

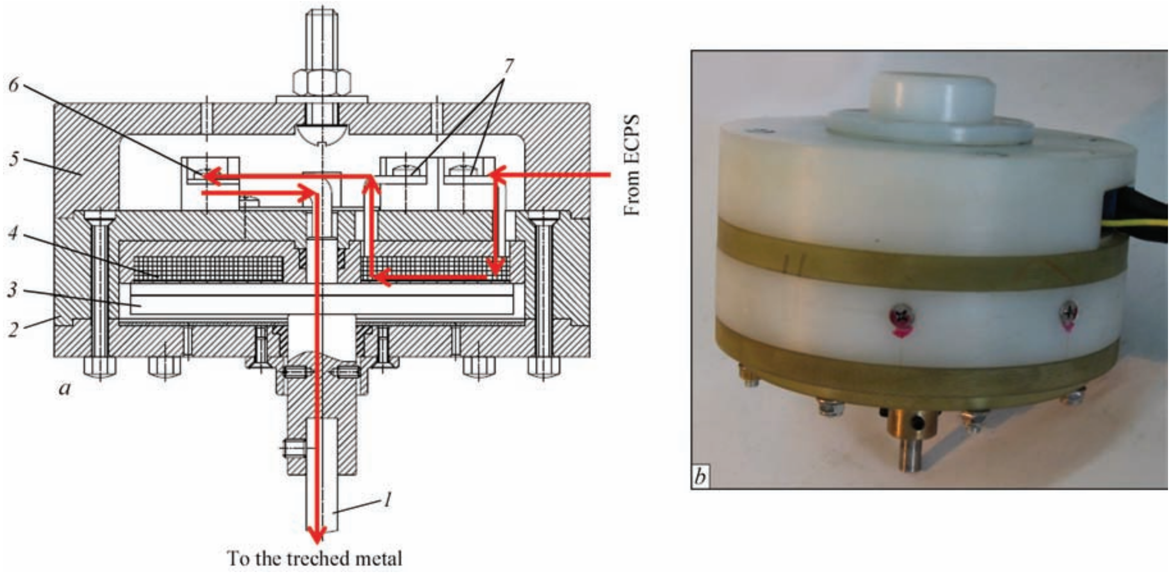

Figure 2. Electrode device for EDT: *a* — schematic diagram (*1* — electrode; *2* — body; *3* — disc; *4* — inductance coil; *5* — cover; *6*, *7* — terminals); *b* — appearance

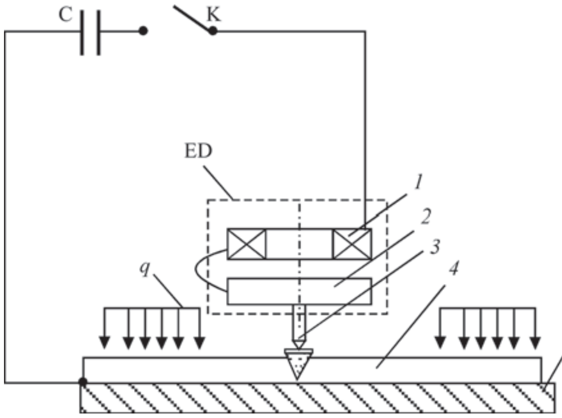

Figure 3. Circuit of EDT of welded joints (C — energy storage capacitor; K — power key; *q* — fixing load); *1* — inductor; *2* — disc; *3* — electrode; *4* — specimen; *5* — assembly plate

on the metal. The direction of ECP passing through the ED circuits from the ECPS to the metal treated is shown by the arrows in Figure 2, *a*. The operating element of ED is the electrode *1*, fixed in the body *2*. The working surface of the electrode contacts the metal treated. The body *2*, rigidly connected to the disc *3*, together with the electrode *1* is included into an impact mechanism (IM), which has the ability to move in a vertical direction. The disc *3* is coupled with the inductance coil *4*. At the top the connection terminals are closed by cover *5*, designed also for positioning the ED in the process of treatment. To connect the ED to the ECPS, the terminals *6* and *7* are located on the top of body *2*. The terminal *6* provides passing of the ECP through the electrode, and *7* — through the inductance coil.

For a double-circuit ECPS, a two-channel ED circuit was developed. The design of the two-channel ED is similar to that shown in Figure 2, but the ECP passing through the electrode *1* and the inductance coil *4* occurs separately.

During operation the ED rests against the metal by the electrode end face and is set perpendicularly to surface treated. Passing of the ECP through the inductance coil in a disc excites a magnetic field, initiating eddy currents in the disc. The interaction of induced currents *I* with the exciting magnetic field leads to the appearance of an electrodynamic force *P*. The scheme of EDT of welded joints by one-channel circuit is shown in Figure 3.

The oscillograms of the dynamic pressure *P* and the pulsed current *I*, passing through the plate of the aluminium AMg6 alloy of thickness $\delta = 4.0$ mm with a charge voltage $U_{ch} = 500$ V and an CES capacitance C = 6600 μF by one-channel circuit are shown in Figure 4. As to its duration the effect of ECP-I on the treatment zone at one-channel circuit exceeds the period of action of force *P* (Figure 4), which is preset by the configuration of the discharge circuit. The features of the two-channel circuit guarantee an independent change in the duration of ECP-I and *P* in the range from 0 to 0.68 s, determined by the parameters of the electric circuit of the separate discharge circuits. This allows presetting different ratios of the amplitude-frequency characteristics of the current and dynamic effects on the metal treated.

To position the ED relative to the surface being treated and to provide a reliable electric contact of the working part of elelectrode in the EDT zone, a specialized manual tool was designed (Figure 5). The design elements of the tool are the base *2*, on which the fixed handle *1* and the fixing plate of ED *3* are located. The

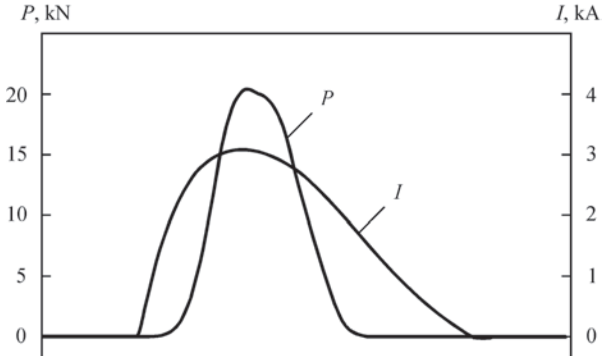

Figure 4. Oscillograms of dynamic pressure *P* and pulsed current *I* passing through the metal treated at a charge voltage $U_{ch} = 500$ V, CES C = 5140 μF, and the inductance *L* = 5.0 μH in the one-channel circuit of discharge circuit

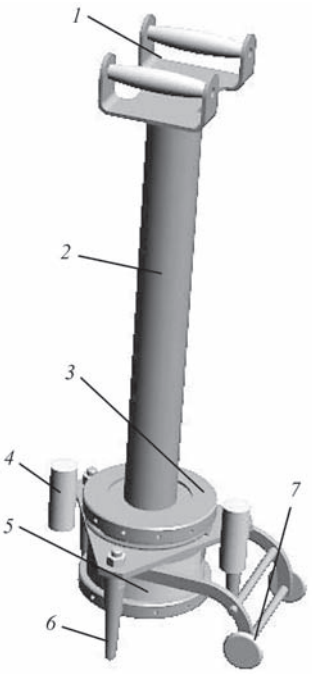

Figure 5. Appearance of manual tool for EDT (*1* — fixed handle; *2* — base; *3* — mechanism for ED fastening; *4* — backlight; *5* — ED; *6* — support; *7* — transport trolley

handle is designed for moving the tool by the operator, and on the plate the backlight of EDT zone — *4*, ED — *5* and two supports *6* are fixed, which together with the electrode of ED provide a three-point resting of the tool against the metal surface treated.

The tool is equipped with a transport trolley *7*, designed for working and sliding movements of ED along the welded joint.

It should be noted that the experimental evaluation of the effectiveness of EDT for the purpose of determining the optimal mode of treatment of welded joints is a rather laborious task, which is associated with the consideration of a large number of parameters of EDT mode, the types of welded joints and mechanical characteristics of metals and alloys subjected to treatment.

In order to optimize the process of selecting the EDT mode, a mathematical model of non-stationary electrophysical [2] and dynamic [3] processes was developed, which determine the mechanism for EDT of welded joints. On the basis of the model, a selection of the mode characteristics is performed to provide the ECP parameters sufficient for effective control of residual stressed state of metal structures.

The adequacy and reliability of mathematical modeling of non-stationary processes in the metal treated is confirmed by experimental investigations carried out on the developed ECPS (Figure 1, *a*) [2].

The description of electrophysical processes at EDT was carried out on the basis of reduction of Maxwell equations to the system of integral equations for current density and electrodynamic forces in the contact zone of the electrode *3* and the specimen *4* (Figure 3).

Figure 6 shows the distribution of lines of equal value of density of ECP j across the thickness *z* of the plate of AMg6 alloy at $L = 5$ μH, C = 5140 μF, $U_{ch} = 500$ V at the moment of time $t = 0.71$ ms (Figure 4), which corresponds to the maximum value of ECP in the discharge circuit. It can be seen that the presented mode provides the values of current density $j \geq 1$ kA/mm^2, which can initiate EPE in the AMg6 alloy treated.

The realization of EPE is confirmed by the data in Figure 7, which shows the distribution of lines of equal value of radial plastic deformations ε_r of tension across the thickness z of the plate of AMg6 alloy at EDT mode, similar to that used in Figure 6. The presented distribution ε_r is caused by the action of electrodynamic forces arising when ECP passes in the zone of electrode contact with the metal treated. It can be seen that electrodynamic forces provide electroplastic deformation of the AMg6 alloy in the treatment zone. It should be noted that the interaction of deformations initiated by EDT with residual welding plastic compression deformations affects the reduction of stress-strain state of welded structures.

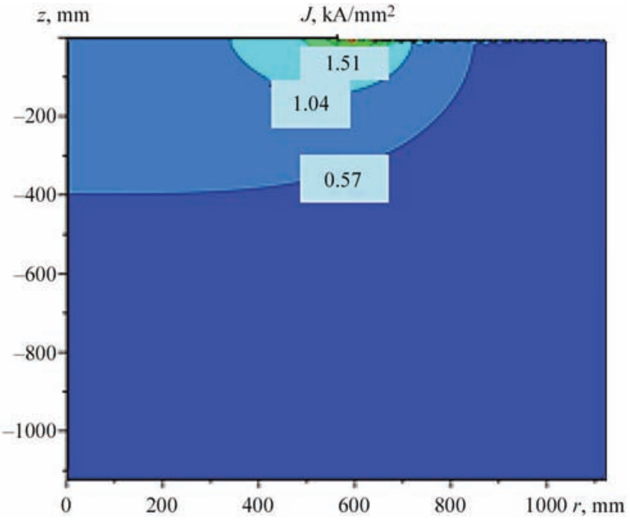

Figure 6. Distribution of lines of equal value of ECP density *j* on width r and thickness *z* of plate of AMg6 alloy (explanations see in the text)

The influence of dynamic component of the electrodynamic effect was determined on the basis of the theory of plastic flow based on the Prandtl–Reiss relations. Figure 8 shows the residual distribution of effective plastic deformations ε^p_{eff} in the cross-section of unstressed plate of the AMg6 alloy of thickness $\delta =$ $= 4$ mm after a single ECP at EDT mode at $L = 5$ μH, C = 5140 μF and $U_{ch} = 200...800$ V. It can be seen that at $U_{ch} = 200$ V, the zone of plastic deformation with a range of values $\varepsilon^p_{eff} = 0.04...0.07$ is localized near the surface of the plate (Figure 8, *a*). When U_{ch} is increased to 500 V, the zone of plastic deformation with a range of values $\varepsilon^p_{eff} = 0.03–0.17$ is propagated almost to the central zone of the plate section (Figure 8, *b*). The increase in the value of U_{ch} to 800 V (Figure 8, *c*) initiates the propagation of the zone of

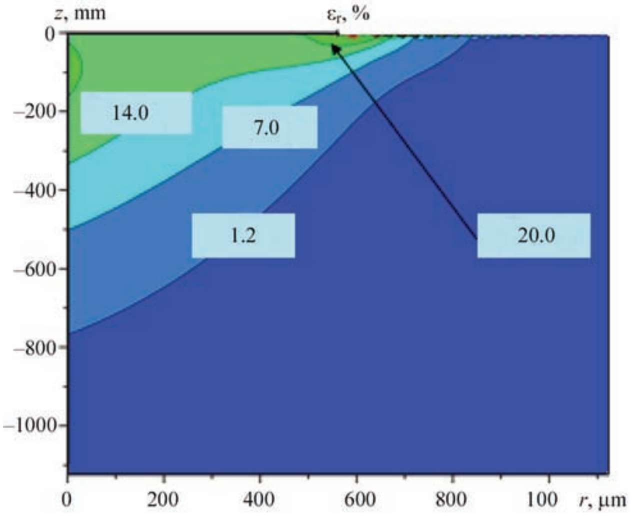

Figure 7. Distribution of lines of equal value of radial plastic deformations ε_r along width *r* and thickness *z* of the plate made of AMg6 alloy (explanations see in the text)

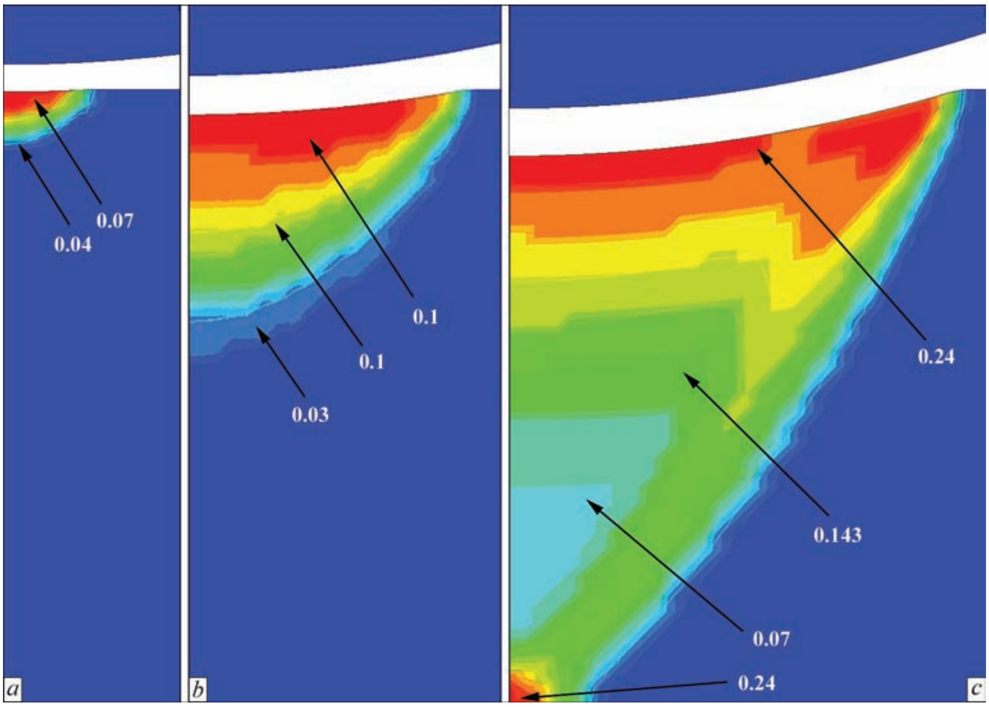

Figure 8. Residual distribution of effective plastic deformations ε^{p}_{eff} in the cross-section of the plate of AMg6 alloy of thickness $\delta = 4$ mm at $L = 5$ μH, C = 5140 μF: *a* — $U_{ch} = 200$; *b* — 500; *c* — 800 V

plastic deformation in the range $\varepsilon^{p}_{eff} = 0.07–0.24$ over the entire section of the plate.

Moreover, in contrast to the data in Figure 8, *a*, *b*, the reflection of the deformation wave from the back surface of the plate is observed, confirmed by the equality of values $\varepsilon^{p}_{eff} = 0.24$ on both sides of the specimen, and also by their decrease in its center.

The data in Figure 8, *b* confirm the distribution of radial component of the residual stresses σ_r after a single ECP at $U_{ch} = 500$ V, shown in Figure 9. It can be seen that the propagation of ε^{p}_{eff}, determined by the dynamic effect, initiates the fields of residual compressive stresses, respectively, $\sigma_r = 73.8$ and –40.5 MPa in the treatment zone and at moving off from it. The superposition σ_r of compression with residual welding tensile stresses can substantially reduce the peak values of stresses in the welded joint.

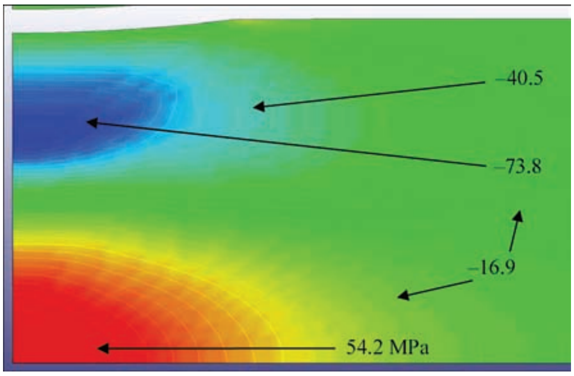

Figure 9. Distribution of radial component of residual stresses σ_r after single ECP at $U_{ch} = 500$ V

In general, analyzing the data in Figures 6–9, it can be concluded that electrodynamic and dynamic effects, considered separately within the frames of mathematical modeling of EDT process, have a significant effect on the stress-strain state of the AMg6 alloy, which is confirmed by experimental investigations, the results of which are presented below.

The investigations of evolution of structure of the structural materials caused as a result of EDT allowed determining the features of electrodynamic effect on the mechanism of plastic deformation of metals and alloys as a result of treatment. The features of the structure and relief of fractograms were investigated using the scanning electron microscopy.

The effect of EDT on the features of fracture of plane specimens of the AMg6 aluminium alloy treated applying EDT according to one-channel circuit was investigated. The treatment was carried out applying single ECP of the base metal and welded joints with the dimensions of working part being 150×30×4 mm at EDT mode at the charge voltage U_{ch} of 500 V and at CES of 6600 μF.

To determine the electrodynamic effect on change in the structure of the material, the topography of macrorelief of the fracture of specimens of the AMg6 alloy at the abovementioned mode was compared in the initial state (Figure 10, *a*) and after EDT (Figure 10, *b*) , from which it is seen that the fractures have an advantageous fibrous structure with tearing crusts formed on the mechanism of mixed fracture [4].

To study the relief of fractures after the electrodynamic effect, the specimens with a one-sided treatment of the material were used. In Figure 10, *b* (zone A), it can be seen that the fracture on the treated side has a more developed fibrous structure as compared with the initial state (Figure 10, *a*). The depth of distribution of the fibers reaches 3.0 mm across the thickness of the specimen, which is confirmed by the data in Figure 8, *b* and characterizes the electrodynamic effects as a volumetric one. At the profound study of the fracture relief after EDT (zone B in Figure 10, *b*), the developed groups of plane sliding lines were observed, the orientation of which coincided with the treated surface of the specimen. Moreover, the sliding has the signs of a rotational mechanism [5], which indicates an intensive running of the process of volumetric plastic flow of the material under the conditions of electrodynamic effects.

The increment of density of the treated areas of the polycrystalline structure leads to deformation hardening, which was confirmed by the results of measurements of hardness HV, which were carried out in the device M-400 of the company LECO at the load value of 0.1 N. The values of *HV* for non-treated material (Figure 10, *a*, zone B) were 824 MPa. The maximum values of *HV* 1290–1310 MPa were observed near the surface treated (Figure 10, *b*, zone A), where there was a rotational sliding along with the plane one. Thus, the hardness of the AMg6 alloy after EDT is by 35–40 % increased as compared to an untreated one.

The metallographic examinations of the AMg6 alloy in the initial state and after EDT at the mode described above, showed that the structure of the metal being not treated by the current, consists of dispersed precipitations of the β-phase of Al_3Mg_2 in the enclosure of magnesium silicide MgSi, where the β-phase has a large area and a lighter shade surrounded by dark lines and spot inclusions of magnesium silicide. At the same time, the treated structure is characterized by a refined grain, which increases the resistance of metal to delayed fracture.

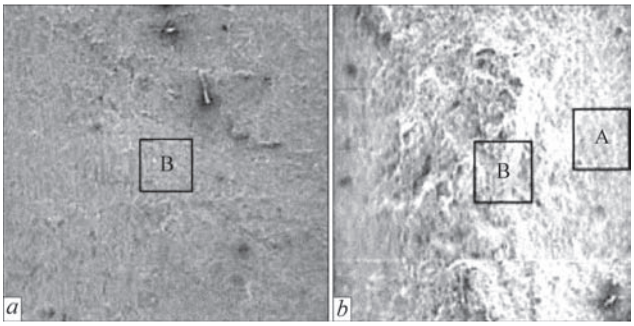

Figure 10. Fractograms (×33) of fractures of the AMg6 alloy, obtained during fracture of specimens without EDT (*a*) and after EDT (*b*) (zone A is the treated area near the metal surface, B is the middle fracture area)

Using the method of «thin foils» [6], the fine initial structure of the AMg6 alloy, as well as its evolution as a result of dynamic and electrodynamic effects according to the one-channel circuit of EDT were investigated. The dynamic effect was realized by eliminating the passing of ECP through the metal treated. The treatment was carried out applying single ECP of specimens of 150×30×4 mm at EDT mode at the charge voltage of U_{ch} = 350 V and CES of C = 6600 μF.

As was shown by the results of investigations (Figure 11), the grains of the untreated metal are characterized by a substructure (Figure 11, *a*) with the dimensions d_s within the ranges of ~1.8–5.0 μm, as well as a uniform distribution of density of dislocation structure between the volume ρ_v and the grain boundary ρ_b. The value of ρ_v reaches $6\cdot10^9$ cm^{-2}, and ρ_b — $8\cdot10^9$ cm^{-2}, which leads to the absence of density gradient of dislocations $\Delta\rho_v$ in the grain volume.

In the metal, after the dynamic effect (Figure 11, *b*), both the dispersed $d_s \sim 1.1$ μm as well as large-sized substructure of $d_s \sim 3.2$ μm is observed without formation of distinct subboundaries. An increase in the density level of dislocations at the grain boundaries ρ_b

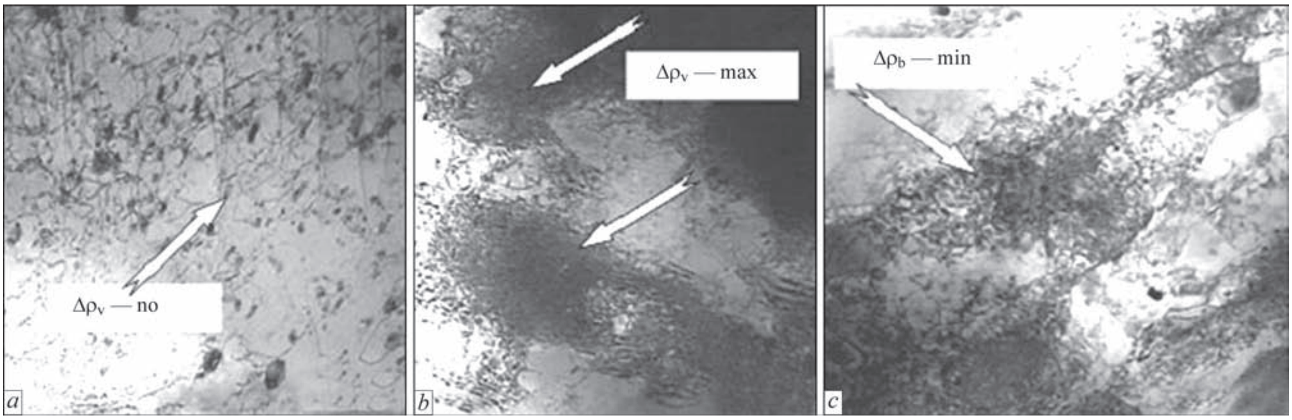

Figure 11. Thin structure of the AMg6 alloy: *a* — in the initial state (×25000); *b* — $\Delta\rho_v$ is the maximum after dynamic effect, ×22000); *c* — $\Delta\rho_b$ is the minimal after electrodynamic effect ($\Delta\rho_b$, $\Delta\rho_v$ are the gradients of the density of dislocations at the boundaries and in the volume of grains)

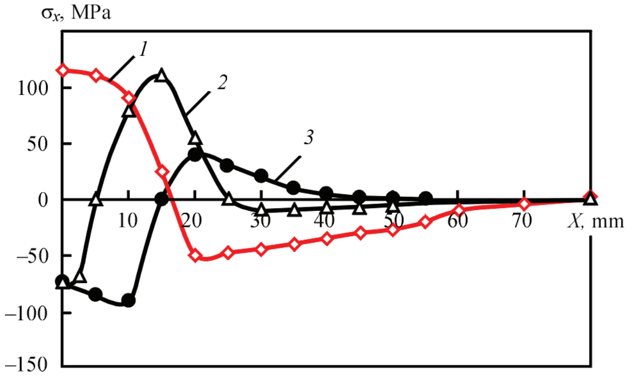

Figure 12. Distribution of longitudinal residual stresses σ_x in the cross-section of welded plate of the AMg6 alloy (curve *1* — initial σ_x; *2* — σ_x after EDT along the weld axis; *3* — σ_x after EDT of the weld axis and base metal at the distance of 10 mm from the weld axis)

was registered, as well as the gradient $\Delta\rho_v$ between the inner volume of grains ρ_v ~$6\cdot10^8$–$4\cdot10^9$ cm^{-2} and ρ_b ~ $2\cdot10^{11}$ cm^{-2}.

After electrodynamic effect, the metal is characterized by the formation of substructures (Figure 11, *c*) with distinct boundaries d_s = 0.8–2.5 μm. Moreover, the density of dislocations ρ_b decreases as compared to the metal after the dynamic effect, as well as their uniform distribution over the entire volume of the metal (without sharp gradients along the grain boundaries $\Delta\rho_b$) between the internal volume of grains ρ_v ~ 2–$3\cdot10^{10}$ cm^{-2} and near grain boundaries ρ_b ~ 6–$8\cdot10^{10}$ cm^{-2}.

The formation of this structure confirms the proposed concept based on the theory of electron-dislocation interaction [1] about the contribution of ECP to relaxation of residual stresses.

To evaluate the electrodynamic effect on residual stresses, the treatment of the specimens of butt welded joints of the AMg6 alloy with dimensions of 400×300×4 mm with the central weld was performed. The weld was produced by automatic butt TIG welding at the mode with arc voltage U_a = 18 V, welding current I_a = 250 A and speed v_w = 3.1 mm/s. Two-sided treatment of welded plates was carried out by ECP at EDT mode at the voltage U_{ch} = 550 V and the capacitance CES C = 6600 μF. The distance between the zones of electrodynamic effects did not exceed 5 mm.

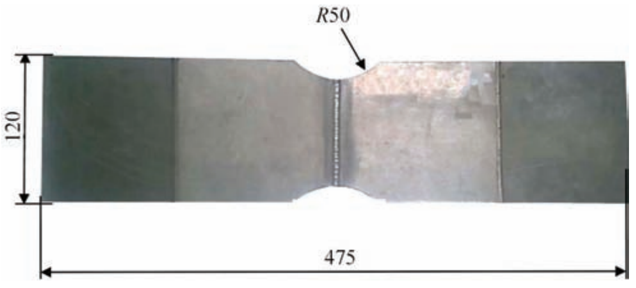

Figure 13. Specimen of welded joint of AMg6 alloy for fatigue tests

The measurements of residual stresses were carried out using the method of electron speckle-interferometry [7].

The distribution of longitudinal (along the weld line) residual stresses σ_x before and after EDT is shown in Figure 12. It can be seen that the initial maximum of σ_x did not exceed 120 MPa (curve *1*). After EDT of the welded joint along the weld axis, the initial values of σ_x in the weld changed from 120 to –75 MPa, and the maximum residual tensile stresses up to 115 MPa were formed on the untreated part of the plate (curve *2*). After EDT of the weld and base metal at a distance of 10 mm from the weld axis (curve *3*), the values of σ_x are changed from 90 to –100 MPa, which is comparable with EDT of the weld center. By analyzing the data in Figure 12, it can be seen that the maximum efficiency of the electrodynamic effect is achieved at EDT along the weld axis and the base metal near the fusion line (curve *3*).

The influence of EDT on the fatigue resistance of welded joint specimens of the AMg6 alloy with the thickness δ = 2 mm (Figure 13) made by automatic TIG welding (Ar) at the values of arc voltage, welding current and speed of the process, respectively U_w = 20 V, I_w = 170 A, v_w = 5.5 mm/s. Two-sided treatment of specimens along the weld line of 90 mm length was carried out by the series of ECP at the mode of two-channel EDT with the charge voltage U_{ch} = 430 V and the capacitance CES of C = 5580 μF. The distance between the zones of applying electrodynamic effects was 5 mm, the width of the working part of specimen was 265 mm.

The fatigue tests on the cantilever bending of specimens of welded joints were carried out in the machine UPM-02 at the symmetrical cycle at the amplitude of cycle stresses in the range of $2\sigma_a$ = 80–160 MPa.

From Figure 14, which presents the results of fatigue tests in the coordinates $2\sigma_a$ – N of specimens in the initial state and after EDT, it can be seen, that the cyclic life N of specimens of welded joints in the in-

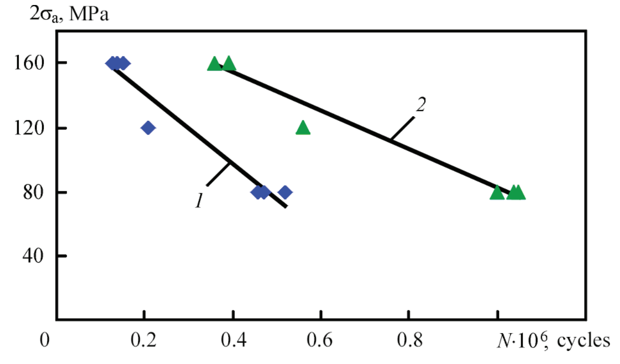

Figure 14. Results of fatigue tests for specimens of welded joints of AMg6 alloy (see Figure 9) in the coordinates $2\sigma_a$ N (curve *1* — initial state; *2* — after EDT)

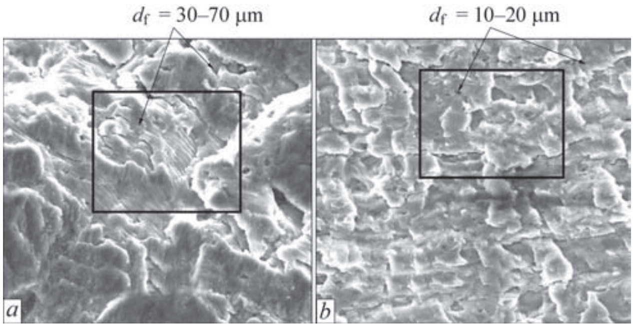

Figure 15. Fracture surfaces of specimens of AMg6 alloy after a low-cycle loading (×810): *a* — initial specimen; *b* — after EDT

vestigated range of $2\sigma_a$ up to three times increases as a result of treatment. At the same time, the fracture of both the initial specimens as well as the treated ones occurs along the fusion line.

On the basis of the results presented above, it can be concluded that EDT has a positive effect on increasing service life of welded joints of the AMg6 alloy, which is to a significant extent determined by decrease in the level of residual welding stresses.

The fractographic analysis of the microrelief of the surface of the initial and treated specimens fractured as a result of cyclic loading at $2\sigma_a$ = 160 MPa (Figure 15) showed that the treated metal is characterized by dispersion of structural elements, such as 3 times refinement of the size of d_f facets (Figure 15, *b*) as compared to the initial state before EDT (Figure 15, *a*). This confirms the positive influence of electrodynamic effects on the evolution of the structure of treated metal for improvement of its resistance to fatigue fracture.

The level of residual stresses determines the parameters of buckling of welded structures [8]. The EDT effects on the local deformation of the «bulge» type, arising during welding of a load-carrying system in the sheet hull structures, was investigated. The specimens of the AMg6 alloy of 4 mm thick were used (Figure 16). Figure 16, *a* shows the dimensions of the specimen, representing a plate, to which the stiffeners are rigidly welded-on applying argon arc welding by fillet welds. The welding mode corresponded to U_w = = 20 V, I_w = 180 A, v_w = 1.4 mm/s. After manufacture of specimens, the values of the deflection *f* were registered at the center of the specimen (Figure 16, *a*). Then, the treatment of the convex surface of the specimen applying the series of pulses with a pitch of 10 mm at the mode at U_{ch} = 500 V and the capacitance of CES C = 6600 μF was carried out. Figure 16, *b* shows the residual shape changes of the plate before and after EDT-straightening. It is seen that as a result of electrodynamic effects, the residual deflections *f* decrease to 1 mm, which is acceptable for the most welded products.

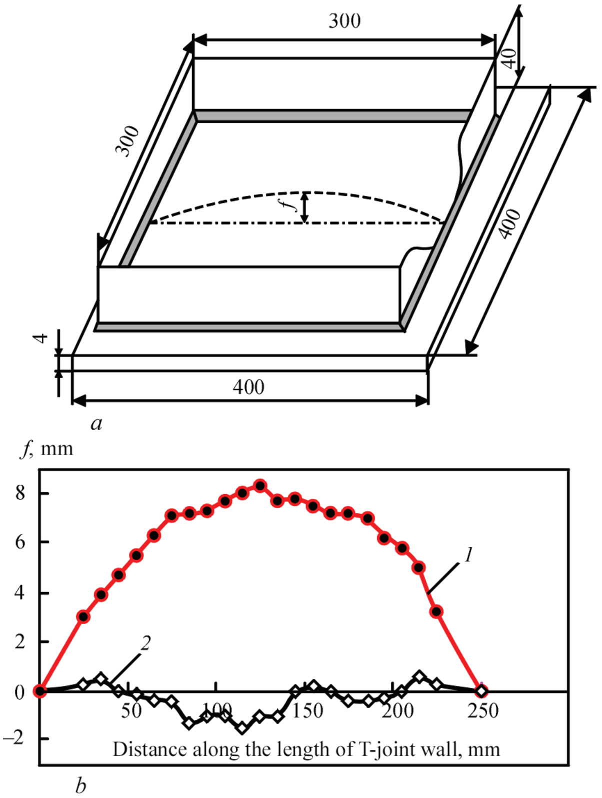

Figure 16. Specimen of welded joint of AMg6 alloy with a bulge: *a* — scheme of specimen (*f* — deflection); *b* — varying shape of specimen (curve *1* — initial deflections *f* in the center of the specimen; *2* — *f* after EDT)

EDT is applicable for increasing the life and reducing the residual stress-strain state of different types of welded structures.

Thus, the use of EDT in the manufacture and repair of small ships of the AMg6 alloy (Figure 17, *a*) allowed increasing the service characteristics of the products. EDT-straightening of structural elements

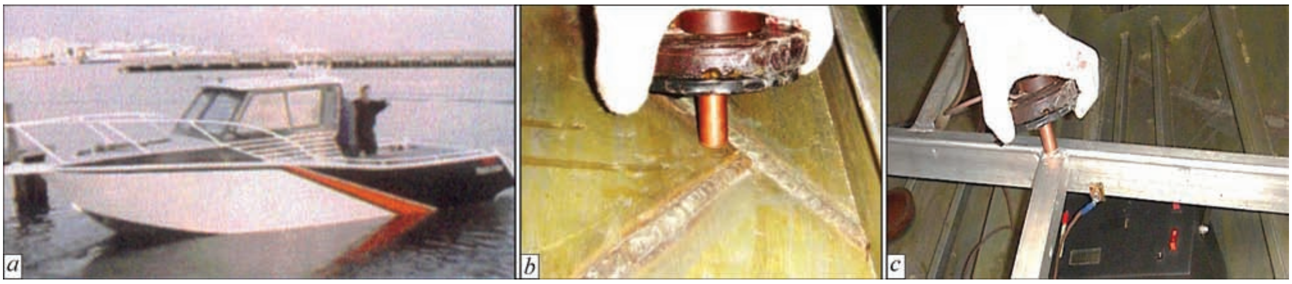

Figure 17. Using of EDT in the manufacture of ship hull of the AMg6 alloy: *a* — outer appearance of hull; *b* — EDT-straightening of welded joints of lining; *c* — EDT-straightening of the bottom beam structures

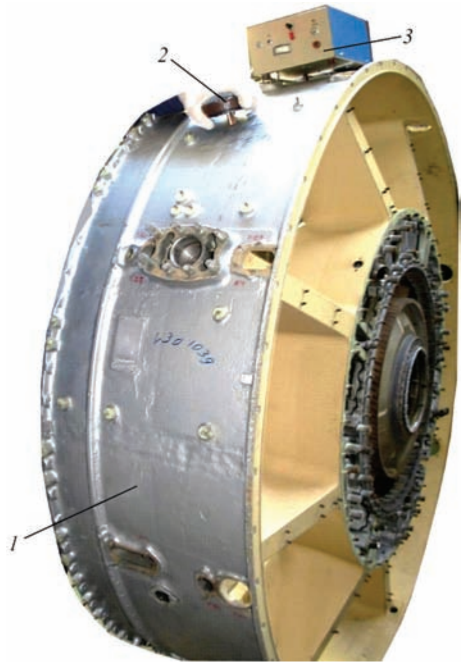

Figure 18. Treatment of repair weld on the outer surface of the outer shell of IBAE of the ML10 alloy applying EDT method: *1* — IBAE; *2* — electrode device; *3* — power source for EDT

allowed a significant improvement of hydrodynamic characteristics and habitability of hulls. Thus, the straightening of bulges in the lining (Figure 17, *b*) reduced the local deflections in the welded joint area from 10 to 1.5 mm, and the elimination of the curvature of transverse beams of bottom reinforcement (Figure 17, *c*) from 8 to 0.5 mm provided the guaranteed adjacency of bottom ceilings. At the same time the EDT of repair welded joints of lining and the load-carrying system provided a reduction in residual stresses from 150 to 40 MPa, which allowed 2–6 times extending the service life of the hulls.

The structural element of the aircraft AN-74 is the intermediate casing of the aircraft engine (IBAE), the purpose of which is mounting the engine D-36 to the wing. IBAE is a large-sized hollow cast structure of the heat-resistant magnesium alloy ML10 (Figure 18), which consists of the outer and inner cylindrical shells coupled between each other by stiffeners-struts, in the internal cavities of which the cooling fluid is circulating. The typical damages of IBAE, which are eliminated by repair welding, are fatigue cracks violating the integrity of the outer and inner shells, and also fracture on the front surface of the outer shell in the reinforcement zone under the flange of the cooling pipeline. Here, the maximum values of tensile stresses in repair welds without heat treatment reach 120 MPa, which corresponds to the yield strength of ML10 alloy. Reduction of stresses with the use of heat treatment is a rather expensive operation, which in some cases is by an order higher than the cost of repair welding. The application of EDT allows changing the distribution of residual welding stresses in repair welds from tensile to compressive ones, the value of which reaches –40 MPa, which is more effective than heat treatment, and much lower in cost.

The experience of practical using of EDT showed that one-channel ED, in view of their simplicity and a longer cycle of charge (as compared to two-channel ones) is advisable to apply for straightening the thin-sheet welded structures. At the same time, two-channel ones, due to the peculiarities of input of the pulsed current into the material treated, are most preferable for lowering the level of residual welding stresses. At the same time, a short charging time, typical for two-channel ED, allows using this type of EDT together with the welding cycle, which is promising for carrying out deformation-free welding of critical structures.

1. Baranov, Yu.V., Troitsky, O.A., Avramov, Yu.S. (2001) *Physical principles of electropulse and electroplastic treatment and new materials*. Moscow: MGIU.
2. Lobanov, L.M., Kondratenko, I.P., Zhiltsov, A.V. et al. (2016) Electrophysical unsteady processes in the system to reduce residual stresses welds. *Tekhnichna Elektrodynamika*, **6**, 10–19.
3. Sidorenko, Yu.M., Shlenskii, P.S. (2013) On the assessment of stress-strain state of the load-bearing structural elements in the tubular explosion chamber. *Strength of Materials*, 45(**2**), 210–220.
4. Kishkina, S.M., Bratashev, V.L., Guk, N.V. (1988) *Fracture of aluminium alloys: Atlas of fractograms*. Moscow: VIAM.
5. Yakovleva, T.Yu. (2003) *Local plastic deformation and fatigue of metals*. Kiev: Naukova Dumka.
6. Darovsky, Yu.F., Markashova, L.I., Abramov, N.P. (1985) Method of preparation for electron microscopic examinations. *Avtomatich. Svarka*, **12**, 60.
7. Lobanov, L.M., Pivtorak, V.A., Savitsky, V.V. et al. (2006) Procedure for determination of residual stresses in welded joints and structural elements using electron speckle-interferometry. *The Paton Welding J.*, **1**, 24–29.
8. Masubuchi, K. (1980) *Analysis of welded structures*. Pergamon Press.

Received 03.04.2017

doi.org/10.15407/tpwj2017.08.06

JOINT FORMATION IN MAGNETICALLY-IMPELLED ARC BUTT WELDING OF THICK-WALLED PIPES FROM HIGH-STRENGTH STEELS

V.S. KACHINSKY and **S.I. KUCHUK-YATSENKO**
E.O. Paton Electric Welding Institute, NASU
11 Kazimir Malevich Str., 03680, Kiev, Ukraine. E-mail: office@paton.kiev.ua

Searching for highly-efficient technologies of welding position butt joints of pipes is especially urgent, particularly during operation performance in site. The paper gives the results of comprehensive research on optimization of the technology of pressure welding of pipes with more than 4–5 mm wall thickness, using a controlling magnetic field. Methods of heating pipe edges by magnetically-impelled arc, algorithms of controlling the main parameters of pressure welding have been determined and comprehensive testing of the joints has been performed. Possibility of achieving high values of welded joint impact toughness in welding high-strength pipe steels is shown. 10 Ref., 7 Figures, 5 Tables.

Keywords: *pressure welding, controlling magnetic field, magnetically-impelled arc, thick-walled pipes, welding technology, site and stationary conditions, mechanical properties*

Ensuring stable quality of position butt welded joints of steel pipes made by highly efficient technologies is an urgent goal for companies in different countries, whose business is associated with pipe welding. Also important is lowering of welder's impact on the technological process.

The above-noted is especially relevant when making joints of pipes with greater (more than 4–5 mm) wall thickness, as well as when it is required to make joints in site.

This work is a study on enhancing the capabilities of pressure welding, in particular, under the impact of external controlling magnetic field (CMF). The following aspects were studied:

- behaviour of welding arc in a narrow gap of approximately 2 mm, between the edges of thick-walled pipes under the impact of external CMF;
- speed of arc movement during heating of thick-walled pipe edges;
- features of heating of thick-walled pipe edges;
- behaviour of liquid melt during pipe heating;
- influence of liquid melt on welded joint formation.

Technology of welding pipes with more than 4–5 mm wall thickness and equipment for magnetically-impelled arc butt pressure welding (MIABPW) of pipes in stationary and in site conditions were developed.

Technology application areas are as follows: welding gas and oil pipelines; welding tubes for systems of thermal stabilization of soil at down to –40 °C ambient temperature (more than 7 thou km of tubes have been welded, which keep all in all 25 mln m^3 of soil in the frozen state over an area of 2.5 mln m^2) hot house construction (more than 50 thou butt joints of tubes have been welded); industries, where butt welding of pipes to fittings, plugs, etc. is applied; welding tubular billets in manufacture of hydraulic cylinders (more than 17 thou butt joints have been welded).

The main features of MIABPW technology include the possibility of welding steel pipes in air, without using shielding gases, as well as implementation of technology of MIABPW of pipes with wall thicknesses greater than the dimensions of active spots of powerful arc discharges.

In application of MIABPW process, the welding arc moves under the impact of an external constant magnetic field. This welding method is applied in industry predominantly for joining parts of a tubular cross-section with up to 4 mm wall thickness and up to 100 mm diameter for automotive industry, with application of shielding gases [1–4]. PWI developed MIABPW technology and welded more than 7 mln hollow parts of automotive range without shielding gas application [5]. Development of technologies and equipment for MIABPW of various pipelines was performed [6]. Despite the high efficiency and other technological advantages, compared to electric arc methods, MIABPW process still has not become widely accepted in industry in critical power engineering plants, in particular, in boiler construction, high pressure gas and oil pipelines. This is largely due to limited information on mechanical properties of welded joints, made by MIABPW, as well as absence

Table 1. Chemical composition of steels, wt.%

Steel grade	C	Si	Mn	P	S	Cu	Ni	Cr	Mo	Ti	Nb	Al
09G2S	0.11	0.75	1.38	0.015	0.016	0.05	0.05	0.25	0.05	–	–	0.01
35	0.39	0.35	0.75	0.035	0.04	0.25	0.25	0.25	–	–	–	–
X70	0.030	0.156	1.45	0.004	0.004	0.30	0.14	0.07	0.20	0.022	0.062	–
01Star520	0.159	0.172	1.19	0.012	0.006	0.13	0.04	0.04	0.03	0.002	0.002	0.03
STPG410	0.25	0.34	0.9	0.024	0.033	–	0.001	0.001	–	–	–	–

of technology of MIABPW of pipes with more than 5 mm wall thickness.

Investigations conducted in this work were aimed at development of technology and equipment for MIABPW of position butt joints of pipes with 10–20 mm wall thickness from high-strength steels and development on their basis of the technology of welding up to 320 mm pipes with wall thickness, exceeding the dimensions of arc active spots, adapted to operation in site and under stationary conditions. Pipes from different steels were welded, in particular, X60, X70, X80, St35, STPG410, 01Star520. Table 1 gives chemical composition and mechanical properties of steels. Welding was performed in MIABPW machines of MD1, MD-205 type, developed at PWI.

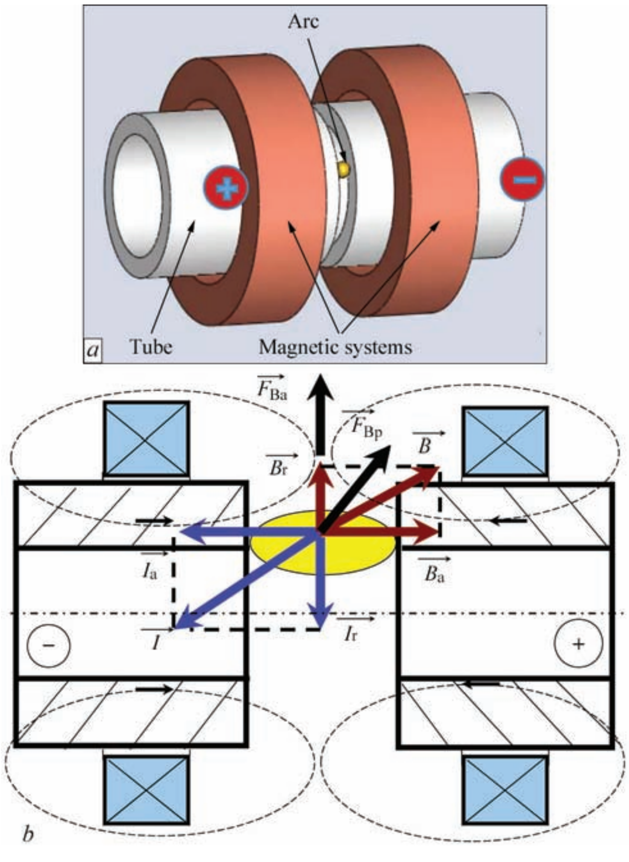

Figure 1. Pressure welding by magnetically-impelled arc: *a* — process schematic; *b* — forces applied to the arc ($\vec{B}$ — magnetic field induction; $\vec{B}_a$ — axial component of magnetic field induction; $\vec{B}_r$ — radial component of magnetic field induction; $\vec{I}$ — arc current; $\vec{I}_a$ — axial component of arc current; $\vec{I}_r$ — radial component of arc current; $\vec{F}_{Br}$ — force determining radial movement of the arc along pipe edges; $\vec{F}_{Ba}$ — force determining axial motion of the arc along pipe edges)

During welding operational control of the main process parameters, namely current, voltage, displacement and deformation force during upsetting, was performed. Processes running in the arc gap between the parts, were studied using high-speed video filming with a high resolution (up to 4500 fps), as well as oscillographing of the process. Welded joints were tested in keeping with the requirements of international standards for gas and oil pipelines (API, DNV).

Metallographic studies of welded joints were performed in «Neophot 32» optical microscope.

MIABPW process schematic is given in Figure 1, *a*. Under the impact of a powerful magnetic field, the arc moves in the gap between the edges of pipes being welded and heats them. Heating intensity is determined by arc current and rotation speed. After the required heating temperature has been reached, part edges are pressed together and the joint forms during their deformation.

As with other pressure welding methods, in order to produce sound joints in MIABPW, it is necessary to create the specified temperature field, and protect the part edges being heated. It is assumed [7, 8] that metal vapours formed at heating by the arc, create partial protection from oxidation in the gap. It is considered [4] that stable heating and protection of part edges from oxidation can be obtained only in the case, when diameter of active arc spots is identical to thickness of pipes being welded. Therefore, up to now MIABPW process was practically used for joining pipes with not more than 5 mm wall thickness that corresponds to the dimensions of active spots of powerful arc discharges, which can be obtained at currents of 1–2 thou A.

Technologies developed at PWI are based on the concept [9], in keeping with which at MIABPW, similar to flash-butt welding (FBW), the main condition for producing sound joints is formation of a layer of molten metal with oxides of its alloying elements, on the edges of parts being welded in the period prior to upsetting. As a result of melt heating by rapidly moving arc, it has a higher temperature than that of melting of the material being welded. It is experimentally established that at contact melting of steels the melt reaches the temperature of 1700 °C. Its solidification proceeds in the range of 1700–1370 °C. If deformation of heated part edges takes place in this period, the melt is completely pressed out of the butt together with the oxides. Duration of melt solidification period depends on thermophysical properties of materials being welded and accepted welding technology:

$$t_1 = \frac{\delta_1 \gamma q}{\lambda \frac{d\theta}{dx}_{x=0}}, \qquad (1)$$

where t_1 is the duration of solidification; δ_1 is the melt layer thickness; $d\theta/dx_{x=0}$ is the gradient of temperature field in near-contact layer; λ is the thermal diffusivity; q is the deposited metal heat content at temperatures, exceeding its melting temperature.

At selection of welding technology, it is possible to vary the conditions of part heating and partially — value δ_1. The most favourable conditions for formation of sound joints in the joint plane are in place in welding with minimum temperature field gradient that is associated with large energy input into the heating zone, and is unfavourable for formation of metal structure in the HAZ, particularly in welding high-strength steels. Therefore, searching for optimum technologies of MIABPW of above-mentioned steels was aimed at development of technologies, featuring minimum energy input and high gradients of HAZ temperature field.

Investigation of processes running in the arc gap at heating of pipe edges by a moving arc was performed on pipes of up to 320 mm diameter with up to $\delta = 12$ mm wall thickness using high-speed video filming. The main parameters of the process (CMF induction, arc current, voltage) were varied within the range of values accepted at MIABPW of such pipes. MIABPW is performed both using constant magnets and electric magnets. Constant magnetic systems were applied in production units developed at PWI.

Figure 2 shows photographs illustrating arc behaviour in the gap and edges heating in different periods of MIABPW of pipes. Arc current was equal to 200–250 A, arc voltage was $U_a = 25$ V. After arc excitation in the gap between the edges, the speed of arc movement is constantly rising, reaching from 50 to 240 m/s by the moment of upsetting performance, depending on pipe diameter, and pipe heating is performed (Figure 2, *a*). As edges temperature rises, melt thickness on them increases (Figure 2, *b*), the melt being retained on the surface of edges by surface tension forces. After a certain thickness has been reached, the melt starts moving in the same direction, under the impact of forces rotating the arc along the edges being heated (Figure 2, *c*). Adjustable speed of this movement can reach 3 m/s under certain conditions. Melt motion is due to the impact of electrodynamic forces and gas pressure in the arc gap, excited by moving arc column. Here, mixing of molten metal layer proceeds. Prior to upsetting, melt layer on the edges is quite uniformly distributed around the pipe perimeter and across its edge thickness (Figure 2, *d*). In the initial upsetting period, the gap between the edges decreases, and the arc discharge is stopped for the period of gap closing (Figure 2, *e*), which is 0.01 s long at upsetting speed of 200 mm/s. At gap reduction to the value of $2\delta_1$, a continuous interlayer of metal melt starts forming between the edges (Figure 2, *f*), which continues its circular motion under the magnetic field impact (current supply through the edges is not interrupted). This promotes melt replenishment and formation of a continuous interlayer across the entire section of pipes being welded. At the moment of gap closing, the melt is pressed out of the butt, and

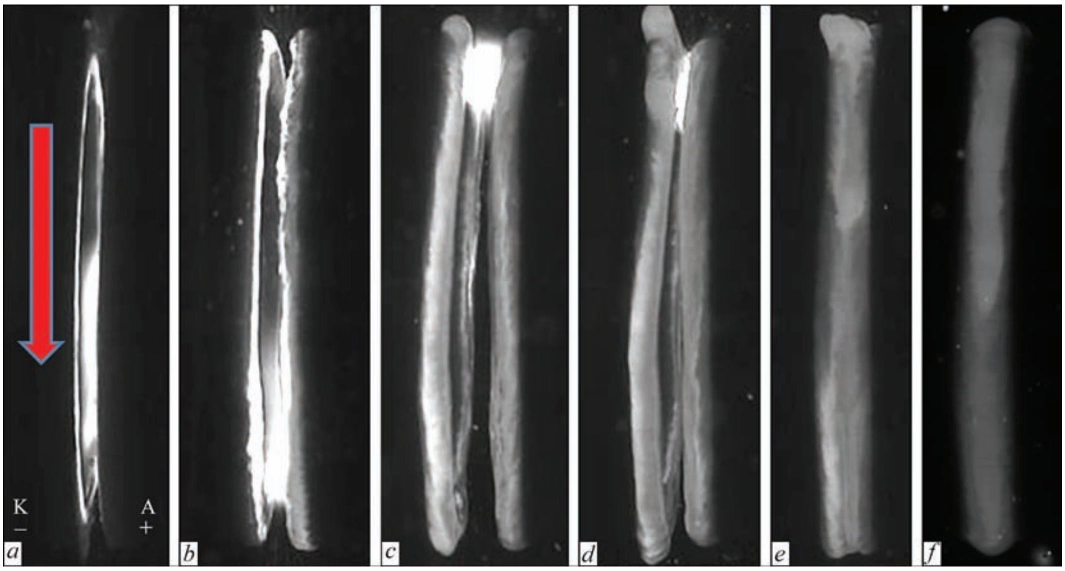

Figure 2. Stages of MIABPW of pipes: *a* — start of arc movement under CMF impact; *b* — formation of a melt layer on pipe edges; *c* — melt movement during heating; *d* — melt replenishment before upsetting; *e* — upsetting start; *f* — welded joint formation

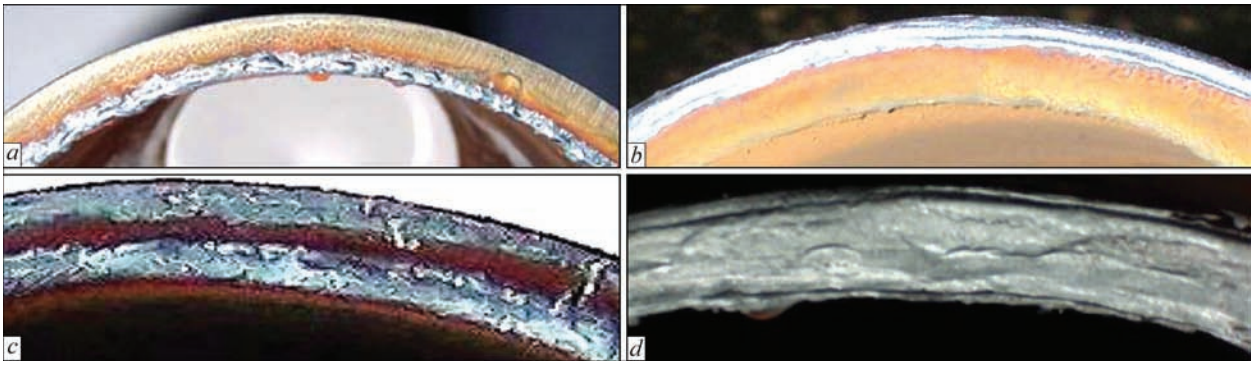

Figure 3. Control of arc movement on the surface of pipes being welded: *a* — arc moves along inner pipe edges; *b* — arc moves along outer pipe edges; *c* — arc scanning from pipe inner to outer edges; *d* — formation of a melt of stable thickness on pipe edges

deformation of heated metal layers in the solid phase takes place.

Given data show that melt behaviour in the period prior to upsetting, has a dominant influence on joint formation in MIABPW. In this period measured in hundredth of a second, the edge surface is not exposed to direct impact of the arc and is in contact with ambient air, surrounding the welding zone. Here, the area of the regions covered by liquid melt, can be much greater than that of the arc active spots, that leads to the conclusion about the possibility of forming sound joints in the regions of edges at sufficiently long periods of interruption of arc passage through these regions. This conclusion was the base for development of the technology of MIABPW of pipes with wall thickness much greater than the dimensions of active spots of powerful arcs.

Performed research of fast processes of melt behaviour in the gap at MIABPW was the base for development of algorithms for controlling MIABPW process parameters in different welding periods. Welding program envisages two periods. In the first period pipe heating takes place, which provides the specified temperature field and edge deformation. In the second period, preceding deformation (upsetting), formation of the melt is ensured in the gap, which is stable by thickness and is kept in the molten state due to intensive energy input. For this purpose, the process is briefly switched into arc contact heating mode that is accompanied by power increase. To provide a stable heating uniform across pipe thickness, as well as required conditions of melt formation in welding thick-walled pipes, PWI developed a system of arc movement control, the schematic of which is given in Figure 1, *b*.

After arc excitation in the gap between pipe edges, stable movement along the inner edge of pipe perimeter is provided, as a result of the impact of radial component $\vec{B}_r$ of magnetic flux induction (Figure 3, *a*). Stable movement of the arc along the pipe outer edge is ensured under the impact of axial component $\vec{B}_a$ (Figure 3, *b*). Periodical change of the value of above-mentioned components leads to scanning movements of the arc between the pipe outer and inner surfaces (Figure 3, *c*). Here, uniform heating of edges in the first period and melt formation in the second period are provided (Figure 3, *d*).

Analysis of mentioned features of heating by quickly moving arc allowed establishing the optimum program of controlling MIABPW parameters.

Based on the above-mentioned studies, PWI developed technologies of MIABPW of high-strength pipes of 60 to 219 mm diameter with 6–16 mm wall thickness. Table 1 gives chemical composition of some pipes in this category, Table 2 shows the main comparative parameters characterizing welding modes in MIABPW and FBW. Table 3 presents the main process parameters in MIABPW of pipes and gives similar parameters for comparison, which characterize the technology of joining similar pipes by flash-butt welding, developed at PWI.

Comparison of the given data shows that duration of the processes, as well as power consumed in MIABPW and FBW of pipes of the same dimensions, differs only slightly that is indicative of identical thermal efficiency of the processes.

Table 2. Main process parameters at MIABPW and FBW

Steel type or grade	Pipe size, Dn, mm	Welding process	Welding time, s	Upsetting force, kN	Heating allowance, mm	Upsetting allowance, mm	Consumed power, first period, kV·A	Consumed power, second period, kV·A
X70	Ø168×7	MIABPW	34.7	247	0	7.5	19.6	58.7
		FBW	37.2	177	15	8	25.1	60.2
35	Ø76×16	MIABPW	105	241	0	10	22.4	64.6
		FBW	120	168	36	19	40.2	98.4

Table 3. Main process parameters of MIABPW of pipes

Steel type or grade	Pipe size, Dn, mm	Welding time, s	Upsetting force, kN	Pipe shortening, mm
X70	168×7	34.7	247	8.5–8.9
01Star520	121×7	27	200	8.8–9.2
01Star520	121×10	43	278	10.7–11.2
35	76×16	82	255	16.4–16.9
09G2S	42×4	14	40.6	3.9–4.1
STPG410	60.5×5.5	19	80	5.8–6.8

Figure 4. Welded joint formation in MIABPW

In MIABPW, metal losses for flashing are much lower, than in FBW, but 1.5 times greater upsetting forces are required to produce sound joints. The latter is indicative of lower temperature of metal layers, subjected to deformation during upsetting. Formation of welded joints of pipes from X70 steels of 168×7 mm size by MIABPW, is shown in Figure 4. Control of pipe upsetting allowance enables significant reduction of welded joint reinforcement height, which is equal to 0.8 to 1.8 mm.

Mechanical testing of pipe joints made by MIABPW, which was performed in keeping with requirements of API and DNV standards, showed that strength and ductility properties of the joints are on the level of base metal values (Tables 4, 5).

As is known [10], an abrupt lowering of impact toughness values is observed at different methods of pressure welding of the above-mentioned steels, including FBW, particularly at low testing temperatures. Producing the required ductility properties of such joints requires additional heat treatment. All the joints of the above-mentioned pipes (Tables 2, 3) welded by MIABPW without heat treatment, had impact toughness values at testing temperatures of 20; –20; –40 °C not lower than 80 % of the respective base metal values.

This is achieved primarily due to energy input in welding and regulation of melt movement in the arc gap in the period, preceding deformation of heated edges prior to upsetting. Formation of a melt stable across the thickness δ_1 on pipe edges enabled producing sound joints at higher gradients of temperature field in near-contact region (Figure 5).

Temperature of near-contact layers and metal softening are reduced, respectively. Figure 6 gives the temperature fields in the heating zone in MIABPW and FBW of pipes of 168 mm diameter, δ = 7 mm. Heating temperature of near-contact layers at 2 mm distance from the melting surface at the moment be-

Table 4. Mechanical properties of base metal and welded joint of pipes at MIABPW and FBW

Steel type (welding process)	σ_y, MPa	σ_t, MPa	KCV_{+20}, J/cm^2	KCV_{-20}, J/cm^2
X70	448.9–469.1 460.6	528.8–566.8 551.0	248.4–265.7 256.5	248.4–265.7 256.5
X70 (MIABPW)	411–440 425.5	532–548 540	124.8–253.4 189.1	149.3–244.4 196.8
X70 (FBW)	–	536–543 539	31.6–238.4 134.5	29.2–141 85.3

Table 5. Mechanical properties of pipe welded joints

Steel type or grade	Pipe size Dn, mm	Base metal σ_t, MPa	Welded joint σ_t, MPa	Base metal KCV_{+20}, J/cm^2	Welded joint KCV_{+20}, J/cm^2	Base metal KCV_{-20}, J/cm^2	Welded joint	
							KCV_{-20}, J/cm^2	KCV_{-40}, J/cm^2
09G2S	42×5	460–478 469	453–484 465	57–5 58	59–78.1 68.5	57.8–58 57.9	64–74.5 69.3	–
35	89×10	538–565 551	528–554 541	56–64 60	52–965 70	–	–	–
01Star520	191×7	638–665 651	618–674 656	116–154 135	87–152 119	–	–	–
STPG410	60.5×5.5	452–464 458	450–462 456	90–98 94	86–92 89	102–104 98	87–94 91	88–94 92

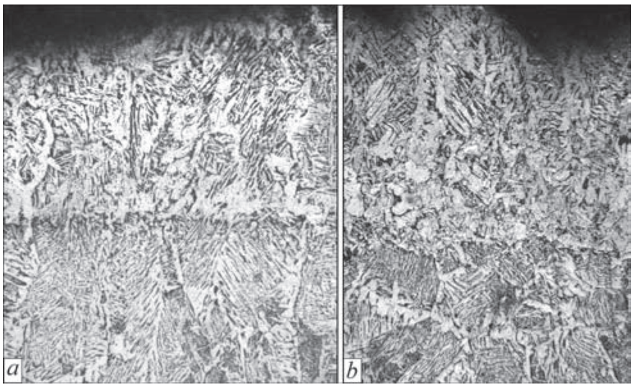

Figure 5. Microstructure of cast metal at the cathode (*a*) and anode (*b*) (×200)

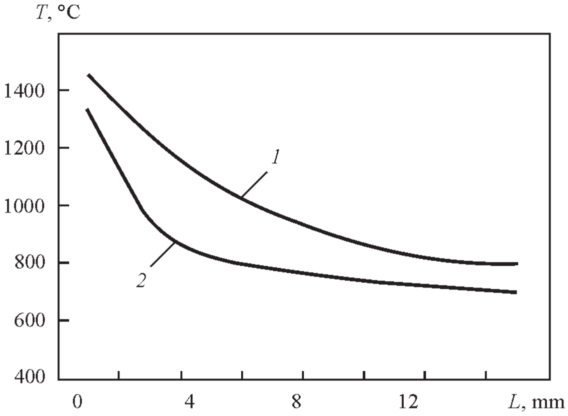

Figure 6. Temperature distribution at FBW (*1*) and MIABPW (*2*) (distance from the butt is given)

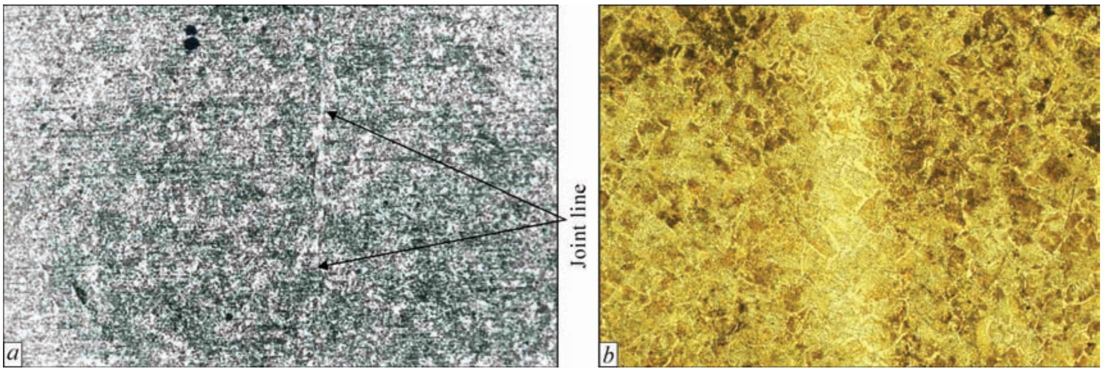

Figure 7. Microstructure of welded joints: *a* — at MIABPW (×150); *b* — at FBW (×100)

fore the start of deformation in MIABPW is equal to not more than 1050 °C, and in flash-butt welding of such pipes it is by 100 °C higher. It is experimentally established that an abrupt lowering of *KCV* values is observed at fast heating of samples from X70 steel up to the temperature of 1100–1150 °C.

As during deformation the structure of the weld central part and along the joint line is determined by the structure of these layers, temperature distribution given in Figure 6 (curve *2*), seems to be optimum at different pressure welding methods, in order to achieve high *KCV* values. Figure 7, *a* shows microstructure of a joint of pipes of 168 mm diameter, $\delta = 7$ mm, from X70 steel, made by MIABPW in the optimum mode (Table 2). Metal along the welding line has ferritic-pearlitic structure with ferrite precipitates in the form of an intermittent band of up to 10 μm thickness. In the central part the structure is fine-grained (grain size number 8, 9) with hardness *HV* 2470–2640 MPa. Total width of the HAZ in MIABPW was equal to 10 mm. For comparison, Figure 6, *b* gives an analogous structure in welding similar pipes by FBW. Structure along the welding line is coarse-grained (grain size number 3–5) with prevalence of pearlitic component and multiple clusters of polygonal ferrite, width of ferrite band being 100 μm. In this region lowering of hardness by 10 %, as well as of impact toughness, is observed, that is the consequence of overheating of near-contact regions up to temperatures of more than 1200 °C, in which formation of the weld took place (curve *1* in Figure 6).

Total width of the HAZ in FBW was equal to 18 mm. Sound joints at heating corresponding to curve *2* in Figure 6, were produced only at MIABPW. Application of such a heating mode at FBW leads to formation of defects along the joint line in the form of thin oxide films, although microstructure in the weld center is similar to that obtained at MIABPW. Possibility of producing sound joints at MIABPW at higher gradients of temperature field is due to formation of a melt stable across the thickness in the gap.

Minimum melt thickness at MIABPW of pipes is equal to 0.6 mm, and at FBW melt thickness varies in the range of 0.15 to 0.2 mm. In keeping with expression (1) formation of sound joints in MIABPW can be achieved at higher gradients of the temperature field in the HAZ. The given data are indicative of the fact that sound joints of high-strength steels in different pressure welding processes can be produced at relatively low temperature of heating of near-contact metal layers, if, alongside application of high-power density heat sources, formation of a melt stable across the thickness is ensured in the contact between the parts being welded, prior to upsetting.

Conclusions

It is found that the dominating factor determining formation of joints in MIABPW, is presence of a melt layer on pipe edges in the initial period of upsetting.

Methods were determined for uniform heating of pipe edges by a rotating arc, the thickness of which exceeds the diameter of the arc active spot.

Algorithms of control of the main parameters of MIABPW and process modes ensuring sound welding of high-strength pipes of up to 320 mm diameter with up to 16 mm wall thickness, were determined.

Comprehensive testing of joints of thick-walled pipes from high-strength steels made by MIABPW, has been performed, confirming strength of welded joints equivalent to that base metal and their high ductility properties. Possibility of achieving high values of impact toughness in MIABPW of high-strength pipe steels without heat treatment was determined.

Technologies for MIABPW of various pipes from high-strength steels of 20 to 320 mm diameter with up to 16 mm wall thickness were developed.

1. Hagan, D., Riley, N. (1979) MIAB welding. Part 2. Fabrication the Fiesta rear axle. *Metal Construction*, 625(**12**), 627–629.
2. Ganovski, F.J. (1974) The magnetarc welding process. Weld. Met. Fab., **June**.
3. *Kenji* Takagi, Hirokazu Otsuka, Fumiho Abakida et al. (1987) Establishment of optimum welding conditions of magnetically impelled arc butt welding and application to field operation. *IIW Doc. III–8801*.
4. Edson, D.A. (1982) Magnetically impelled arc butt welding of thick wall tubes. Ibid., *III-726–82*.
5. Kuchuk-Yatsenko, S.I., Kachinsky, V.S., Ignatenko, V.Yu et al. (2010) Magnetically-impelled arc butt welding of parts of automobile range of products. *The Paton Welding J*., **6**, 28–31.
6. Takagi, K., Aracida, F. (1982) Magnetically impelled arc butt welding of gas pipeline. *Metal Construction*, **10**, 542–548.
7. Gelman, A.S. (1950) *Resistance welding*. Moscow: Mashinostroenie.
8. Orlov, V.D., Dmitriev, Yu.V., Chakalev, A.A. et al. (1975) *Technology and equipment of resistance welding*. Moscow: Mashinostroenie.
9. (1992) *Flash-butt welding*. Ed. by S.I. Kuchuk-Yatsenko. Kiev: Naukova Dumka.
10. Kuchuk-Yatsenko, S.I., Shvets, Yu.V., Zagadarchuk, V.F. et al. (2012) Flash-butt welding of thick-walled pipes from high-strength steels of K56 strength class. *The Paton Welding J*., **5**, 2–7.

Received 02.06.2017

doi.org/10.15407/tpwj2017.08.07

EQUIPMENT AND TECHNOLOGY OF ANTICORROSION ELECTROSLAG SURFACING APPLYING TWO STRIPS

I.A. RYABTSEV[1], **A.A. BABINETS**[1], **V.N. KORZHIK**[1,2], **A.I. SITKO**[1,3] and **ZHAN YUIPENG**[2]
[1]E.O. Paton Electric Welding Institute, NASU
11 Kazimir Malevich Str., 03680, Kiev, Ukraine. E-mail: office@paton.kiev.ua
[2]Guangdong Welding Institute (E.O. Paton Chinese-Ukrainian Institute of Welding)
510650, China, Guangzhou City, Tianhe, Changxing Road, 363
[3]LLC «Scientific and Production Center «PLAZER»
[3]10-A, Filatova Str., off. 2/10, Kiev, Ukraine. E-mail: plazer2010@meta.ua

The E.O. Paton Electric Welding Institute together with the E.O. Paton Chinese-Ukrainian Institute of Welding and the SPC «PLAZER» developed the equipment and technology for anticorrosion electroslag surfacing applying strips. The effect of current, voltage and surfacing speed as well as the gap between the strips on the stability of electroslag process, geometric dimensions of deposited beads and volume of base metal in the deposited one were investigated. In the experiments the stainless strips ESAB 309LNb ESW with the cross-section of 0.5×60 mm and the flux ESAB OK 10.10 were used. The range of surfacing modes applying two strips was determined, providing a high efficiency and a stable electroslag process with a good formation of deposited metal and a minimal penetration of the base one in the ranges of 7–9 %: $I_s = 1400$–1500 A; $U_s = 32$–33 V; $v_s = 14$–17 m/h; the gap between the strips is 16 mm. The mechanical properties of the metal deposited at these modes applying the strips ESAB 309LNb ESW under the flux ESAB OK 10.10 are at the level of mechanical properties of steel 309LNb. The obtained results can be used in selection or development of materials and technologies for anticorrosion surfacing of parts of power and chemical equipment. 7 Ref., 1 Table, 6 Figures.

Keywords: *electroslag surfacing applying strips, surfacing technology, surfacing equipment, penetration, efficiency of surfacing*

To protect the parts of power and chemical equipment from corrosion, the electric arc surfacing under the layer of flux of a high-alloyed corrosion-resistant metal on low-carbon steel is widely used [1, 2]. The surfacing is mainly carried out applying one electrode strip with a thickness of 0.5–0.8 mm and a width of 50–70 mm, which, depending on the modes, provides the efficiency of 10–35 kg/h [2]. In this case, the volume of base metal (VBM) in the deposited metal is 15–25 % and to provide the necessary chemical composition of the corrosion-resistant deposited metal, the surfacing should be performed at least in two layers.

This reduces the efficiency of surfacing and can lead to accumulation of microdefects in the deposited metal, growing residual stresses in it, increasing chemical and structural heterogeneity [3]. Under service conditions, these factors can negatively affect the resistance of deposited metal against crack and corrosion formation [4].

One of the ways for solving this problem is the use of surfacing materials and methods which could provide a minimum penetration of base metal, in particular, electroslag surfacing applying two strips (ESSS). According to some data [5–7], this method provides obtaining the necessary chemical composition of the deposited metal already in the first layer, which is especially important for surfacing of high-alloy austenite steels on structural steel.

The scheme of electroslag surfacing process applying two strips is shown in Figure 1. The current supply, as a rule, is carried out through the copper insert located between the strips and providing a preset gap between them. The protection of surfacing zone from atmosphere is carried out by flux. During surfacing at the first moment of time an arc is occurred between the electrode strips and the product, which fuses the edges of the strip, facilitates the flux melting and the formation of a slag pool, shunting the arc. Further, the arc process is transferred into the slag one, since the current begins to pass through the molten electroconductive slag. The heating and melting of the strip, as well as fusion of the base metal, occur due to the heat transfer from the molten slag. Thus, the welding arc has no direct effect on the base metal, which leads to decrease in its penetration.

The E.O. Paton Electric Welding Institute together with the E.O. Paton Chinese-Ukrainian Institute of Welding (CUIW, Guangzhou, China) carried out works on implementation of the ESSS method in China.

The installation for ESSS includes: welding manipulator KM 2530, on the transverse beam of which a surfacing machine is mounted with a feeding mechanism for surfacing applying two strips and a device for supply and remove of flux after surfacing; a roller stand, on which the cylindrical parts, being surfaced, are installed; an inverter power source KAIYUAN ZD5-2000 and a computer control unit.

The manipulator KM 2530 consists of a column (including lifting mechanism, device for protection against falling and device for weight balancing), transverse beam with its drive of longitudinal movement and basement on which a column with a transverse beam is fixed. The basement, in its turn, is bolted to the floor in the surfacing workshop with the help of anchor bolts. The column, transverse beam and basement represent welded structures.

The lifting mechanism raises or lowers the traverse, which provides adjustment of the surfacing machine in a position convenient for surfacing. The drive moves the traverse with the surfacing machine in the longitudinal direction at the travel or surfacing speed. During surfacing of cylindrical parts, the traverse drive also produces a displacement of the welding machine per a surfacing step. The high accuracy of manufacturing the parts of the lifting mechanism and the traverse drive provides a stable and high-quality operation of the installation.

The installation is equipped with an inverter power source ZD5-2000 manufactured by the company Tangshan Kaiyuan Specific Welding Equipment Co., Ltd (China). When using this source, the rated surfacing current is 1650 A (DC = 100 %).

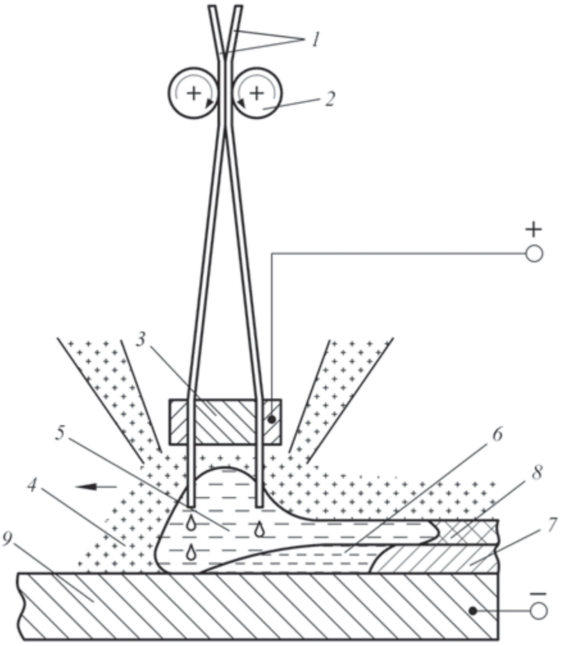

Figure 1. Scheme of electroslag surfacing by two strips [4]: *1* — electrode strips; *2* — feeding rollers; *3* — copper insert-current conductor; *4* — flux; *5* — slag pool; *6* — metal pool; *7* — deposited metal; *8* — slag crust; *9* — workpiece being deposited

For ESSS of cylindrical parts an adjustable roller stand KT5000 is used, which consists of a block of driving rollers and a block of auxiliary ones. A block of two pairs of driving rollers is mounted on a driving platform and has a drive system which sets a part deposited into rotation. A block of two pairs of auxiliary rollers is mounted on an auxiliary platform and does not have a drive system. The distance between the rollers of driving and the auxiliary blocks can be adjusted depending on different diameters of parts being deposited. The maximum load-carrying capacity of the stand KT5000 is 5000 kg, the diameter of the deposited parts is 500–3500 mm, the range of rotation speeds is 134–1340 mm/min. The current supply to

Figure 2. ESSS process of cylindrical specimen of 1000 mm diameter

the part deposited is carried out through the driving rollers with the help of sliding contacts.

The main technical characteristics of the installation for ESSS are given below, and the general appearance of the installation in the process of practicing modes of electroslag surfacing of a cylindrical specimen applying two strips are given in Figure 2.

Technical characteristics of the ESSS installation

Rated mains voltage, V	380
Frequency of supply mains current, Hz	50
Rated welding current of surfacing, A	1650 at DC = 100 %
Range of surfacing current adjustment, A	400–2000
Number of electrode strips, pcs	2
Thickness of cold-rolled strip, mm	0.5–1.0
Width of cold-rolled strip, mm	60
Ranges of smooth adjustment of strips feed speed, m/h:	
1 range	5–50
2 range	23–230
Surfacing speed regulation ranges, m/h	6–61
Vertical movement of surfacing machine:	
Travel, mm	400
Speed, m/h	24
Correction of electrode strips feed mechanism, mm:	
Along the deposited bead	90
Across the surfacing bead (by hand)	200
Adjustment of inclination angle of nozzlers, deg	±30
Travel speed of surfacing machine, m/h	800
Range of transverse oscillation speeds, m/h	29–118
Device for flux:	
Volume, dm^3	55
Air consumption, m^3/h	30
Height of flux suction, m	2

The computer control system of the installation allows monitoring the process of surfacing applying two strips with a high degree of automation. For example, during surfacing of cylindrical parts, the operator sets the surfacing modes and diameter of workpiece being deposited on the computer screen and presses the «Start» button. The control system, coming from the workpiece diameter, selects the rotation speed, displacement moment and value per step during closing of each circular bead. The control system of the installation is integrated with the power source control system, which allows conducting the process of surfacing in automatic mode and provides a high quality of surfacing. If necessary, the operator can interfere with the surfacing process and correct its modes.

In the installation the modes of electroslag surfacing by two strips were practiced on flat and cylindrical parts and the investigations of effect of current, voltage and surfacing speed, as well as the gap between the electrode strips on the stability of the electroslag process, the geometrical dimensions of the deposited beads and VBM in the deposited metal were carried out.

In the experiments the strip ESAB OK Band 309LNb ESW with cross-section of 0.5×60 mm and flux ESAB OK Flux 10.10 were used. The surfacing was performed on plates of steel St3 of 350×200×(30–40) mm, the current and voltage values varied within 1200–1600 A and 25–38 V, respectively. The speed of surfacing varied between 10–30 m/h, and the gap between the strips was 8–20 mm, the strips stickout remained unchanged and was 35–40 mm.

After surfacing, a layer-by-layer spectral analysis of chemical composition of the deposited metal was carried out, the results of which are given in the Table. The analysis of these data shows that in ESSS the preset chemical composition is achieved already in the first deposited layer.

The influence of current, voltage and speed of surfacing, as well as the gap between the strips on the stability of the electroslag process, the geometric dimensions and VBM were investigated. It was found that geometric dimensions of the deposited bead are almost directly proportional to the value of surfacing current and voltage, however, the value of VBM remains almost unchanged (Figure 3). This is explained by the fact that in electroslag process there is no direct effect of arc on the base metal, therefore the increase in electrical power mainly affects only the increase in the amount of deposited metal.

A greater influence on VBM is provided by surfacing speed as well as by gap between the strips (Figure 4). The surfacing speed determines the duration of thermal action of slag pool on the base metal, and the size of a gap significantly affects the stability *N* of running the electroslag process itself. The stability was determined according to oscillograms as a ratio of duration of periods of electroslag and arc processes for a certain time. At a small size of gap the slag pool

Chemical composition of strip of grade ESAB OK Band 309LNb ESW and metal deposited by electroslag method applying two strips of this grade

Material investigated	Mass fraction of elements, %							
	C	Mn	Si	Cr	Ni	Nb	S	P
Strip								
ESAB OK Band 309LNb ESW	0.015	1–2.5	≤0.4	20.0–22.0	11.0–13.0	0.4–0.8	≤0.03	≤0.03
Deposited metal								
1 layer	0.014	1.43	0.67	21.7	12.5	0.59	0.005	0.017
2 layer	0.017	1.47	0.65	21.4	12.4	0.63	0.005	0.017
3 layer	0.017	1.42	0.70	22.1	12.8	0.58	0.007	0.019

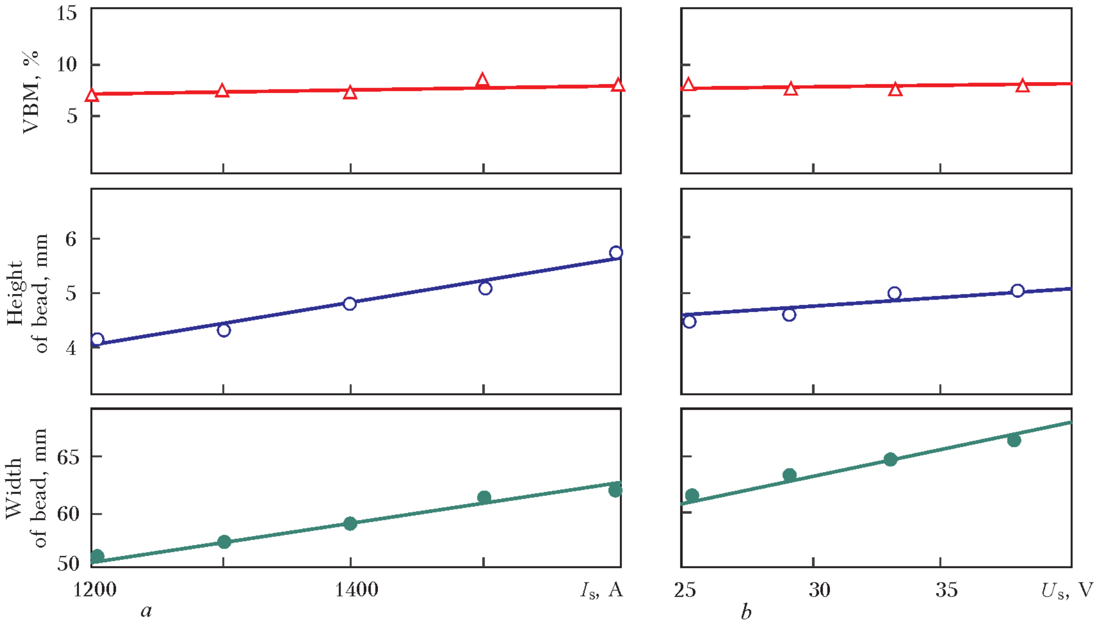

Figure 3. Influence of current I_s (*a*) and voltage U_s (*b*) of surfacing on geometric dimensions of deposited bead and VBM in the deposited metal

overheats between the strips, an unstable slag-arc process is observed, as a result, the penetration of base metal increases and its formation is deteriorated. As the gap increases, the area of the slag pool mirror increases, the pool temperature decreases and the electroslag process becomes more stable. At a width of 16 mm, the deposited bead has even edges and a smooth surface, i.e. the better formation (Figure 5, *a*) than the bead deposited at the same mode, but with a gap of 8 mm (Figure 5, *b*).

As a result of investigations it was found that a stable electroslag process applying strips of 0.5×60 mm section is reached at the following surfacing parameters: I_s = 1400–1500 A; U_s = 32–33 V; v_s = 14–17 m/h; feeding speed of the strip is 65–70 m/h; the gap between the strips is 16 mm. The metallographic examinations showed that specimens deposited at these modes are characterized by a good formation of deposited metal and minimal penetration of base metal within the range of 7–9 % (Figure 6, *a*, *b*). At the same time, the fusion boundary of the deposited and base metal is quite even, which positively affects the strength properties of the produced joint.

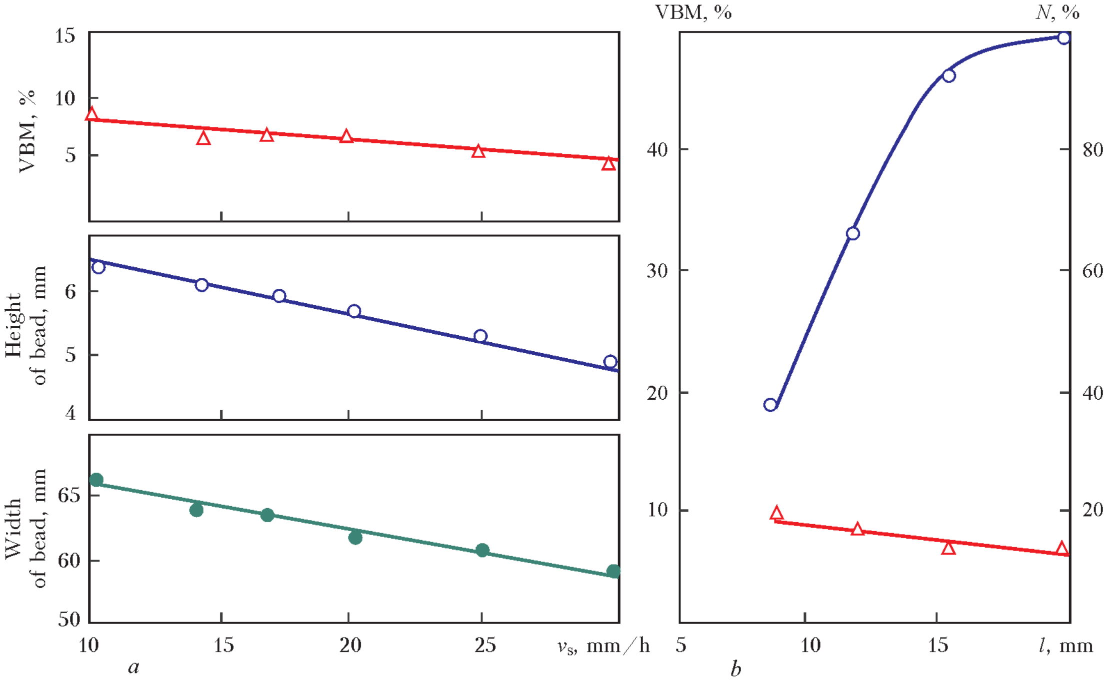

Figure 4. Influence of speed of surfacing v_s (*a*) and gap between the strips *l* (*b*) on geometric dimensions of deposited bead, stability of the process *N* and VBM in the deposited metal

Figure 5. Influence of gap between the strips l on formation of deposited metal: a — l = 8 mm; b — 16 mm. Surfacing mode: I_s = = 1200–1300 A; U_s = 32–33 V; v_s = 14 m/h

To determine mechanical properties of the deposited metal, a multilayer surfacing was carried out according to the abovementioned mode. The total thickness of the deposited metal was ≈ 20 mm, width was 62–65 mm. The specimens for mechanical testing were cut from the deposited billet. The mechanical properties of deposited metal of steel 309LNb at 20 °C are the following: σ_t = 504–506 MPa (≥510); σ_y = 286–297 MPa (≥205); δ = 44–49 % (≥25); ψ = = 64.0–69.7 % (≥60) (in brackets the data on mechanical properties of steel 309LNb are given).

The test results show that strength characteristics of the metal deposited applying strips ESAB 309LNb ESW are at a sufficiently high level and meet the requirements specified to them. The obtained results can be used to select or develop materials and technologies for anticorrosion surfacing of the parts of power and chemical equipment.

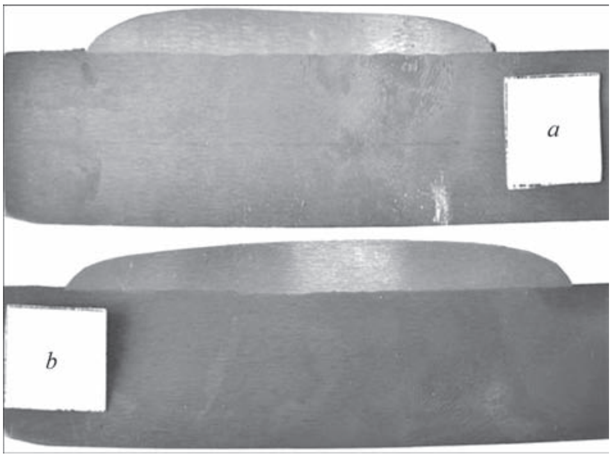

Figure 6. Macrosections of cross-section of specimens deposited at the modes U_s = 32–33 V; v_s = 12 m/h; l = 16 mm: a — I_s = = 1400 A (VBM = 7 %); b — I_s = 1500 A (VBM = 9 %)

The work was carried out at the support of program of foreign consultants No. WQ20124400119, Innovation research team of Guangdong province (China) No. 201101C0104901263, as well as research projects of China: No.2013B050800032 «Investigation and application of high-efficient welding equipment for arc welding» and No. 201508030023 «Development of submerged arc welding technology».

1. Kravtsov, T.G. (1978) *Electric arc surfacing using electrode strip*. Moscow: Mashinostroenie.
2. Ryabtsev, I.A. (2005) High-efficiency wide-layer surfacing using electrode wires and strips (Review). *The Paton Welding J*., **6**, 31–35.
3. Ivanov, V.P., Ivashchenko, V.Yu. (2011) Influence of hardfacing technology and heat treatment on structure and properties of metal deposited on carbon steel by LN-02Kh25N22AG4M2 strip electrode. *Ibid*., **8**, 7–9.
4. Ryabtsev, I.A., Senchenkov, I.K., Turyk, E.V. (2015) *Surfacing. Materials, technologies, mathematical modeling*. Glivize: Silesia Polytechnical Institute.
5. Frumin, I.I., Kalensky, V.K., Panchishin, Yu.A. et al. (1977) Development of process and investigation of some technological specifics of strip electroslag surfacing. In: *Theoretical and technological principles of surfacing. New processes of mechanized surfacing*. Kiev: PWI, 83–88
6. Kalensky, V.K., Panchishin, Yu.A., Shekhteri, S.Ya. et al. (1980) Application of electroslag surfacing using sintered strips for manufacture of two-layer sheet billets. In: *Theoretical and technological principles of surfacing. Properties and tests of deposited metal*. Kiev: PWI, 89–92.
7. Ignatov, V.A., Murzin, V.V., Rokhlin, E.A. et al. (1980) Examination of process of electroslag anticorrosion surfacing using two strip electrodes. In: Ibid.. Kiev: PWI, 101–106.

Received 25.04.2017

doi.org/10.15407/tpwj2017.08.08

NON-DESTRUCTIVE TESTING

CURRENT ACHIEVEMENTS IN RADIATION TESTING (REVIEW)

V.A. TROITSKY, S.R. MIKHAILOV and **R.O. PASTOVENSKY**
[1]E.O. Paton Electric Welding Institute, NASU
11 Kazimir Malevich Str., 03680, Kiev, Ukraine. E-mail: office@paton.kiev.ua
[2]NTUU «Igor Sikorsky Kyiv Polytechnic Institute»
37 Pobedy Str., 03056, Kiev, Ukraine. E-mail: fel@kpi.ua

A paper studies a prospective method for receiving a digital image on results of radiation testing without intermediate data carriers. Advantages of flash-radiography were analyzed, namely high productivity, low cost, possibility of on-line multiangle monitoring of welded joint internal defects; absence of intermediate data carriers. Comparison of main methods of digital image receiving was carried out. New radiation testing technology based on small-size semi-conductor detectors, named X-ray mini technology, was proposed. 24 Ref., 4 Figures.

Keywords: *non-destructive testing, flash-radiography, digital image, X-ray TV system, scintillator, solid-state detector, internal defects of welded joints, X-ray minitechnology*

Radiation testing is the most widespread type of non-destructive testing (NDT) of quality of welded joints, materials and products. NDT radiation methods can be applied to products of any materials and exceed other types of NDT (acoustic, magnetic particle, eddy-current etc.) on amount of information about defects (type, shape, size, location etc.) [1].

Significant qualitative transformations in possibilities of radiation NDT took place in the recent years due to appearance of new multi-element semi-conductor detectors of radiation images as well as intensive implementation of digital technologies of receiving, processing and analysis of the images. Ionizing radiation passed through controlled object and containing information on internal defects, is transformed with the help of electron means applying these detectors and digital technologies in electric signals array. The later are digitized, processed and used for formation of digital image (DI) of the tested object. DI contains information on internal structure of scanned object, and can be observed during exposure, i.e. on-line. Such a radiation testing method without consumables and intermediate data carriers that allows obtaining on-line DI is called flash-radiography [2]. Possibility of computer processing and DI analysis, development of electron archives of DI, their documenting and further transfer using computer networks shall be referred to important advantages of the flash-radiography.

The peculiarity of flash-radiography is absence of intermediate data carriers, namely radiography films, memory plates with photostimulation memory. Currently widespread technologies with intermediate data carriers require ambiguous operations of exposure, processing and expensive devices for reading and digitization of information for mode selection. Absence of intermediate data carriers (films, memory plates), respectively, allows an order increase of productivity and significant decrease of cost of product quality control.

Methods of DI receiving. Examination of internal defects of the object using portable X-ray television equipment with digital processing of images should fundamentally change technology of radiation NDT in the coming years. In recent time, concept of «digital image» (optical or radiation) finds more and more application in flaw detection. Hardware and software complexes for processing and digitization of X-ray films and forming DI are currently very widespread [3]. The DIs are also received using memory plates employed instead of X-ray films [4–7]. The methods and algorithms of DI processing are common for three variants of radiation testing (Figures 1–3). This is an important direction in modern radiation flaw detection. Today, in majority of cases the DIs are obtained by digitization of radiographs. Less often it is obtained in processing of latent image being read from the multiple use memory plates. The same results can be received using digital flash-radiography detectors without additional expenses related with intermediate data carriers [2, 8, 9].

Figure 1 shows typical technological scheme for DI obtaining by means of digitization of film radiographs. This traditional technology is widespread all

Figure 1. Traditional scheme of radiography testing using film and digitization of radiographs: cassette charging (*1*); exposure on X-ray film (*2*); procedure of film treatment (*3*); film scanning (*4*); DI (5)

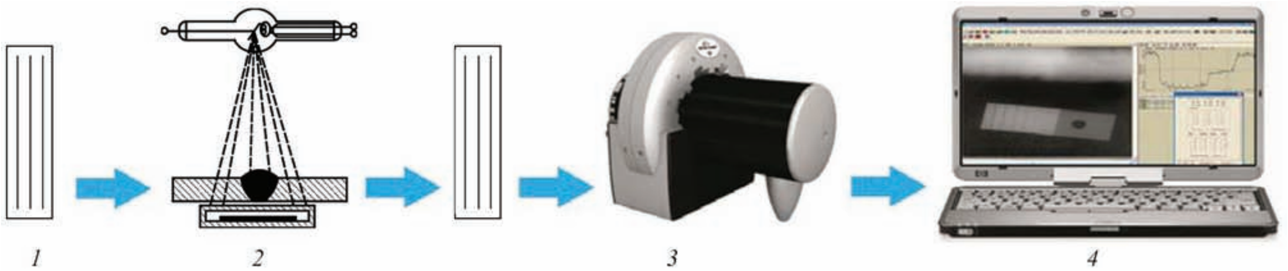

Figure 2. Scheme of exposure procedure using memory plate: preparation of cassette with memory plate (*1*); exposure on memory plate (*2*), reading from plate (*3*); DI (*4*)

over the world in all branches of industry. It requires preparation of a cassette with film and screens. The next procedures are used after exposure, i.e. chemical processing, film drying, reading of information on X-ray film viewer and digitization of the results using corresponding computer complex. This technology is mainly applied for compact archiving of NDT results in e-form and receiving additional information, which can not be gotten without digitization.

Figure 2 shows a scheme of more advanced technology of DI receiving based on memory plates (computer radiography). In comparison with the previous scheme for DI receiving this technology provides the possibility of multiple use of the intermediate data carrier (memory plate). This variant does not include wet process of development and other mandatory procedures.

Figure 3 gives a scheme of technology of instant (flash) digital radiography based on fluoroscopic and solid-body detectors [10, 11]. This is the quickest and cheapest method of DI receiving in e-form, which does not require processing and reading equipment and corresponding additional time.

Work [12] provides comparison of quality of the images obtained with the help of different detector systems. A procedure for calibration and subtraction of transducers' own noises was developed for the technology without intermediate data carriers. This is a method to enhance contrast sensitivity in such a way that it is possible to note the changes of 1/1000 radiation thickness, whereas the best films of C1 grade on European EN 584-1 and American ASTM E 1851 standards have the best contrast 1/100.

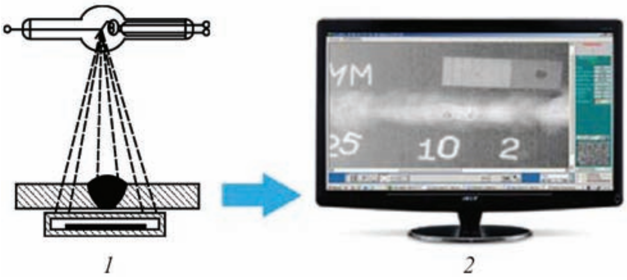

Figure 3. Exposure scheme without intermediate data carriers: exposure on solid-body detector (*1*); DI (*2*)

The quality of X-ray image can be determined on image quality indicators (GOST 7512–82). Classification of welded joints based on the results of radiography testing is carried out on GOST 23055–78. The larger density and the longer exposure are, the more information will contain the exposed film. Therefore, a good scanner is necessary for digitization of dense films and receiving more informative DI. Widespread reader units and cheap scanners can not provide high quality of digitization of radiographs if their relative density is more than 3 units. All the attempts to get satisfactory DIs from denser films were unsuccessful. Therefore, in the film version (Figure 1) satisfactory DI is possible only if film optical density is in 1.5–2.5 units range. The noises of a digitizing unit do not introduce irretrievable distortions in the DI under such values. Experience of digitization of the film images with 3–3.2 units density has already shown unsatisfactory results and it is difficult to reproduce fine information. For example, images of small pores of less than 0.2 mm and cracks with small opening are lost. Thus, digitization of the films has significant limitations. Part of the defects being detected with the help of X-ray film viewer can not be found in the DI. This is significant disadvantage of the traditional film radiography, which virtually can not be overcome in real production.

Film-free technologies on schemes of Figures 2 and 3 do not have this disadvantage, they differ by large dynamic range that expands NDT capabilities.

A special interest is the technologies based on small, several square centimeters, solid-body digital electron transducers. They do not have limitations related with cassette size, screens and memory plates. Mobile transducers can be freely moved over object surface. Such possibilities are embedded in the diagnostics of widely used in practice large customs objects, which can have significant dimensions [13]. It is virtually impossible to control similar objects using intermediate data carriers (films, memory plates). Miniature solid-body transducers can cover structures of different shape. The images from separate small transducers are connected in the one image of the complex-shape object.

Intensive works on improvement of solid-body electron transducers, and mobile X-ray television flaw detectors, which replace ultrasonic equipment due to better flaw detection capabilities [14], are carried out in the USA, Japan and other countries. This tendency will gain acceptance in other countries in time.

In the USA, Japan and Europe tens of companies have already manufactured the solid-state digital transducers virtually for any tasks of radiation testing [15–17].

Comparison of possibilities of separate methods of radiation testing needs consideration of dynamic range. These are object thicknesses, available for satisfactory analysis in one image. Large dynamic range provides substantial advantages to the technologies on scheme of Figures 2 and 3 in comparison with film radiography. Usually large dynamic range is reached by exposure dose that is limited with 3–4 units density in the film systems. Further, the films become unreadable at large film densities. In the case of digital detector systems (without intermediate carriers) «exposure», i.e. data storage has no limitations thanks to computer technologies. At that signal-to-noise ratio (SNR) grows proportional to dose square root. This is equivalent to exposure time or amount of averaged images. This is a way for reaching SNR ratio equal to several thousands and high DI quality. In practice this process is limited with contrast sensitivity of 0.1 % that corresponds to SNR of 1000 order.

Digital processing of the images is accompanied by the protocol procedures. They include operations on DI suitability evaluation, measurement of grey intensity, optical density and determination of sensitivity. Digital scale of grey is usually of 16-bits [4], has thousand of shadows and DI histogram should be located approximately in the middle of this scale in order to eliminate lack of exposure or overexposure. The central location of the histogram provides the possibility of more quality digital processing, i.e. allows carrying scaling of grey gradation. Calibration on size is applied. It allows measuring defects, fulfill other procedures, which are not typical for traditional film radiography and ultrasonic testing.

Significant achievements of radiation transducers based on movable scanning bars with the detectors, which find application in customs control [18], should be noted. All attempts to use such transducers for testing of welded joints have been unsuccessful up to the moment. These systems are continuously improved.

Recently, developers of fluoroscopic transducers on «scintillator screen–objective–CCD-matrix» have made a good progress [1, 19, 20]. Success of these transducers lies in quality of single crystal CsI (Tl) and powder $Gd_2O_2S(Tb)$, $Gd_2O_3(Eu)$ screens and enhanced video cameras. It is important to know how to select optimum screen. For that, their detection quantum efficiencies (DQE) $\eta_{q.e.}$ are compared. DQE is one of the most important complex parameters, determining efficiency of energy conversion in digital detector. DQE is determined on formula [20]:

$$\eta_{q.e} = \frac{\psi^2_{out}}{\psi_{in}}, \qquad (1)$$

where ψ_{in} and ψ_{out} are the relationships of SNR at system input and output, respectively.

DQE provides the possibility of making a conclusion on appropriateness of application of that or another screen for specific task, solved with X-ray TV system (XTVS) of «scintillator screen–objective–CCD matrix» type. Such systems have a series of advantages over other ones, namely possibility of replacement of scintillator screen, that allows varying size of working field and other parameters of the system; small time of image receiving; simple design; small dimensions and weight; low price.

Carried investigations showed that rise of value of exposure dose P_D from zero promotes gradual increase of ψ_{in} and ψ_{out} in the beginning. Dependence of SNR ratio at the input rises step-by-step and at specific value of power of exposure dose reaches the maximum and then start decreasing.

The maximum corresponds to a signal of complete filling of charge pixel of CCD matrix, further the signal is limited. Thus, drop of the value of quantum efficiency of transducer is mainly determined with a range of X-ray radiation energy, which can be absorbed by the screen, and charge in the pixel, which can be accumulated per one cycle. Such transducers due to storage using simple technical means can reach sensitivity of commercial X-ray films.

Calculated dependencies of the SNR ratio at XTVS output on the input power of exposure dose of X-ray radiation allow determining the optimum values of power of exposure dose for set durations of image storage in CCD-matrix. These values provide the highest SNR ratio and the best defect detectability. Investigations [20] showed that the quantum efficiency of X-ray TV system with Gd_2O_3(Eu) is higher than in the systems with CsI (Tl) and Gd_2O_2S(Tb) screens.

In the transducers with CsI (Tl) screen at exposure power more than 0.2 mR/s the value of quantum efficiency varies substantially less at increase of P_D than in XTVS with Gd_2O_2S(Tb) and Gd_2O_3(Eu) screens. In the transducer with CsI (Tl) screen the range of P_D variation, which has comparative consistency of quantum efficiency, depends on storage duration. Rise of storage duration in the CCD-matrix increases the value of quantum efficiency for all screens. A storage time is incommensurably lower than additional time, which is necessary for radiation testing with intermediate data carriers. Therefore, flash-radiography based on fluoroscopic transducers is of the same prospects as the transducers based on expensive solid-body detectors of direct conversion.

X-ray mini radiation testing technology. Not expensive small-size solid-body detectors can be used in modern X-ray TV systems. A new technology based on such small-size detectors is called X-ray mini [21, 22]. In contrast to traditional film radiography or computer radiography, which use expensive films or memory plates as detectors, the X-ray mini technology allows significantly reducing cost and rising efficiency of testing as well as providing virtually instantaneous results. An important peculiarity of X-ray mini technology is diminutiveness of the X-ray detector that allows carrying rapid X-ray testing of difficult-to-reach assemblies of operated planes, turbines, reactors etc.

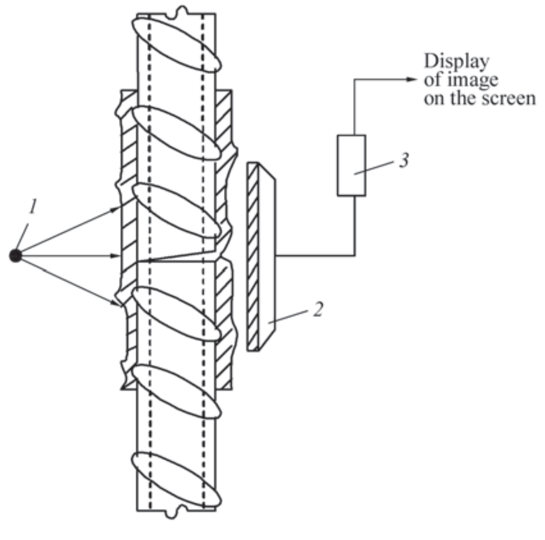

Figure 4. Scheme of X-ray TV testing: *1* — emitter; *2* — solid-body detector; *3* — electron transducer (description *1–3* see in the text)

For example, S10811-11 type detectors from Hamamatsu Photonics Company (Japan) with operating field size 34×24 mm, thickness 6 mm, pixel size 20 μm and number of pixels 1700×1200 provides testing sensitivity and resolution capacity up to 20 pairs of lines/mm. The E.O. Paton Electric Welding Institute uses such X-ray mini technology for testing of welded joints of different products, condition of honeycomb structures of aircrafts, composite structure, examination of closed spaces, where location of traditional films or memory plates is impossible.

X-ray image detector is used for the X-ray mini technology realization. Its area is two times smaller than the area of traditional cassettes with film, memory plates or solid-body detectors of standard size. Thanks to small size such miniature solid-body detector can be located in any difficult-to-reach or constricted space as well as moved on curved surface of the tested object. Such scanning allows examining found defects and inhomogeneities of the tested object in different angles. Information on internal structure of examined area of the tested object comes to a display on-line. The main difference of X-ray mini technology from known digital radiography based on solid-body detectors lies in the fact that cost of such miniature detector is ten times lower than cost of standard size detector [23, 24].

Interesting solutions based on X-ray mini technology were received in construction during control of welding quality or mechanical joints of separate parts of bearing reinforcement bars (Figure 4).

Construction of high-store buildings and other critical buildings is related with butt welding of large amount of the reinforcement bars. The most loaded butt joints shall be controlled by physical methods. In most cases, until recently, this was carried out using ultrasonic testing (UT) means. UT method is effective only in the cases when a butt joint is well dressed and treated. Corresponding claws, binding gel, clamping ultrasonic transducers for joining reinforcement bars parts are used for this. However, currently, application of UT is stopped due to lack of its effectiveness after distribution of mechanical joints of reinforcement bars with the help of crimp pipes. Ultrasonic radiation can not examine the gaps, which are natural for the mechanical joints made by crimping (Figure 4). Therefore, today such butt joints of bearing reinforcement bars are controlled using X-ray mini technology.

Application of film radiography under construction site conditions is unreasonable, since it requires special premises for chemical and other types of film treatment, X-ray film viewer for analysis of test results. Portable X-ray TV detectors, which are fixed to tested joint before testing, significantly accelerate process of quality evaluation of reinforcement bar joints. At that looseness of adjoining due to unsound crimping and bad bar mating are found at that.

The X-ray TV testing, in contrast to radiography one, provides flash result, does not require consumables and special procedures of treatment of radiography film.

Figure 4 shows the scheme of X-ray TV testing using solid-body detector. In this case, the same as in radiography testing, emitter *1* (radioisotope source or X-ray apparatus) is located in front of tested joint, on the opposite site of which is solid-body detector *2*. Image from solid-body detector through electron transducer *3* is shown on the monitor screen. Smartphone or tablet with USB interface can be used as a monitor. Thus, it is on-line control of crimp quality of joint tube (presence of butt gap, reduction of reinforcement bar section etc.).

Conclusions

1. Significant disadvantages of traditional film radiography are low productivity and high cost of testing as well as need in X-ray film viewer with powerful light sources. Exposed images can not be decoded and their digitization becomes impossible at relative density of more than 4 units. This disadvantage is absent in modern technologies based on miniature solid-body detectors.

2. Electron digital information on testing results contains visual demonstrations of internal structure of the objects, expands the capabilities of flaw detection, rises productivity and reduces cost of radiation testing of welded joint quality.

3. X-ray mini technology allows examining internal defects of the objects in different angles that is virtually impossible for other testing methods. The solid-body transducers can be located and moved in the zones, where location of cassettes with films or memory plates is almost impossible. Such technology is realized on serial equipment and allows more than order reduction of testing control in comparison with radiography based on planar detectors of standard size.

4. Scanning of complex surface with miniature detectors and joining of the images of separate exposures allows controlling extended objects from different angles. Corresponding auxiliary equipment is developed for scanning of particular objects using miniature detectors.

1. Troitsky, V.A., Mikhailov, S.R., Pastovensky, R.A. et al. (2015) Modern systems of radiation nondestructive testing. *Tekhn. Diagnostika i Nerazrush. Kontrol*, **1**, 23–35.
2. Troitsky, V.A. (2013) Flash-radiography. *Territoriya NDT*, **4**, 44–49.
3. Grudsky, A.Ya., Velichko, V.Ya. (2011) Digitizing of radiographs it is not so simple. *V Mire Nerazrush. Kontrolya*, **4**, 74–76.
4. Tsvetkova, N.K., Novitskaya, K.A., Kologov, A.V. et al. (2014) Peculiarities of application of digital radiography complexes in nondestructive testing of bodies production. *Tekhnologiya Mashinostroeniya*, **7**, 47–50.
5. Stepanov, A.V., Lozhkova, D.S., Kosarina, E.S. (2010) *Computer radiography: Results of practical examinations for potential replacement of film technologies*. Moscow: VIAM.
6. Sosnin, V.V. (2008) Book 1: Visual and measuring control. Book 2: Radiation control. Ed. by F.R. Klyuev. In: *Nondestructive testing*: Refer. Book, Vol. 1. Moscow: Mashinostroenie.
7. Varlamov, A.N. (2014) Experience of operation of digital radiography complex in field conditions. *V Mire Nerazrush. Kontrolya*, **3**, 25–28.
8. Troitskiy, V. (2016) Quick industrial X-ray testing without intermediate data carriers of information. *The NDT Technician*, **4**, 15.
9. Zscherpel, U., Ewert, U., Bavendiek, K. (2007) Possibilities and limits of digital industrial radiology: The new high contrast sensitivity technique — Examples and system theoretical analysis. In: *Proc. of Int. Symp. on Digital Industrial Radiology and Computed Tomography — DIR 2007* (June 25–27, Lyon, France).
10. Ferreira de Olivera, D. (2016) Relationship between image plates physical structure and quality of digital radiographic images in weld inspections. In: *Proc. of 19th World Conf. on Non-Destructive Testing* (13–17 June, Munich, Germany).
11. Iovea, M. (2016) Fast X-ray digital radiography equipment for in-line production control. In: *Proc. of 19th World Conf. on Non-Destructive Testing* (13–17 June, Munich, Germany).
12. Majorov, A.A. (2009) Digital technologies in radiation testing. *V Mire Nerazrush. Kontrolya*, **3**, 5–12.
13. Kokkoori, S., Wrobel, N., Hohendorf, S. et al. (2015) Mobile high-energy X-ray radiography for NDT of cargo containers. *Materials Evaluation*, 73(**2**), 175–185.
14. Troitsky, V.A. (2015) New possibilities of radiation control of quality of welded joints. *The Paton Welding J.*, **7**, 51–55.
15. Liang, L. (2016) The relationship study between penetration thickness ratio and an imaging length in digital radiography. In: *Proc. of 19th World Conf. on Non-Destructive Testing* (13–17 June, Munich, Germany).
16. Vieyra, M. (2016) Development of a tangential neutron radiography system for monitoring the fatigue cracks in hydrogen fuel tanks. In: *Ibid*.
17. Duerr NDT GmbH and Co. KG, *http*://duerr-ndt.de/ru/product.
18. Yatsenko, S.Ya., Kokorovets, Yu.Ya., Lozenko, A.P. et al. (2015) X-ray television systems Polyscan. *Tekhnich. Diagnostika i Nerazrush. Kontrol*, **1**, 60–62.
19. Majorov, A.A. (2007) X-ray television in industrial NDT. *V Mire Nerazrush. Kontrolya*, 35(**1**), 4–9.
20. Shilo, D.S., Mikhajlov, S.R., Pisarenko, L.D. (2016) Quantum efficiency of detection of digital X-ray television systems on the basis of scintillation screens and CCD matrices. *Nerazrush. Kontrol i Diagnostika*, **4**, 25–37.
21. Troitsky, V.A., Mikhajlov, S.R., Pastovensky, R.O. (2017) X-ray mini technology based on solid-state detectors. *Tekhnich. Diagnostika i Nerazrush. Kontrol*, **1**, 25–29.
22. Troitsky, V.A., Mikhajlov, S.R., Bukhensky, V.N. et al. (2014) Flash-radiography of NPP objects on the basis of flat panel detectors. *NK-Inform*, 63(**3**), 6–14.
23. Troitsky, V.O., Karmanov, M.M., Mikhajlov, S.R. et al. (2016) *Device for X-ray television control*. Utility model pat. 111974, Ukraine.
24. Troitsky, V.O. (2017) *Method of X-ray television control of welded joints*. Utility model pat. 113257, Ukraine.

Received 04.04.2017

MEETING WITH MANAGEMENT OF UKRAINIAN-ARAB BUSINESS COUNCIL AT PWI

On July 10 negotiations of the management of Ukrainian-Arab Business Council (UABC) with PWI directorship and leading specialists were held at PWI. UABC delegation consisted of: Sheikh Imad Abu Al-Rub, UABC President; Abdullah Al-Dweik, Qatar representative; O. Berezyuk, UABC Vice-President; M. Oliferenko, Cand. of Sci. (Eng.), Chairman of UABC Expert Council; M.Strikha, Dr of Sci. (Eng.), Deputy Minister of MES of Ukraine; B. Bazilevsky, Extraordinary and Plenipotentiary Ambassador of Ukraine, V. Komarnitsky, Cand. of Phys.-Math. Sci., Chairman of UABC Expert Council; S. Oksner, Assistant-Consultant of UABC President; R. Nechaj, Representative of MFA of Ukraine, V. Frindak, translator.

Academician I.V. Krivtsun, PWI Deputy Director, on behalf of academician B.E. Paton, PWI Director, PWI scientists and specialists, welcomed UABC management, and expressed his desire to familiarize the guests with the range of the Institute's activities within the framework of the first introductory meeting. He noted that the Institute's scientists prepared presentations, which may be of interest for specialists from Arab countries, and at the same time, will provide information about PWI activities.

Then I.V. Krivtsun described the history of the Institute establishment (1934), its development paths, directions of activity, and priorities at different stages of the work. It was emphasized that the greatest part of the Institute's developments has found practical application in the national economy. Many of them were sold under license agreements to different countries. The range of research areas is quite broad — from creation of underwater welding technologies to development of technologies of joining in space, from engineering new functional materials to development of technology of connecting live tissues in medicine. The Institute constantly keeps active cooperation with foreign companies and specialists.

Sheikh Imad Abu Al-Rub spoke in reply on behalf of the Arab party. He thanked the Ukrainian party, PWI management and specialists, participating in the meeting, for the opportunity of familiarizing with the activity of such world-renowned materials science center as PWI. He expressed the desire of a number of Arab countries to establish mutually beneficial business contacts with Ukrainian scientists. In his opinion, science is the sphere of cooperation, which can develop on a long-term basis. The established Council (UABC) will allow concentrating scientific-technical information provided by Ukrainian specialists, and bringing it through Arab country ambassadors to the respective structures in these countries. This will enable significantly speeding up organization of cooperation.

Other speakers were M. Strikha, O. Berezyuk, B. Bazilevsky, V. Komarnitsky, and M. Oliferenko. The following features were noted. At present the countries of the Arab world are poorly informed about Ukraine. They are interested in effective use of their available resources. Their objective is to become familiar with Ukraine's achievements as fully as possible, accumulate the information about successes in science, economy and private sector. They are interested in involving Ukrainian experts, in particular, from PWI, in UABC Expert Council. Today contacts with Kharkiv STU, Ivano-Frankivsk University and other organizations are also being established.

After studying Ukraine's proposals, it is intended to set up working groups in each field. The main purpose of the work is to obtain practical results.

It was noted that an Arab bank is now being established in Ukraine. This will allow ensuring timely funding of the work, improving confidence of the parties, and will speed up program fulfillment.

I.V. Krivtsun thanked UABC representatives for the provided information, and confirmed achievement of concrete results being an important component of cooperation. He noted that the presentations made today are just a small part of extensive range of subjects of the Institute's activity. We will have new meetings, participate in joint seminars and conferences, and find new topics for cooperation.

PWI publishes three scientific-technical journals — monthly «Avtomaticheskaya Svarka» (English version «The Paton Welding Journal») (subjects are welding and related technologies); quarterly «Tekhnicheskaya Diagnostika i Nerazrushayushchiy Kontrol», and «Sovremennaya Elektrometallurgiya». Familiarization with them will allow promptly receiving information about the most recent achievements of Ukrainian scientists in the field of welding, metallurgy, nondestructive testing and related technologies.

I.V. Kirvtsun introduced the topics of presentations and the presenters. Among them were:

In PWI exhibition hall

- welding and treatment of soft live tissues (G. Marinsky, Dr. of Sci. (Eng.), Department Head);
- innovative highly efficient methods and technologies of flash-butt welding of pipes for various applications and rails (I. Zyakhor, Cand. of Sci. (Eng.), Deputy Department Head);
- automated methods of underwater welding of metal structures (Yu. Maksimov, Dr. of Sci. (Eng.), Department Head);
- methods and technologies of welding lines for process power supply to electrolyzers in primary aluminium production plants (V. Kuzmenko, Lead. Eng.);
- technical diagnostics and monitoring of the state of critical welded structures (A. Nedoseka, Dr. of Sci. (Eng.), Department Head);
- welding of polymer pipes (M. Yurzhenko, Cand. of Phys.-Math. Sci., Department Head);
- training highly qualified welding operators in keeping with the requirements of European and International Standards (P. Protsenko, Director of International Educational-Certification Center).

Presentation subjects aroused a keen interest to the presenters. UABC specialists expressed a desire to receive electronic versions of brief resumes on each of the presented subjects.

Sheikh Imad Abu Al-Rub speaking during the discussion of cooperation prospects

Then I.V. Krivtsun invited meeting participants to PWI exhibition hall. A brief presentation on the subject of «Space activities» was made, when the visitors were familiarized with the exhibits earlier used in space: Vulcan equipment, «URI» hand tool for electron beam welding, «Universal» tool, «Isparitel» unit, as well as exhibits illustrating the Institute’s work on development of truss structures deployable in space.

Meeting participants expressed their gratitude for the intensive and constructive program and intent to actively promote Ukrainian-Arab cooperation.

Prof. V.N. Lipodaev

INTERNATIONAL CONFERENCE «ROBOTIZATION AND AUTOMATION OF WELDING PROCESSES»

Annual, traditional, summer International Conference took place at the E.O. Paton Electric Welding Institute on June 13–14, 2017. This year Conference was dedicated to robotization and automation of welding processes. The Conference was organized by the National Academy of Sciences of Ukraine, E.O. Paton Electric Welding Institute and International Association «Welding». More than 120 specialists from Ukraine, China and Poland participated in the Conference.

During visit of demonstration hall of the E.O. Paton Electric Welding Institute with a group of reporters of Chinese Xinhua News Agency. Demonstration of machine vision system

Among the participants are the scientists and specialists from E.O. Paton Electric Welding Institute, LLC «Fronius Ukraine», LLC «Fanuc Ukraine», LLC «Binzel Ukraine», Poland Institute of Welding in Gliwice, JSC «Motor Sich», NTUU «Igor Sikorsky KPI», Guangdong Institute of Welding (PRC), «Weihan Science and Technology» (PRC) and others (in total more than 40 companies).

The Conference was opened by Prof. L.M. Lobanov, Deputy Director of the NAS of Ukraine (academician of the NAS of Ukraine). After welcoming the participants of the Conference, he in short review outlined the main directions of the presentations.

Around 30 presentations were made during plenary session of the Conference. Conditionally, they can be divided on the following directions by topics:

- tendencies of development and application of robotics;
- example of application of effective solutions in welding processes automation;
- means for geometry adjustment and monitoring in robotic arc welding;
- practice of implementation of robotic complexes.

A lot of the presentations sparked interest of the Conference participants and were accompanied by questions to the presenters.

A day before the Conference, on June 13, the participants had the possibility (optionally) to visit LLC «Fronius Ukraine» (Knyazhychi village, Brovary area, Kyiv region). A group of 40 people was divided and V. Bondarenko and V. Slyuta, the representatives of LLC «Fronius Ukraine», conducted a familiarization excursion around the company territory.

The visitors saw a laboratory of automation and robotization. It is equipped with welding systems for mechanized and automatic welding using one or two arcs, systems for orbital welding of pipe with pipe and pipe with tube plate, system for welding in different spatial positions, automatic systems with magnetic containment in flat and vertical positions, system for surfacing on cylinder bodies. Also MAG surfacing process and CMT process with pulsed arc were demonstrated. The participants were also familiarized with laboratory unit for dual arc welding of longitudinal extended welds.

Participants of the Conference before boat trip over Dnieper

Engineering service of LLC «Fronius Ukraine» has been working since 2006. It helps to generate an order together with the customer, ensures training of technologist-operators, and provides consultations and engineering support. All this guarantees «correct work». The engineering service has specially equipped class for training.

In the conclusion the visitors attended a presentation on «Examples of effective solutions of welding (surfacing) processes automation», including welding of longitudinal welds FLW, welding process TIME (2 arcs) of bracket-like columns, CMT surfacing of mining equipment (one-layer surfacing with portion of base metal in deposited ≤ 6 wt.%), surfacing of inner pipe surfaces of 6 and 9 m length, CMT surfacing of support bearings, operation of system for orbital welding of open and close type.

ISSN 0005-111X

Автоматическая Сварка

www.patonpublishinghouse.com

СВАРКА • РЕЗКА • НАПЛАВКА • ПАЙКА • НАНЕСЕНИЕ • ПОКРЫТИЙ

Издается с 1948 года

МАЙ–ИЮНЬ 2017

TECHNOLOGY FOR THE WELDER'S WORLD.

iROB®

Системні рішення для роботизованого дугового зварювання від ABICOR BINZEL

ПІІ ТОВ «Бінцель Україна ГмбХ»

Тел.: 0-44 / 403-1299, 403-1399

Факс: 0-44 / 403-1499, 403-1599

E-mail: info@binzel.kiev.ua

ABICOR BINZEL ROBOTIC SYSTEMS

www.binzel-abicor.com

ИНСТИТУТ ЭЛЕКТРОСВАРКИ им. Е. О. ПАТОНА НАЦИОНАЛЬНОЙ АКАДЕМИИ НАУК УКРАИНЫ

ISSN 0957-798X

The Paton WELDING JOURNAL

May – June 2017

www.patonpublishinghouse.com

WELDING • CUTTING • SURFACING • BRAZING • COATING • DEPOSITION

/ Perfect Welding / Solar Energy / Perfect Charging

Fronius

TRANSSTEEL 5000 SYNERGIC

PROFESSIONAL MIG/MAG SYSTEM FOR PERSONAL TASKS

THE E. O. PATON ELECTRIC WELDING INSTITUTE OF THE NATIONAL ACADEMY OF SCIENCES OF UKRAINE

Familiarization with the developments of Fronius Company sparked lively interest of the visitors.

During the Conference the participants could visit a demonstration hall of the E.O. Paton Electric Welding Institute, where they could see welding robotic complex based on Fanuc robot and Fronius welding systems. The complex is equipped with machine vision system, developed at the E.O. Paton Electric Welding Institute by a team headed by Cand. of Tech. Sci. E.V. Shapovalov. «HORDA» wire from «Dizhka Pac» package, courtesy of «Vitapolis» Company (Boyarka, Kyiv region), was used in the welding robotic complex.

Proceedings of the Conference were published in «Avtomaticheskaya Svarka» journal Nos. 5/6, 2017 and in English in «The Paton Welding Journal», Nos. 5/6, 2017.

The Conference had creative, friendly atmosphere and was traditionally closed by evening trip over Dniper River on «Kashtan-5» motor ship, during which the participants admired of coastal landscapes with the churches, bridges over Dnieper as well as discussed in free atmosphere the perspectives of cooperation and directions of works in the field of welding processes robotization.

Dr. A. Zelnichenko and Prof. V. Lipodaev

PATON PUBLISHING HOUSE

www.patonpublishinghouse.com

SUBSCRIPTION

«The Paton Welding Journal» is Published Monthly Since 2000 in English, ISSN 0957-798X, DOI.ORG/10.15407/TPWJ2017.08.01.

«Avtomaticheskaya Svarka» Journal (Automatic Welding) is Published Monthly Since 1948 in Russian, ISSN 005-111X.

«The Paton Welding Journal» is Cover-to-Cover Translation of Avtomaticheskaya Svarka» Journal into English, DOI.ORG/10.15407/AS.

If You are interested in making subscription directly via Editorial Board, fill, please, the coupon and send application by Fax or E-mail.

The cost of annual subscription via Editorial Board is $348 for «The Paton Welding Journal» and $180 for «Avtomaticheskaya Svarka» Journal.

«The Paton Welding Journal» can be also subscribed worldwide from catalogues subscription agency EBSO.

SUBSCRIPTION COUPON

Address for journal delivery ______________________________

____

Term of subscription since __________ 20 till __________ 20

Name, initials ______________________________

Affiliation ______________________________

Position ______________________________

Tel., Fax, E-mail

We offer the subscription all issues of the Journal in pdf format, starting from 2009.

The archives for 2009–2015 are free of charge on *www.patonpublishinghouse.com* site.

ADVERTISEMENT

in «Avtomaticheskaya Svarka» and «The Paton Welding Journal»

External cover:
First page of cover (190×190 mm) — $700
Second page of cover (200×290 mm) — $550
Third page of cover (200×290 mm) — $500
Fourth page of cover (200×290 mm) — $600

Internal cover:
First/second/third/fourth page of cover (200×290 mm) — $400

Internal insert:
Page A4 (200×290 mm) — $340
Double page A3 (400×290 mm) — $500

- Article in the form of advertising is 50 % of the cost of advertising area
- When the sum of advertising contracts exceeds $1001, a flexible system of discounts is envisaged

Size of journal after cutting is 200×290 mm

Editorial Board of Journal «Avtomaticheskaya Svarka» and «The Paton Welding Journal»
E.O. Paton Electric Welding Institute of the NAS of Ukraine
International Association «Welding»
11 Kazimir Malevich Str. (former Bozhenko Str.), 03680, Kiev, Ukraine
Tel.: (38044) 200 47 57, 200 82 77; Fax: (38044) 200 82 77, 200 81 45
E-mail: journal@paton.kiev.ua; www.patonpublishinghouse.com